LEABHARLANN CHOLÁISTE NA TRÍONÓIDE, BAILE ÁTHA CLIATH | TRINITY COLLEGE LIBRARY DUBLIN
Ollscoil Átha Cliath | The University of Dublin

Terms and Conditions of Use of Digitised Theses from Trinity College Library Dublin

Copyright statement

All material supplied by Trinity College Library is protected by copyright (under the Copyright and Related Rights Act, 2000 as amended) and other relevant Intellectual Property Rights. By accessing and using a Digitised Thesis from Trinity College Library you acknowledge that all Intellectual Property Rights in any Works supplied are the sole and exclusive property of the copyright and/or other IPR holder. Specific copyright holders may not be explicitly identified. Use of materials from other sources within a thesis should not be construed as a claim over them.

A non-exclusive, non-transferable licence is hereby granted to those using or reproducing, in whole or in part, the material for valid purposes, providing the copyright owners are acknowledged using the normal conventions. Where specific permission to use material is required, this is identified and such permission must be sought from the copyright holder or agency cited.

Liability statement

By using a Digitised Thesis, I accept that Trinity College Dublin bears no legal responsibility for the accuracy, legality or comprehensiveness of materials contained within the thesis, and that Trinity College Dublin accepts no liability for indirect, consequential, or incidental, damages or losses arising from use of the thesis for whatever reason. Information located in a thesis may be subject to specific use constraints, details of which may not be explicitly described. It is the responsibility of potential and actual users to be aware of such constraints and to abide by them. By making use of material from a digitised thesis, you accept these copyright and disclaimer provisions. Where it is brought to the attention of Trinity College Library that there may be a breach of copyright or other restraint, it is the policy to withdraw or take down access to a thesis while the issue is being resolved.

Access Agreement

By using a Digitised Thesis from Trinity College Library you are bound by the following Terms & Conditions. Please read them carefully.

I have read and I understand the following statement: All material supplied via a Digitised Thesis from Trinity College Library is protected by copyright and other intellectual property rights, and duplication or sale of all or part of any of a thesis is not permitted, except that material may be duplicated by you for your research use or for educational purposes in electronic or print form providing the copyright owners are acknowledged using the normal conventions. You must obtain permission for any other use. Electronic or print copies may not be offered, whether for sale or otherwise to anyone. This copy has been supplied on the understanding that it is copyright material and that no quotation from the thesis may be published without proper acknowledgement.

Design and Characterization of Functional Interfaces for Fundamental Studies of Nitro-Polycyclic Aromatic Hydrocarbon Chemistry

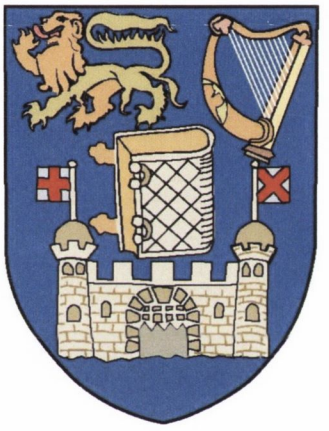

Deirdre M. Murphy, B.Sc.

School of Chemistry

Trinity College Dublin, Ireland

A thesis submitted for the degree of

Doctor of Philosophy (PhD)

January 2014

TRINITY COLLEGE
- 4 MAR 2014
LIBRARY DUBLIN

Thesis 10208

Declaration

I, Deirdre M. Murphy, declare that this thesis details entirely my own work, with due acknowledgements and references given to the work of others where appropriate. I also declare that this work has not been submitted, in whole or in part, to any other university or college for any degree or other qualification.

In submitting this thesis to the University of Dublin, I agree to deposit this thesis in the University's open access institutional repository or allow the library to do so on my behalf, subject to Irish Copyright Legislation and Trinity College Library conditions of use and acknowledgement.

Signature: Deirdre Murphy Date: 16/01/14

Summary

Nitro-polycyclic hydrocarbons (nPAHs) are a class of highly mutagenic compounds whose reactions and fates in the atmosphere have a tremendous effect on atmospheric chemistry. In the troposphere, the photodegradation of nPAHs occurs as a heterogeneous reaction on carbonaceous particles. In this work we aimed to design and characterize functional nPAH/carbon interfaces for fundamental studies of nitro-polycyclic aromatic hydrocarbon chemistry.

In Chapter 1, an introduction to the formation pathways, physical properties, fate and transformations of nPAHs is given. The properties of carbon and the use of amorphous carbon surfaces as model interfaces is also discussed, along with a brief description of the methodology utilized. In Chapter 2, we present an investigation into the spontaneous attachment of two nPAHs which are positional isomers and their monocyclic analog at amorphous carbon surfaces. We have focused on the adsorption kinetics of these polycyclic aryldiazonium salts and examined how their grafting rate and yield depends on the structure and stability of the salt. *In situ* grafting was monitored using Infrared reflection absorption spectroscopy (IRRAS) and results were complemented by electrochemical *ex situ* studies in order to determine surface chemisorption rates. The adsorption rates of the two positional isomers were found to be significantly different at amorphous carbon surfaces, a disparity which is attributed to a shift in reduction potential of the aryldiazonium salts.

Following this we then shifted our focus to exploring the fundamental processes occurring at the carbon-solution interface during the spontaneous grafting reaction and in Chapter 3, we provide a detailed study of charge transfer properties of the carbon materials used. A number of spectroscopic and electrochemical methods were utilized to characterize two amorphous carbon materials that differed in their degree of graphitization and to investigate their reactions *in situ* and *ex situ* with two isomeric aryldiazonium cations. To our knowledge this is the first time that a modification of electronic properties is shown to control relative reaction rates at the carbon/solution interface in disordered carbon materials. A discussion of our results in light of our current understanding of aryldiazonium chemisorption reactions and available models of charge-transfer at the solid/liquid interface is presented.

One reaction which is known to occur in the atmosphere is the photodegradation of nPAHs and this is thought to be their major loss pathway in the atmosphere. The photodegradation of nPAHs can occur as a heterogeneous reaction on soot particles, which make up a large percentage of particulate matter in the atmosphere. We therefore probed the photochemical behaviour of nPAHs at carbon substrates as a model for the reactions that occur on soot particles, as shown in Chapter 4. We utilized IRRAS to investigate the degradation of surface bound nPAHs. We show that the photodegradation of nitroaryl groups at surfaces can be measured with satisfactory time resolution. It is also found that the photodegradation of nPAHs at surfaces occurred through the loss of the nitro group and occurs in parallel with an oxidation process. A comparative study of the degradation of nPAHs in solution is also discussed.

Finally, a number of other model interfaces were designed and investigated which were not connected to nPAH chemistry and are presented in Chapters 5 and 6. Having gained an understanding of diazonium chemistry during the work carried out on nPAH/carbon interfaces, we utilized this expertise for the functionalization of substrates with biomolecules. Immobilization was confirmed via IRRAS characterisation, along with a quantitative assessment of the surface density of carbohydrate coated films obtained at carbon surfaces using *ex situ* quartz crystal microbalance measurements. This work showed that aryldiazonium chemistry offers a one-step, solution based functionalization method for the modification of surfaces with carbohydrates. A second functional interface in the form of a fluorinated surface was also designed and prepared and this is discussed in Chapter 6. Fluorine-fluorine interactions between polyfluorinated compounds and fluorinated surfaces were investigated and quantified using IRRAS. These results are highly significant as we demonstrate a clear opportunity for designing solid phase recovery systems for pollutants, ligands or catalysts based on fluorous chemistry.

Paul

Mo chompánach sa choireacht, sa saol agus i ngrá

Mom and Dad

Mo laochra don saol

Acknowledgements

This thesis was made possible due to the help and support of many people around me.

I would like to sincerely thank my supervisor, Prof. Paula Colavita for her direction during the past four years. This thesis would not have been possible without her. She has been a constant source of inspiration, information and guidance, for which I am tremendously grateful. I feel extremely lucky to have had Paula as my boss and will think of her always as a role model.

I would like to thank all of the members of my group throughout the years. I am very grateful for the time we spent working and socialising together. I would like to mention my friend and colleague Ronan Cullen. I thank him for providing data, valuable insights and somehow, always being there to help. I would also like to thank Dr. Laura Soldi for really looking after me at the start.

My acknowledgements would not be complete without a mention to my college friends who made this experience incredibly enjoyable. I truly appreciate the friendships I have made here. Thank you.

Special thanks go to the technical and secretarial staff in the School of Chemistry. I thank Patsy especially for the fun he brought to the teaching lab, Manuel for the immense amount of time he spent helping me with various pieces of equipment and Brendan Mulvaney for his cheerful and friendly banter.

I would like to acknowledge the collaborators I have worked with during the past four years. I thank Prof. Eoin Scanlan for his help with the synthesis of nPAHs and the modification of surfaces with carbohydrates. I also thank him for the useful conversations we had and the time and enthusiasm he dedicated to encouraging my skills in organic chemistry. I would like to acknowledge Prof. Robert Baker for his support and input in our collaborative work. I would like to thank Prof. Mike Lyons for all of his help with the electrochemical work presented in this thesis and of course, for the cork related humour. I

would like to acknowledge the financial support received from college and from Science Foundation Ireland.

I would like to mention Christopher McSweeney, who encouraged me to pursue a PhD. I'm glad I took your advice and thank you. I would also like to thank Karen Daly, an incredibly talented teacher who introduced me to chemistry; I would not have taken this route if it were not for you. I would like to thank my extended family, my friends from scouts and from home and the Ballincollig Boys. Caitriona and Eilis, thank you for your endless friendship.

I would like to thank my family, my biggest supporters. For keeping me calm, for cheering me up, for encouraging me and for believing in me. Dad, Mom, Tommy, Maeve, Orla, Laoise and Bailey. I could not have been blessed with a more wonderful family. Thank you.

Paul. Thank you for being my person. Thank you for all of the support, all of the hugs, all of your love, for your immense patience and for always knowing how to make me smile.

Table of Contents

Table of Contents viii

Table of Figures xii
Table of Schemes xvii
Table of Tables xviii

1. Introduction 1
   1.1. Motivation 2
   1.2. Nitro-polycyclic aromatic hydrocarbons 3
      1.2.1. General introduction and background 3
      1.2.2. Formation, sources and emissions 3
      1.2.3. Physical properties of nPAHs 6
      1.2.4. Photochemistry and transformations of nPAHs 9
      1.2.5. Influence and health effects of nPAHs 15
      1.2.6. Fate 19
   1.3. Carbon surfaces 22
      1.3.1. Properties of Carbon 22
      1.3.2. Carbonaceous aerosols in the environment 24
      1.3.3. a-C as a model surface 25
   1.4. Rationale and Methodology 26
      1.4.1. Rationale 26
      1.4.2. Methodology 27
   1.5. Applications of model interfaces in other fields 29
   1.6. References 29

2. Understanding the spontaneous grafting of nPAH aryldiazonium salts at amorphous carbon surfaces: Influence of structure and stability of the aryldiazonium salt on attachment 38
   2.1. Introduction 39
   2.2. Experimental 41

2.2.1. Chemicals and Materials 41
2.2.2. Synthesis of compounds for modification of surfaces 42
2.2.3. Sample characterization 45
2.2.4. Characterization techniques 48
2.3. Results and Discussion 50
2.3.1. Grafting of 4NND and 5NND at carbon surfaces 50
2.3.2. *In situ* adsorption rate studies at carbon/solution interfaces 53
2.3.3. *Ex situ* studies of grafting rates at carbon surfaces 56
2.3.4. Dediazoniation of 4NND and 5NND salts 57
2.3.5. XPS Characterization of 4NND and 5NND adlayers 60
2.3.6. Electrochemical analysis of electron density differences 62
2.4. Conclusions 63
2.5. References 64

3. Heterogeneous charge transfer at the amorphous carbon/solution interface: effect on the spontaneous attachment of nPAH aryldiazonium salts 67
3.1. Introduction 68
3.2. Experimental 70
3.2.1. Chemicals and materials 70
3.2.2. Preparation of carbon substrates 70
3.2.3. Functionalization of carbon substrates 70
3.2.4. Characterization 71
3.3. Results 73
3.3.1. Properties of annealed amorphous carbon films 73
3.3.2. *In situ* and *ex situ* studies of 4NND and 5NND adsorption at amorphous carbon substrates 76
3.3.3. Valence structure at amorphous carbons 80
3.3.4. Electron transfer studies at amorphous carbons 81
3.4. Discussion 84
3.5. Conclusions 91
3.6. References 92

4. Photochemical investigations of nPAHs at amorphous carbon surfaces 95
4.1. Introduction 96
4.2. Experimental 99
4.2.1. Chemicals and materials 99
4.2.2. Sample preparation 100
4.2.3. Photodegradation setup 100
4.2.4. Characterization methods 101
4.3. Results 102
4.3.1. UV-Vis absorption spectra of parent molecules 102
4.3.2. Photodegradation of 4NB at a-C surfaces 103
4.3.3. Photodegradation of 4NN at a-C surfaces 107
4.3.4. Photodegradation of 4NND at a-C:H surfaces 111
4.3.5. Photodegradation of nPAH in solution 112
4.4. Discussion and Conclusions 114
4.5. References 117

5. Carbohydrate coated surfaces using aryldiazonium chemistry 119
5.1. Introduction 120
5.2. Experimental 122
5.2.1. Chemicals and materials 122
5.2.2. Surface preparation 122
5.2.3. Preliminary grafting experiments 122
5.2.4. Synthesis of Diazonium tetrafluoroborate derivatives of acetylated carbohydrates and surface functionalization procedure 123
5.2.5. Characterization Methods 124
5.3. Results and Discussion 125
5.3.1. Preliminary surface modification using aryldiazonium carbohydrates 125
5.3.2. Functionalization of various acetylated carbohydrates onto amorphous carbon surfaces 126
5.3.3. Functionalization of carbohydrates onto various surfaces 128
5.3.4. Surface density of carbohydrate coated carbon films 129
5.4. Conclusions and supporting work 130

5.5. References 131

6. Fluorine-Fluorine interactions for recovery and separation 134
6.1. Introduction 135
6.2. Experimental 138
6.2.1. Chemicals and materials 138
6.2.2. Preparation of substrates 138
6.2.3. Preparation of Perfluoro-Self Assembled Monolayers 140
6.2.4. Physisorption Studies 140
6.3. Results and Discussion 141
6.3.1. Preliminary grafting experiments 141
6.3.2. Physisorption Studies 142
6.3.3. Comparison of physisorption of compounds 144
6.4. Conclusions 148
6.5. References 149

7. Conclusions and Future Work 151

Table of Figures

Figure 1.1. Ternary phase diagram of amorphous carbons reproduced from Robertson..... 23
Figure 1.2. Density of states in a-C films as a result of the mixed π and σ states. 24
Figure 1.3. Schematic of diesel soot particle showing (a) elemental carbon, (b) surface adsorbed organics and (c) surface sulfates. 25
Figure 1.4. Schematic of spontaneous grafting of an aryldiazonium salt onto a surface. 28

Figure 2.1. Schematic of custom built ATR cell for in situ monitoring with pathlength (*l*) indicated. 46
Figure 2.2. IR spectrum of $K_3[FeCN_6]$ 46
Figure 2.3. IR spectrum of 4NND 47
Figure 2.4. Principle of ATR-FTIR measurement 48
Figure 2.5. Depiction of p- and s- polarised components of light 49
Figure 2.6. Electric fields at metal interface for (a) parallel and (b) perpendicular external electric field 49
Figure 2.7. IRRAS spectra of a-C substrates following immersion in 1×10^{-3} M 4NND and 5NND solutions for 1 h 50
Figure 2.8. IR spectra of the bulk unattached diazonium salt measured via ATR 51
Figure 2.9. (a) IRRAS spectra of a-C substrates following immersion in 1×10^{-3} M 5NND aqueous solution for 1 h and (b) ATR-FTIR spectra collected at 5.3 h following injection of a 1×10^{-4} M 4NND aqueous solution 52
Figure 2.10. Cyclic voltammograms of 4NND and 5NND-modified a-C electrodes obtained in 0.1 M H_2SO_4 at 0.2 V s^{-1}; the substrates were modified via immersion in 1×10^{-4} M aqueous solutions of 4NND and 5NND for 10 min 53
Figure 2.11. (a) ATR-FTIR spectra collected as a function of time after injection of a 1×10^{-4} M 4NND aqueous solution into the liquid cell; spectra are offset for the sake of clarity. (b) Plot of the pathlength-corrected net absorbance of $\nu_s(NO_2)$ as a function of deposition time obtained for 4NBD, 4NND and 5NND. (c) Plot of the $\nu_s(NO_2)$ net absorbance normalized

by pathlength and absorption cross-section (Normalized Net Absorbance), as a function of deposition time.....54
Figure 2.12. Surface coverage of nitrophenyl groups (Γ) on a-C substrates as a function of deposition time in 1×10^{-4} M 4NND (○) and 5NND (■) solutions.....56
Figure 2.13. Thermogravimetic analysis of 4NND and 5NND under N_2 in the range 0-900 °C at 10 °C/min.....58
Figure 2.14. Comparative UV spectra of 4NBD, 4NND and 5NND.....58
Figure 2.15. UV-Vis spectra of 1×10^{-4} M solutions of (a) 4NND and (b) 5NND) during hydrolysis at 37 °C over a period of 7 h. The insets show the corresponding first-order kinetic plots obtained from the UV-Vis data (see Equation 2.1.).....60
Figure 2.16. XP spectra in the N 1s region of (a) 4NND and (b) 5NND adlayers at a-C surfaces.....61
Figure 2.17. Cyclic voltammetry at 0.2 V s^{-1}, showing reduction peaks of diazonium ($-N_2^+$) groups of 4NND and 5NND in anhydrous acetonitrile solution.....63

Figure 3.1. (a) Raman spectra (514 nm) of carbon films as deposited (a-C), after annealing at 500 °C (a-C500) and 700 °C (a-C700) for 1 h, and of glassy carbon (GC) (b) I_D/I_G vs. G peak position for a-C, a-C500, a-C700 and GC.....73
Figure 3.2. (a) a-C deposited on quartz before (left) and after (right) annealing at 700 °C. (b) Typical Tauc plots of as prepared amorphous carbon films (a-C) and after annealing at 700°C (a-C700).....74
Figure 3.3. C 1s XP spectra of a-C and a-C700 films. 75
Figure 3.4. Cyclic voltammetry of a-C700 electrodes modified via partial intercalation of 4NBA in acetonitrile solution, measured in 0.1 M H_2SO_4 at 0.2 V s^{-1}.....75
Figure 3.5. (a) Symmetric $-NO_2$ stretching peak of 4NND obtained via in situ ATR-FTIR at a-C700 surfaces after injection of 1×10^{-4} M 4NND. (b) Adsorption curves for 4NND and 5NND at a-C700, after normalization.....77
Figure 3.6. Comparison of adsorption curves of 4NND (a) and 5NND (b) at a-C and a-C700 obtained from 1×10^{-4} M solutions over 3 h of reaction. 77
Figure 3.7. (a) Cyclic voltammograms of 4NND and 5NND-modified GC electrodes obtained in 0.1 M H_2SO_4 at 0.2 Vs $^{-1}$; substrates were modified by immersion in 1×10^{-4} M

aqueous solutions of 4NND and 5NND for 10 min. (b) Surface coverage of nitroaryl groups (Γ) on GC substrates as a function of deposition time in 1×10^{-4} M 4NND (●) and 5NND (■) aqueous solutions. 78
Figure 3.8. Normalized UPS spectra of a-C700 and as deposited a-C surfaces with spectra offset for clarity. 80
Figure 3.9. (a) High and (b) low binding energy regions of normalized UPS spectra of annealed carbon (a-C700) and as deposited amorphous carbon (a-C) surfaces. 81
Figure 3.10. Experimental impedance data represented as Nyquist plots for a-C and annealed a-C700 electrodes with frequencies at maximum Z. Continuous lines show the best fit of EIS data using the equivalent circuit shown in the inset. 82
Figure 3.11. Experimental impedance data represented as Nyquist plots for a-C700 and GC electrodes. 83
Figure 3.12. Schematic showing the Fermi levels obtained from work function determinations of carbon substrates in this chapter, the position of electron acceptor levels of 4NND and 5NND obtained from electrochemical measurements,[12] and the literature position of the Standard Hydrogen Electrode (SHE), all relative to vacuum.[45] 87
Figure 3.13. Example of the integration procedure used to calculate charge transfer rate constant ratios using the approximation in Equation 3.6.. The intensity of the UPS photoemission and the distribution of $Ru(NH_3)_6^{+3/+2}$ acceptor levels in solution are shown after alignment of their Fermi levels (E=0); the y-scaling is arbitrarily chosen for the two curves in order to facilitate graphical comparison. The inset shows the product of the two curves which defines a narrow energy interval over which the overlap can be integrated (indicated by the bracket). 88

Figure 4.1. Photodegradation experimental set-up 101
Figure 4.2. UV–Vis spectra of (a) nitrobenzene and 4-nitrobenzene diazonium and (b) nitronaphthalene and 4-nitronaphthalene diazonium in aqueous solution. 102
Figure 4.3. (a) Raw IRRAS spectra of 4NB on a-C irradiated with filter at position 1 over 24 h. Spectra have been offset for clarity. (b) Close up of the nitro symmetric stretching peak region 103
Figure 4.4. Percentage change in symmetric nitro peak over time for 4NB on a-C 104

Figure 4.5. Logarithmic plots of the symmetric nitro peak decay at (a)Filter position one ((λ > 200 nm, (b)Filter position two (λ > 350 nm) and (c)Filter position three (λ > 440 nm).105
Figure 4.6. Percentage change in the symmetric nitro peak for 4NBD modified a-C surfaces measured over 24 h using λ > 200, λ > 350 and λ > 440 with weighted exponential fitting of the decay.....106
Figure 4.7. Plot of decrease of nitro symmetric peak (•) and emergence of CO peak (•) for 4NB surfaces with irradiation at λ > 200 nm (filter one). Lines show fitting with exponential functions.....107
Figure 4.8. Raw IRRAS spectra of 4NN at a-C with irradiation at λ > 200 nm.....108
Figure 4.9. Percentage change in symmetric nitro peak for 4NND modified a-C surfaces measured over 12 h using λ > 200, λ > 350 and λ > 440 with weighted exponential fitting of the decay.....109
Figure 4.10. Comparison of 4NB and 4NN decay curves through filter one (λ >200 nm).109
Figure 4.11. Plot of decrease of nitro symmetric peak (•) and emergence of CO peak (•) for 4NND modified surfaces with irradiation at λ > 200 nm (filter one). Lines show fitting with exponential functions.....110
Figure 4.12.(a). Raw IRRAS spectra of 4NN on a-C:H irradiated using filter one over 4 h and (b)percentage change in symmetric nitro peak over time for 4NND modified a-C:H.111
Figure 4.13. UV–Vis spectra of 2.6×10^{-5} M 1NN following irradiation at λ > 200 nm over 18 h. 113
Figure 4.14. Plot of percentage change of absorbance at 213 nm of 2.6×10^{-5} M 1NN following irradiation at λ > 200 nm over 18 h. 113

Figure 5.1. Background corrected IRRAS spectra of C and Cu surfaces following in situ modification with (**A**). IR spectra of parent amine compound and carbohydrate rhamnose. 125
Figure 5.2. Raw IRRAS spectra of C, Cu and Au surfaces following in situ modification with (**B**). 126
Figure 5.3. IRRAS spectrum of carbohydrate coated a-C substrate obtained via surface functionalization of aryldiazonium salt **4** from a 1.0 mM aqueous solution. 127

Figure 5.4. IRRAS spectra of carbohydrate coated carbon substrates obtained via surface functionalization of aryldiazonium salts of compounds **1** (trace a), **2** (trace b),..... 128
Figure 5.5. Fluorescence microscopy images of carbon surfaces after binding experiments using fluorescently labelled biomolecules; the lower half of the carbon surface has been modified with a monosaccharide, whereas the upper half remains bare. (a) Binding experiment on Man-modified carbon surfaces using FITC-ConA lectin (b) Binding experiment on Gal-modified carbon surfaces using FITC-PNA lectin 131

Figure 6.1. IRRAS spectrum of PF-SAM grafted at Cu surface. 142
Figure 6.2. **Top:** IR absorption spectrum of 5. **Bottom:** IRRAS spectra of PF-SAM (A), of PF-SAM after adsorption of compound 5 (B), and after vigorous sonication to remove physisorbed material (C). Spectra have been offset for clarity. 143
Figure 6.3. Integrated absorbances in the region 1400-1000 cm^{-1} of compounds 2-7. Error bars indicate 90% C.I. 144
Figure 6.4. IRRAS spectra of PF-SAM (A), of PF-SAM after adsorption of compounds (B), and after vigorous sonication to remove physisorbed material (C) for compounds 2-7. Spectra have been offset for clarity. Unresolved peaks are assigned as follows CF_3 stretching modes (■), asymmetric CF_2 vibrations (▲), symmetric CF_2 vibrations (●) stretching of C-C bonds and bending of CCC (♦). 147

Table of Schemes

Scheme 1.1. Mechanism of formation of gaseous nPAHs in polluted atmospheres. 4
Scheme 1.2. Structure of 2-nitrofluoranthene. 5
Scheme 1.3. Photochemical degradation pathways of 1 nitropyrene. 11

Scheme 2.1. Heterolytic (A) and homolytic (B) pathways of covalent aryldiazonium attachment at surfaces. 39
Scheme 2.2. Structures of 4-nitrobenzene diazonium tetrafluoroborate (4NBD), 4-nitronaphthalene diazonium tetrafluoroborate (4NND) and 5-nitronaphthalene diazonium tetrafluoroborate (5NND). 41
Scheme 2.3. Structure of 4-nitro-1-naphthylamine (4NNA). 42
Scheme 2.4. Structure of 4-nitro-naphthalene diazonium tetrafluoroborate (4NND). 43
Scheme 2.5. Structure of 5-nitro-1-naphthalen-1-amine (5NNA). 43
Scheme 2.6. Structure of 5-nitro-naphthalene diazonium tetrafluoroborate (5NND). 44

Scheme 3.1. Proposed mechanism of aryldiazonium salt chemisorption reactions. 68
Scheme 3.2. Structures of 4-nitronaphthalene diazonium tetrafluoroborate (4NND) 69

Scheme 4.1. Proposed mechanism for the photodegradation of 1-nitronaphthalene.....97
Scheme 4.2. Structures of 4-nitrobenzene diazonium tetrafluoroborate (4NBD) and 4-nitronaphthalene diazonium tetrafluoroborate (4NND). 98
Scheme 4.3. Structures of 1-nitronaphthalene (1NN) and nitrobenzene (NB). 99

Scheme 5.1. Structures of unprotected 4-aminophenyl rhamnoside (**A**) and benzyl protected 4-aminophenyl rhamnoside (**B**). 122
Scheme 5.2. Peracetylated 4-aminophenyl glucoside (**1**), galactoside (**2**), mannoside (**3**) and rhamnoside (**4**). 123
Scheme 5.3. Formation of glycosyl diazonium intermediate. 124

Scheme 6.1. Classification of Halogen – Halogen interactions. 136
Scheme 6.2. Procedure for the modification of surfaces with fluorinated compounds. 141

Table of Tables

Table 1.1. Properties of diamond, graphite and amorphous carbon. 22

Table 2.1. Assignment table for bulk diazonium salts. 51

Table 3.1. RMS roughness values for bare and modified a-C and a-C700 substrates measured using AFM. 79
Table 3.2. Values of fitting parameters for a-C and a-C700 from Figure 3.10. 82
Table 3.3. Summary of electrochemical potentials of redox species used in our experiments referenced to SHE and to the vacuum level. 84
Table 3.4. Relative values of electron transfer rate constants for the spontaneous reduction of aryldiazonium cations in water at the two carbon surfaces investigated in this work, calculated using a Gerischer-Marcus model and Equation 3.6. 89

Table 4.1. Filter specifications and total power measured at the sample position. 101
Table 4.2. First order rate constant, limiting value at $t \rightarrow \infty$, and initial rate decay of 4NB at a-C surfaces. 106
Table 4.3. First order rate constant, limiting value at $t \rightarrow \infty$ and initial rate decay of 4NN at a-C surfaces. 109
Table 4.4. First order rate constant, limiting value at $t \rightarrow \infty$ and initial rate decay of 1NN in aqueous solution. 113

Table 5.1. Surface coverage obtained from functionalization reactions with 1.0 mM solutions of 4-aminophenyl glycoside precursors **1-4** 129

Table 6.1. Compound numbers and structures for fluorine-fluorine physisorption tests... 139
Table 6.2. Summary of the integrated absorbances in the 1000-1400 cm^{-1} region for compounds 2-8. 146
Table 6.3. Peak assignments for fluorinated compounds 2-7. 148

1. Introduction

The following chapter presents an introduction to the formation pathways, sources, physical properties, fate and transformations of nPAHs. The influence and health effects of these ubiquitous pollutants are also examined. Thereafter, the properties of carbon and the use of amorphous carbon surfaces as model interfaces are discussed, along with a brief description of the modification methodology utilized to form nPAH/carbon interfaces.

1.1. Motivation

The work herein aims to tackle the design and characterization of functional interfaces for fundamental studies of nitro-polycyclic aromatic hydrocarbon (nPAH) chemistry. nPAHs are environmentally relevant pollutants which are ubiquitous in ambient atmospheres and knowledge on the formation, fate and degradation of this class of compounds is paramount for further understanding of atmospheric chemistry and health effects of anthropogenic emissions. nPAHs undergo many reactions and transformations in the environment and the purpose of this work is to gain an understanding of these reactions from a fundamental point of view. While there is a noticeable lack of knowledge about the factors which influence the environmental fate of nPAHs, one class of reactions that are known to occur is their heterogeneous reactions on carbonaceous soot particles. We have developed a model surface of deposited amorphous carbon (a-C) films to help us understand the environmentally important reaction of nPAHs at carbon surfaces in the atmosphere. We used aryldiazonium chemistry as a modification method that enables us to probe reactions of nPAHs at carbons. These reactions depend on the structures of the adsorbed compound and are also greatly influenced by the physical and chemical nature of the surfaces onto which they are adsorbed.[1-2] This work aims to examine coupling of nPAHs at carbon surfaces to explore these dependencies, initially by investigating the adsorption of molecular conformers at amorphous carbon surfaces. Thereafter, we probe the effect the composition and electronic properties of the carbon surface has on the reaction of nPAHs at the surface. As photolysis is the major degradation pathway of nPAHs, we present an investigation into the photochemical behaviour of nPAHs at carbon surfaces. This work provides experimental data on the interfacial chemistry of nPAHs at carbon surfaces that is crucial for understanding atmospheric reactions of these molecules. Finally, unrelated to nPAH chemistry but relevant for environmental uses of surfaces, we show the development of functional interfaces for separation technologies and the design of bioactive surfaces.

1.2. Nitro-polycyclic aromatic hydrocarbons

1.2.1. General introduction and background

Polycyclic aromatic compounds (PACs) are a complex category of organic molecules consisting of fused ring structures with at least two benzene rings in linear, angular or cluster arrangements. In their simplest form these compounds contain only carbon and hydrogen atoms and are referred to as polycyclic aromatic hydrocarbons (PAHs). In more complicated structures, PAHs can contain additional fused rings which are not six-sided. Sulfur and nitrogen analogues of PAHs are also possible, as are substitutions of entire moieties, such as oxy- and nitro- groups.[1] The molecules resulting from the incorporation of nitro groups in PAHs are the focus of this thesis.

Nitro-polycyclic aromatic hydrocarbons (nPAHs) are a highly mutagenic class of compounds that consist of fused aromatic rings with one or more nitro groups attached to the aromatic moiety.[3-4] nPAHs are ubiquitous contaminants that are extremely important compounds in the environmental chemistry of the polluted atmosphere. While it is beyond the scope of this thesis to give detailed accounts of the physical and chemical properties of PACs and their derivatives, these can be found in the literature.[1,5] The subsequent sections summarize the properties of nPAHs that are relevant for their atmospheric behaviour.

1.2.2. Formation, sources and emissions

PAHs and nPAHs are formed via a number of processes. They originate from both natural and anthropogenic incomplete combustion and pyrolysis of organic matter such as fossil fuels and petrochemical fuels.[2,6-9] The incomplete combustion of organic matter which occurs due to natural events, such as volcanic eruptions and forest fires also contribute to PAHs and nPAHs in the atmosphere however anthropogenic emissions are the predominant source from this formation pathway, where organic PAH are nitrated during combustion processes.[7,10-12] Up until the mid-1980's it was believed that anthropogenic emissions were the major formation source of nPAHs in ambient air.[1,13] It was then shown that nPAHs are also formed via *in situ* gas phase reactions of PAHs with NO_2, NO_2 radicals and NO_3 in polluted atmospheres, and also with atmospheric oxidants such as N_2O_5, oxygen radicals and hydroxyl radicals in the presence of nitrogen oxides[2,8-9] and that these formation

processes contribute significantly to the total nPAHs found.[1-2,14] Different isomers of nPAHs result from their different formation processes,[2,15] meaning that nPAHs from direct emissions or atmospheric reactions can be distinguished from each other as shown in a review by Ravindra *et al.* which matches individual PAHs with their origin sources.[11] For example, the nitroproducts formed via atmospheric gas phase reactions are not the isomers that are expected from an electrophilic nitration mechanism. Following OH radical attack at the most electro rich site, NO_2 addition occurs at a neighbouring carbon, however for nPAHs formed from combustion the isomers are as expected from electrophilic nitration.

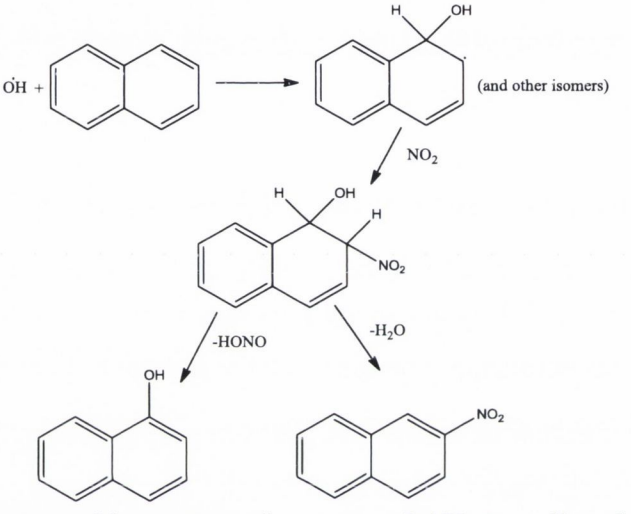

Scheme 1.1. Mechanism of formation of gaseous nPAHs in polluted atmospheres.[1]

The major mechanism for formation of gaseous nPAHs in polluted atmospheres consists of the reaction of OH radicals with gaseous PAHs at the sites of highest electron density and the subsequent addition of NO_2 to the PAH-OH adduct, as shown in Scheme 1.1.[2,13-14,16] Experiments were conducted which confirmed this reaction mechanism in which semi-volatile PAHs were subjected to low levels (sub ppm) of NO_2 with trace HNO_3 in ambient air conditions resulting in the formation of nPAHs in excellent yields.[14,17-18] Deposition on a variety of substrates and exposure to a range of concentrations of NO_2 were also investigated with trace amount of HNO_3 and the formation of mono and dinitro-PAHs confirmed.[1,17-19] Reaction with OH radicals is the predominant gaseous formation process overall, and the predominant daytime formation pathway, but reactions with other gaseous atmospheric species, such as with NO_3 radicals at night, also contribute and nPAHs have been shown to be formed in atmospheric liquid and gaseous phases owing to photochemical and dark nitration.[20]

The rate at which atmospheric nPAH are formed depends on many parameters, including the concentrations of reacting species, the rate constants for PAH reaction with OH radicals/NO_3 radicals and meteorological conditions such as humidity and sunlight radiation.[9,15] The major precursors of nPAHs in the atmosphere are gaseous PAH.[21] Nielson *et al.* probed the reactivity of PAHs towards nitrating species by measuring transformation rates in solution.[14] The nitration reaction was proposed to proceed through an electrophilic attack, as electron-donating substituents enhanced the reactivity and electron-withdrawing groups diminished it. 2-Nitrofluoranthene (2-NF) is an example of an nPAH which is formed via atmospheric reactions of PAHs with nitrogenous species in polluted atmospheres shown in Scheme 1.2. This molecule contributes significantly to the mutagenicity of airborne particulate matter and is measured at higher concentrations than other 4-6 ring nPAHs.[22-23]

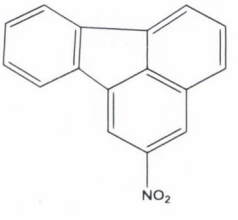

Scheme 1.2. Structure of 2-nitrofluoranthene.

Nitronaphthalenes are another cohort of this class of compounds whose formation occurs either via direct combustion emissions or via atmospheric nitration of naphthalene with OH radicals during daytime and reaction with nitrate radicals during nighttime in the presence of NOx.[24-25] Due to the environmental relevance of nPAHs, formation pathways have been extensively researched. For example, Carrara *et al.* investigated nPAH formation which occurs while operating diesel engines by exposing artificially PAH-coated soot aerosol with NO_2 at varying temperatures.[26] Fan *et al.* presented an investigation of nPAH formation and decay in the atmosphere from which a reaction mechanism was elucidated by modelling of results from an outdoor smog chamber.[8] It has even been shown that nPAHs can be formed via an *in situ* reaction in fish.[27]

An evaluation of the sources of PAHs and nPAHs reveals divisions into a number of different sources. Anthropogenic sources of PAHs and nPAHs can be divided into mobile and stationary categories. Mobile sources consist of vehicle emissions, in particular diesel

engines, but also including railways, ships and aircrafts.[7] Stationary sources include those from industrial sources (power generation, incineration, coal and oil refining process, processing of primary materials) and domestic sources (fossil fuel combustion, cigarette smoke, residential heating and wood burning).[7,9,28-30] For domestic sources, heating and cooking are the most important contributors to the total emissions in the environment. This leads to major health concerns, especially due to the use of combustion of solid fuel for cooking and heating in third world countries.[9,11] Natural sources of PAHs and thereby nPAHs include volcanic eruptions, decaying of organic matter, accidental fires caused by lightning strikes and agricultural sources such as biomass burning.[9,31] An in-depth review of the sources of PAHs found in particulate matter is reported by Lee *et al.* [9]

Investigations into PAC emissions have mainly focused on unsubstituted PAHs.[11,28,32] Mastral *et al.* present a review on PAH emissions from energy generation sources in which they probe the influence of PAH origin, fuel type, combustor type and combustion variables with respect to PAH formation and emissions in the solid/gaseous phase.[32] More recently, nPAH emissions have been studied, which is expected as these emissions are especially important due to the direct acting mutagenicity of these compounds.[33-34] When considering nPAHs which have been emitted directly from combustion sources, the most common emission source of nPAHs is believed to be diesel engines.[23,34] nPAHs are amongst the most toxic components of diesel emissions and releases of such compounds are of concern due to their climatic impact and possible effects on human health. Investigations into the emissions of PAHs and nPAHs from diesel vehicles have been carried out by Hu *et al.*, which included the analysis of 35 particles associated with nPAHs in exhaust emissions.[34] Recent publications on the emissions of nPAHs have focused on those produced from residential wood combustion and from heavy duty diesel exhausts.[33-34]

1.2.3. Physical properties of nPAHs

nPAHs are ubiquitous and persistent atmospheric pollutants which have been found to occur in ambient and urban air, in natural and waste waters, and in sediments and soils. They are present in the exhausts of vehicles and waste incineration plants, in carbon black and toner cartridges, in cigarette smoke and even in food stuffs.[20,28,30,35] nPAHs exist in the

environment as a mixture, with their parent PAHs, along with hundreds of other organic compounds.[12] In total, more than one hundred different nPAHs have been identified in various samples in the literature.[28,36] Generally, these compounds have high physical and chemical stability, exert toxic effects on humans, are resistant to biological transformations and tend to accumulate.[29,36]

The concentration of nPAHs in the atmosphere is of interest as these compounds are potent mutagens.[15] Concentrations of nPAHs have been determined to range from <1 pg m^{-3} up to approximately 1 ng m^{-3}, which is 10-1000 times lower than the concentrations of their parent PAHs.[37] Concentrations of nPAHs of several nanograms per gram of particulate material have been reported in urban areas.[38] Intuitively, the magnitude of atmospheric compounds such as nPAHs is related to their emissions and stability.[7] Another influencing parameter on the concentrations of atmospheric particle associated nPAHs is the particle size of the matter to which the nPAHs have condensed onto.[7] The concentrations of nPAHs in the atmospheric have been shown to be influenced strongly by seasonal variation in particulate PAH levels.[28] Reisen *et al.* present a study deciphering how atmospheric reactions influence seasonal PAH and nPAH concentrations in Los Angeles (LA).[15] They showed that PAH concentrations were highest in LA during January, due to emissions from traffic whilst nPAH concentrations were highest at the sub-urban site during August due to enhanced summertime photochemistry. Several groups have monitored the concentrations of PAHs and nPAHs and identified the sources of these compounds, which in urban areas were found to be predominantly caused by traffic emissions, incineration and coal combustion.[6,39] Edwards *et al.* discuss concentrations of PAHs found in air, soil and vegetation.[31]

PAHs have a low solubility in water and this decreases with increasing ring size.[1,11-12] This hydrophobicity enables their persistence in the environment.[30] However when PAHs react to form more polar species such as nPAHs, their solubility is greatly enhanced. The increased solubility of nPAHs, which have been shown to be significantly more mutagenic than their parent PAHs, has major implications on the distribution of nPAHs in the environment.[1-2,14,16,39] This emphasizes the importance of nPAHs from an environmental

perspective, but also in terms of possible impacts on public health and exposure to ecosystems.

nPAHs exist in different phases in the atmosphere.[12,16,32] They are found as gases and adsorbed onto particles in ambient air, exhaust emissions and primary combustion emissions.[8,14] nPAHs occur in the gas phase as volatile 2- ring systems, in the particle phase as 5- and 6- ring systems and are also present as semivolatile 3- and 4- ring systems which partition between the gas and particle phases.[1,7] The partition distribution of compounds in the atmosphere is determined by factors such as the ambient temperature, the concentration of the compound and the mass and size of available particles to adsorb onto.[1,7,32] The vapour pressure of a compound is another extremely important influencing parameter on its partitioning distribution.[28,32] Owing to their low vapour pressures, large condensed ring structures such as pyrene and anthracene tend to condense onto particle surfaces,[9] whereas PACs with lower molecular weights and higher vapour pressure are found almost exclusively in the gaseous phase.[7,11,29] The vapour pressures of nPAHs are lower than those of their parent PAHs, meaning a larger fraction of them partition into the gaseous phase. An example of nPAHs which are found in the vapour phase are nitronaphthalenes.[9] Despite there being higher levels of low molecular weight PACs in the gaseous phase, more of the probable human carcinogenic of PACs are associated with particulate matter, highlighting the importance of understanding particle associated nPAH chemistry.[11] Another interesting fact about the gas particle distribution is that heavier nPAHs may be formed in the gas phase, however they condense immediately onto particulate and hence are not detected in the gaseous phase.[8,40] Knowledge on gas-particles distributions of such pollutants are imperative for conducting accurate modeling studies.[2] A vital factor for determination of the chemical and physical fates of nPAHs depends on whether they exist in the gas or particle phase or are partitioned between them. Consequently, their rates of reaction, mechanisms and transport through the environment can vary hugely depending on how they are partitioned.[1] Evidence of this is given by the tremendously different fates of naphthalene (2-ring system) and pyrene (4-ring system) in literature studies.[1] More details of gas particle partitioning can be found in the literature, where Yamasaki developed a gas-particle equilibrium constant based on Langmurian absorption theory.[41] Using this work, Feilberg *et al.* determined equilibrium constants for partitioning of 1-nitronaphthalene

(1NN) and 2-nitronaphthalene (2NN) between the gas phase and diesel exhaust particles using a smog chamber system.[37]

Deciphering the size distribution of nPAHs is imperative for understanding their fate in the environment and also their possible health effects, as particle size can determine the deposition behaviour in respiratory organs.[23] The size distributions of particle-associated PAHs and nPAHs in ambient air have been reported in the literature and have been shown to fall into two size groupings.[23,42] The first grouping consists of non-volatile PACs formed via adsorption onto particles less than one micrometer in size, whilst the second grouping is made up of volatile PACs which have condensed onto particles greater than one micrometer.[6-7,42] Kawanda *et al.* clarify these size groupings by reporting the size distribution of PAHs and nPAHs in atmospheric particulate matter measured using a low pressure cascade impactor in a traffic tunnel.[23] The particulate matter was found to consist of a bimodal size distribution whereas the nPAHs measured in this traffic tunnel were unimodal. Particles less than 10 μm are ultrafine particles and can infiltrate the human respiratory system. The largest fraction of particle associated PACs are ultrafine particles and thereby lie within the respirable size range.[7,23] Ultrafine particles have been shown to deposit on the surfaces of respiratory organics such as blood vessels of the lungs and pulmonary alveoli cells. Further evidence that a significant proportion of airborne organic particulate matter is distributed into the respirable size range is given by Baek,[43-44] who sampled an urban location and found that 95% of particle associated PACs had a diameter of less than 3.3μm. These examples illustrate the importance of understanding particle associated PAHs and nPAHs and their reactions due to the significant risk they pose to human health.

1.2.4. Photochemistry and transformations of nPAHs

nPAHs undergo photochemical reactions in the atmosphere and photodegradation is their major degradation pathway. It is important that we understand the photochemistry of nitroaromatics as they decay naturally in the atmosphere through light-induced reactions.[38] A detailed synopsis of the photochemical behaviour of atmospheric particulate matter, including particle associated PAHs can be found in the literature.[45] Owing to the

photolabile chromophore group ($-NO_2$) the photodegradation of nPAHs is more rapid than the parent PAH degradation which ensures faster oxidation and substitution of the aromatic ring under photolysis conditions.[29]

In fact, the nitro groups in nPAHs have a huge influence on the photochemistry of these aromatic systems. The photolabile ($-NO_2$) groups in nPAHs, enhances the ability of the compounds to absorb solar radiation and this has a significant effect with regards their atmospheric reactions, lifetimes and fates.[1] Also, the extended conjugation found in polycyclic aromatics ensures electron charge is easily delocalised through the system which further enables adsorption of sunlight.[45] Initially, only secondary photochemistry phenomena of the triplet states were observed for nPAH compounds due to highly efficient intersystem crossing,[46] however recently published work provides time scales for primary photoinduced events in 9-nitroanthracene.[38] The photochemical behaviour of nPAHs in different phases has been probed in the literature.[20,38,46] 1-Nitronaphthalene (1NN) has been utilized as a model nPAH to understand photosensitized reactions in aqueous solutions[20,25] and photochemical studies on particle associated nPAHs in a model system have also been investigated.[37] In this thesis, nitronaphthalene analogues will be utilized to investigate the photochemical behaviour of nPAHs at carbon surfaces. The influence that the structure of the nPAH analogue and the carbon substrate have on the photochemical behaviour of the nPAH will be probed, as well as a comparison with the photochemical behaviour of the nPAHs in solution. By carrying out photodegradation studies of nPAHs in model systems, it is hoped that a fuller understanding of the atmospheric chemistry of these environmental pollutants can be attained.

Atmospheric reactions involving nPAHs are of utmost importance as they behave as sinks for other atmospheric components, affecting their lifetimes and the atmospheric component makeup.[47] Reactions involving nPAHs greatly influence the chemistry of the atmosphere meaning it is imperative that we understand as much about their behaviour and transformations as is possible. The potential for transformations of nPAHs in atmospheric conditions is immense but only a selection of these transformations are summarized in the following section. Firstly the photodegradation of nPAHs is discussed as this is their major loss pathway. This section includes insight into nPAHs particle phase transformations and

the effect of the associated surface and the nitro group on nPAH photodegradation. Secondly the non-photochemical transformations of nPAHs are discussed. Interactions involving nPAHs can occur in many contexts which include interactions following emission, transportation, deposition or uptake by vegetation.

In the environment, nPAHs undergo various chemical reactions including photochemical reactions when exposed to light.[16] However a limited understanding of the phototransformation mechanisms exists and the ultimate fate of nPAHs in the environment remains uncertain.[2,13] The most probable fate of such compounds is photodecomposition.[2,48] It has been shown that photodegradation is the dominant loss process for gaseous nPAHs in the atmosphere[2,9,49] and it is largely agreed that photodegradation is the major chemical pathway for the loss of larger particle bound nPAHs also.[1] nPAH decomposition has been studied in solution and on particles.[2]

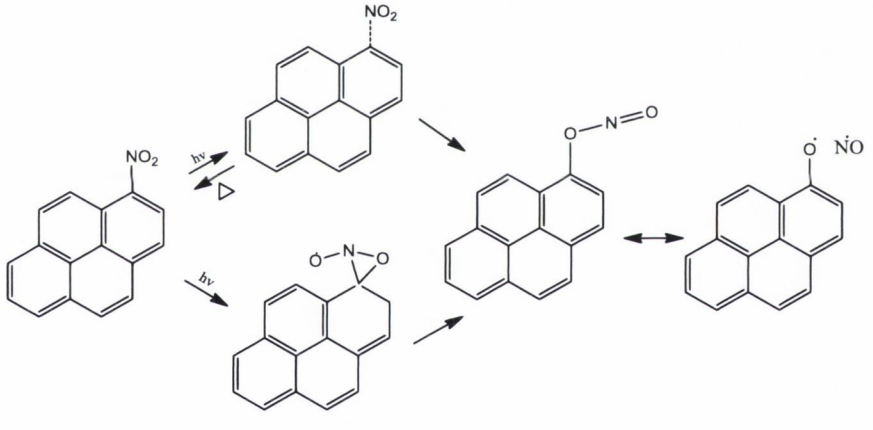

Scheme 1.3. Photochemical degradation pathways of 1 nitropyrene.[2]

In 1966, Chapman proposed a nitro to nitrite photo rearrangement as the photodegradation loss process for nPAHs.[50] Upon absorbing light, the nitroarene is rearranged to the corresponding arylnitrite with subsequent elimination of NO and the formation of a reactive phenoxy radical as depicted in Scheme 1.3. which shows the photochemical degradation of 1-nitropyrene.[1-3,51] Further reactions of the reactive phenoxy radical are likely to form quinones or other oxidized species, as has been shown in the literature.[3] Studies reporting the detection of oxyl radicals which advocated the proposed mechanism of formation of nitrites in the photochemically induced rearrangement of nitrogroups have been published.[52] There were two mechanisms for the nitro to nitrite rearrangement put forward

by Chapman, which were a dissociation-recombination mechanism and an intramolecular mechanism.[29,50] The intramolecular mechanism which occurs in concerted fashion is discussed further by Stewart *et al.*[10] From the literature, it is apparent that the mechanism for photodegradation is complicated and probably involves many different organic components which accelerate nPAH decay.[28] Further discussions on this mechanism and a later mechanism postulated by Hamanoue have also been reported.[38,53-55] Modeling of nPAH decay in the atmosphere has been reported in the literature, generally carried out using outdoor smog chamber experiments.[8,51]

Photochemical reactions of nPAHs occur both on the surface of particulate matter and inside water droplets, with the lifetime of the particulate associated nPAHs being significantly longer than the lifetimes of nPAHs in liquid.[45] However there are many factors to consider; reaction rates, mechanisms and products of photochemical transformations of particle bound nPAHs depend on the structures of the absorbed compound and are also greatly influenced by the physical and chemical nature of the surfaces onto which they are adsorbed.[1-2,29] This conclusion can be drawn from investigations which show tremendously different degradation behaviours when nPAHs were absorbed onto various substrates.[1-2] For example, under similar conditions the half-life of 1-nitropyrene was shown to be 0.5 h, 0.8 h 14 h and 6 days on wood soot, diesel soot, glass and on silica, respectively.[2,4,56]

For surface-bound nPAHs, there is a wide variation in degradation rates as the physical and chemical characteristics of the surface such as their colour and carbon content have a profound effect on the photodegradation of the adsorbed nPAH. During photolysis darker materials absorb the light and protect the adsorbed molecules from photodegradation whereas this is not true for lighter coloured surfaces.[7,47] In fact, faster degradation has been shown to occur on white substrates, despite them absorbing the least radiation.[45] For example PACs on graphitic coal ash have been shown to degrade slower than compared with PACs adsorbed on other soot particles.[2,45,57] It has been shown that heterogeneous degradation processes are inhibited on carbonaceous material when compared to reactivity in the gas phase, this has been attributed to physical properties such as the high surface area and porosity of the carbon material although it remains under debate.[58]

It is also known that photodegradation of nPAHs varies in differing solvents and that the photoproducts formed are consequently affected. A number of groups have presented the photoreaction kinetics and effects of solvent and orientation/position of the nitro group on the photodegradation rate of nPAHs.[16,30] Highly oxidizing solvents lead to the occurrence of free radicals which induce quicker photodegradation.[30] In general, the more polar the solvent, the faster the degradation process for PAHs.[59] A comparison of the photostability of PAHs and nPAHs in different solvents showed that decomposition of nPAHs was always faster than the corresponding parent PAH.[29] The most frequently observed photoproducts were quinones, while further reactions of degradation products included oxidation, fragmentation and reduction.[29] Photodegradation of nPAH in solution are also thought to proceed via a nitro-nitrite rearrangement, this is as a result of the photoproducts obtained following the irradiation of dinitropyrenes in literature reports.[13]

It has been proposed that photoreactivity, along with biological activity of nPAHs is affected by the orientation of the nitro group moiety.[3,10,60-61] Photolysis of nPAHs in solution have been shown to be dependent on the conformation of the molecule.[2,28] Chapman postulated a correlation between how labile nPAHs are towards photochemical degradation and the out of plane arrangement of their nitro groups.[50] This was probed by Warner *et al.* via irradiation of nPAHs in solution and adsorbed onto surfaces.[3] Warner concluded that not all of the nPAHs in solution displayed a relationship between the photodegradation and nitro group orientation, and also the surfaces used appeared to have a greater influence on the photodegradation of the nPAHs absorbed onto surfaces degradation than the structure of the nPAH. Feilberg *et al.* also discussed the importance of the orientation of the nitro group in nPAHs.[28] Through measurement of the photolysis of nitronaphthalenes, it was found that 1NN degraded considerable faster than 2NN during gas phase photolysis and that the rate of gas phase photolysis of nitronaphthalenes was shown to be dependent upon the orientation of the nitro group relative to the aromatic plane. In simple terms, this work suggested that if the nitrogroup is in the same plane as the aromatic moiety, this incurs stability towards photolysis, whereas if the nitro group is out of the aromatic plane, photolysis occurs.[28]

Photodegradation also occurs via heterogeneous reactions with atmospheric species other than hydroxyl radicals, such as NO_3 and O_3. Night time reaction via NO_3 radical attack and particle oxidation by O_3 are known as processes which transform particle associated nPAHs in the atmosphere, however their contributions to the transformations of nPAHs are relatively minor when compared to the former photodegradation pathway.[1-2]

In the particle phase, and following photodegradation via heterogeneous reactions with atmospheric oxidants, the major transformations of nPAHs include photosensitized photolysis and the photogeneration of radical species.[45] These reactions occur on the surface of particles and also within liquid droplets. Vione *et al.* presents a review of the photochemical reactions which occur in the aqueous and particulate phase in the troposphere.[45] It has been shown that when PACs are irradiated in the absence of oxygen, transformations such as photodimerisation occur whereas irradiation under normal atmospheric conditions leads to photodegradation.[45] Atmospheric aerosols contain quite a significant amount of photosentisizers (PAH degradation products) which can induce degradation of nPAHs following absorption of radiation, providing another pathway for transformations of nPAHs.[45] Finally, nPAHs can undergo photoreduction and multiple α-fragmentation.[29]

Transformations undergone by PAHs and nPAHs are not exclusively photochemical and some other transformations which they undergo include the formation of nPAHs under dark conditions and microbial degradation of nPAHs. These transformations of nPAH have been less well studied than their photochemical processes due to the smaller contribution they make to the overall transformations of nPAHs. The work which has been carried out on these transformation processes has mainly focused on PAHs. Dark nitration enables the transformation of PAHs to nPAHs in the atmosphere. HNO_2 formed via photo induced processes proceeds to nitrate activated PAHs via a dark process.[45] The dark nitration of PAH by O_3 has also been shown in the literature and has been found to be a fast process under simulated atmospheric conditions.[62] A half-life of 0.62 hr for BaP is reported following exposure to 190 ppm O_3.[7] However, huge significance has not been placed on this transformation pathway by many researchers.[63-65] Some knowledge of transformations of key PAHs via electrophilic reactions exists which links electron-donating substituents on

PAHs to increased transformation rates and electron withdrawing substituents such as nitro groups to decreased rates of transformation.[1,14,30] Such decreased transformation rates draw attention to the significant influence that compounds such as nPAHs could have in the atmosphere due to persistence.[1] Again, the importance of understanding the reactions and interactions of nPAHs in the atmosphere is highlighted.

The microbial degradation of PACs is an important process to understand as it plays a pivotal role in the environmental fate of these compounds. The ubiquitous nature of PACs and their high persistence in soil has meant that their biodegradation has been investigated thoroughly.[31,66] Recently, Johnsen *et al.* investigated the microbial degradation of PAH in soil.[66] PAH are hydrophobic and with increasing molecular weight become unavailable for microbial degradation as microbial decomposition can only occur in aqueous environments.[30] Therefore, accumulation in the solid phase is promoted in soils. In general, aqueous solubility (and therefore bioavailablilty) decreases with increasing molecular mass.[66] This makes microbial degradation a less effective/efficient pathway for high molecular weight PACs than low molecular weight compounds. It has been shown that this rationale holds for PAHs in solution, in solid form and adsorbed onto surfaces.[30] The metabolic aspects of PAH degradation have been reviewed and demonstrate the importance of this transformation process due to the extensive soil contamination caused by the industrial revolution near large urban areas.[66] These studies bring to light the biochemical persistence of PAC's and draw attention to the benefits of gaining a more detailed understanding of these environmental pollutants.

1.2.5. Influence and health effects of nPAHs

In recent years, concern has mounted regarding the possible adverse health effects of atmospheric pollutants with particular attention on carcinogens in ambient air. PAHs were amongst the first atmospheric pollutants to be identified as being carcinogenic and their high concentrations in ambient air have heightened this concern.[7,9] Research into PAHs inadvertently began as early as 1915 when Japanese scientists discovered the carcinogenic properties of coal tar extracts in animal tests which produced malignant tumours.[67] Interest in this family of compounds was reignited in the 1980's when their mutagenic properties were confirmed by a bacterial assay, the Ames *Salmonella typhimurium* Reversion Assay

which is a short-term bacterial analysis that detects chemical mutagens.[1,4,14,16,39,68-69] This test identified nPAHs as a group of potent direct acting mutagens, of which many of the compounds were also shown to be carcinogenic. It has been calculated using this assay that nPAHs are responsible for 8-25% of the total mutant activity of particulate matter in the atmosphere.[39] As a direct result of the proven mutagenic and carcinogenic properties of nPAHs there has been great interest in these environmental pollutants, which has persisted to the present day as they continue to be investigated as widespread atmospheric pollutants in urban and industrial environments.[3,9,16,39,51] It has been shown that highly condensed PAHs with four or more rings have significant human health effects and exert a wide range of mutagenic and carcinogenic effects on animals and microorganisms.[2,30] With regards the influence and effects of PACs, nPAHs are an extremely important category of derivatives, especially considering nPAHs are known to have a greater toxicity and carcinogenic potential than unsubstituted PAHs; for example many nPAHs have been shown to be more mutagenic than their parent PAHs in the Ames test.[2]

The carcinogenic potential of PACs has been demonstrated in animals, plants and humans, which is unsurprising as PAHs and nPAHs have been shown to be indirect- and direct-acting mutagenic compounds, respectively.[19,39,70] It is believed that the most carcinogenic PAHs are those with lower volatility (4-5 rings) as they can be most easily introduced into the human body. These compounds are almost exclusively associated with particulate matter in the air. Owing to this, it is believed that particle associated nPAHs are responsible for a number of respiratory diseases such as pharynx cancer and lung cancer.[23,39,69] However, nPAHs are also thought to be particularly important for other cancers, such as cancer of the bladder[68] and a number of tumourigenicity studies have indicated that both PAHs and nPAHs are important in the development of lung and liver carcinomas.[71-73] Tokiwa *et al.* investigated the effects of nPAHs on human health by examining resected lung tissue samples of lung cancer patients.[19] The nPAHs found included 2-nitrofluoranthene (2NF), 3-nitrofluoranthene (3NF) and 1-nitropyrene (1NP). However, work carried out examining lung tumours from rats exposed to diesel engine emissions suggested that the associated particles also had some influence on causing and sustaining the disease.[74] Studies have also been carried out which investigate DNA adduct formation by PAHs and nPAHs.[12,75-76] Fu *et al.* looked at structure-activity relationships of nPAHs

and DNA and correlated the structural and electronic features of nPAHs with their biological activities.[77] They proposed that the orientation of the nitro group in a compound can largely affect its metabolism.

nPAHs are direct acting mutagens and are thought to account for a significant portion of the mutagenicity of ambient air and the particulate matter therein.[1] A mutagen is something which can induce or increase the frequency of mutation within an organism. It has been shown that in diesel particulate, 40% of the direct acting mutagenicity has been attributed to nPAHs.[10] Bioassay directed chemical analyses have shown that nPAHs contribute significantly to the direct-acting mutagenicity of ambient air.[1,26] Other work by De Raat *et al*, involved the application of several different bacterial strains to test ambient air particles and coal fly ash.[65] It was found that the most mutagenic subfractions were those containing unsubstituted mononitrated nPAHs.

A popular way to measure the toxicity of PAHs is via the toxicity equivalency factor (TEF) evaluation, which is the sum of TEF values and concentration values of PAHs.[9] Petry *et al.* used TEFs to assess the risks of exposure of airborne PAHs in both occupational and natural environments.[78] TEFs were also used by Halek *et al.* to estimate the annual lung cancer incidences in Tehran in 2005 which were caused by PAH compounds at 58 people per million.[79] Collins *et al.* calculated PEFs for PAHs and nPAHs using a number of bioassays.[80]

The particle size distributions of nPAHs in the ambient atmosphere can have a huge influence on how they affect human health. This is because their size distribution determines their deposition behaviour. It has been reported that coarse particles are deposited in the nasal region but finer particles are deposited in pulmonary alveoli, with nPAHs being detected in fine particles.[23] This leads to much higher mutagenicity in fine rather than course particles.[19] nPAHs are important pollutants due to their higher water solubility and thus bioavailability when compared to PAHs. Also the phototoxicity observed in nPAHs is not exhibited by PAHs. It has been shown that highly condensed PAHs with four or more rings have significant human health effects and exert a wide range of mutagenic and carcinogenic effects on animals and microorganisms.[2,30] Lower molecular

weight PAHs, with the exception of naphthalene, have been associated with relatively lower toxicity.[9]

Exposure to nPAHs can occur in a number of ways including inhalation and internal adsorption via ingestion. The inhalation of air particles with adsorbed nPAHs is an extremely important exposure route as it happens continually to large populations in urban and industrial areas.[28] Exposure via inhalation is reliant on atmospheric conditions, concentrations of nPAHs in the air and their distribution between the gas and particulate phases.[7] The size of the associated particle is also important and as discussed previously the particle itself may have a huge influence on the fate of the inhaler. nPAHs can be internally adsorbed through food, particularly through grains, and also via meat, fish and leafy vegetables.[81] Internal adsorptions from water consumption and even via skin contact are other, less important exposure routes.[9] Following adsorption, PAHs are transported to the fatty tissues of the human body, they are then stored in fat tissue or in the liver and/or kidneys and can undergo accumulation due to repeated and long term exposure.[9] While some of these reports follow PAHs exposure pathways, it is logical that nPAHs will follow similar routes.

Exposure to nPAHs can occur in a number of environments including occupational and environmental exposure. Occupational exposure to nPAHs occurs in industrial settings such as coke manufacturing factories and steel work plants.[28] It has been shown in epidemiological studies that workers exposed to PAC/diesel exhausts have excess risk of developing cancer of the lung and bladder.[68,74] Environmental exposure data shows nPAH pollution in urban areas is mostly caused by residential heating and diesel engine usage.[9] Vehicle emissions are also main sources of nPAHs in many cities. Other human exposure routes to nPAHs include fumes from cooking oil, wood fires and kerosene heating, exposure to emissions from industrial plants, cigarette smoke, agricultural burning, waste incineration and diesel exhausts and of course exposure to PACs in ambient air.[9]

As a source of nPAH exposure, diesel exhaust particles are especially important. They contain both PAHs and nPAHs and contribute massively to urban pollution.[28] The exposure of taxi drivers to particulate air pollution and nPAHs in Shenyang, China, was recently

investigated. Risk analysis of exposure to nPAHs have been investigated and suggest a 0.49 risk per million of developing cancer due to 2-nitrofluorene based on metabolic activity of this compound and its concentrations in large cities.[82] Considering other nPAHs are more abundant and more potent mutagens, this risk factor can be taken as an underestimation.[82] Moreira *et al.* presents a review of nPAHs which includes the occurrence and biological activities of nPAHs, methods for their analytical determination and the use of biological markers for assessing human exposure.[36] This review highlights that a vast understanding and knowledge of the physical and chemical properties of these compounds is required to efficiently conduct environmental monitoring, exposure regulation, molecular epidemiology, air quality management and overall reduction of impacts.[11,36]

1.2.6. Fate

Following release into the atmosphere, nPAHs undergo a variety of atmospheric processes through which their transport, distribution, removal and degradation can occur. While resident in the atmosphere, PAHs may undergo chemical and photochemical transformations, as discussed in previous sections. The atmospheric behaviour of particle bound PAHs and nPAHs is massively dependant on the behaviour of the particles themselves, and so the atmospheric residence times, transport and removal of particle associated nPAHs is a function of the associated particle size.[6-7,28] For example, large coarse particles (> 3 μm) and very fine particles (> 0.1 μm) have limited residence times due to removal by deposition and coagulation respectively. The accumulation size mode encompasses the particles between these sizes (>0.1 μm and <3 μm) and this is the mode with which particle phase PAHs and nPAHs are predominantly associated. Deposition from this mode occurs slowly and particles may remain airborne for extended periods.[6] Removal mechanisms from this fraction are not efficient and particles are prone to long range transportation with distances of up to 1000 km possible. PAHs and nPAHs have been identified in remote non-urban locations such as arctic and marine environments, with explanations pointing towards aerial transport from distant anthropogenic sources.[83-85]

As discussed above, nPAHs undergo photolysis in the atmosphere. For example 1NN undergoes photolysis in less than 1h in the atmosphere, meaning that its long range

transport would be thought to be highly improbable. However significant amounts of 1NN and 2NN have been detected in Antarctic airborne particulate matter, which has been explained by gas phase nitration of naphthalene followed by partitioning onto low temperature particles in these regions.[25] Transport of particle phase PACs is limited by reactions, whilst dilutions of particle phase PACs can occur during transportation via redistribution into the gas particle partition. However, generally the transportation of PACs has been shown to be extensive and the exchange between phases recognized as another atmospheric process undergone by nPAHs.[7] Extensive transportation and the persistence of PACs in remote locations, confirms that information and knowledge about these increasingly ubiquitous compounds is required to understand their fate and behaviour.

nPAHs are present in urban samples and are also found in soil and aquatic environments due to dry and wet deposition.[1,39] This highlights nPAHs as important compounds in air pollution research but also in the studies of soil and aquatic systems. Deposition represents a physical removal of nPAHs from the atmospheric environment and this atmospheric process is significant from a public health perspective as it introduces nPAHs into environments with which humans and animals intimately interact. Processes which govern dry deposition of particle associated nPAHs include diffusion, impaction and sedimentation of particles. This deposition method also depends on turbulence in the atmosphere, the chemical properties of the compound being deposited and the nature of the surface onto which deposition is occurring.[7,28] Wet deposition occurs when PACs in the gaseous phase partition into rain by cloud scavenging, whereas particle associated PACs are removed within clouds via diffusion and impaction mechanisms. It has been shown that precipitation removes particle associated compounds more efficiently than gas phase compounds, with PACs having been identified in rain, snow and fog.[7]

Along with distribution, transportation and deposition, nPAHs undergo other atmospheric processes in the environment. As discussed in Section 1.2.4. nPAHs undergo reactions, both photochemical and chemical, which can lead to their degradation, rearrangement and/or conversion.[9] These transformations include photoreduction of the nitro moiety, nucleophilic photosubstitution and hydrogen abstration.[4] Uptake by vegetation, microbial degradation and potential biomagnification are other probable atmospheric processes

undergone by nPAHs.[4,28] PAHs and nPAHs have been found in tree bark pine needles and forest canopies. A model by Simonich and Hites predicts that approximately 40% of PAC emitted into a region will be removed by vegetation.[86]

There are a number of problems which are encountered when trying to investigate nPAHs. The low concentrations of nPAHs measured in environmental samples (~pg/m^3) ensure these contaminants can be difficult to monitor and require extremely sensitive detection techniques. A common method used to sample nPAHs is their collection on sorbent resins and filters, followed by extraction and analysis, however the associated difficulties with this technique include the complex mix of compounds being sampled and the relatively low concentrations of nPAHs within this mixture.[9] Volatilization and further reaction during sampling can also occur. Whilst hundreds of PACs have been identified in polluted atmospheres, the majority of these are particle associated compounds due to problems in gas phase sampling, where extremely large sampling volumes are required. However, it is important to point out that it is believed particulate associated organics are more plentiful and more harmful to human health than those in the gaseous phase.[7]

As is the case with much of the literature on PACs, much more work has been carried out on the more abundant PAH compounds that the nitro derivatives, which is also the case for nPAHs adsorbed onto carbonaceous surfaces. This paragraph focuses on the literature relevant to the formation and decay of nPAHs on soot and carbon surfaces. An investigation into the formation of nPAHs adsorbed on diesel soot particles was carried out by Carrara *et al.* via the interaction of PAH coated soot aerosol with NO_2 at different temperatures and analysis of the reaction products.[26] This work showed an artificial model system being used in order to gain understanding of atmospheric reactions and the results showed that formation of nPAHs increased linearly with time for all concentrations of NO_2. As for the temperature dependence, it was also observed that above 373 K, a decrease in nPAH formation was observed which was attributed to a relocation of the particle associated PAHs into the gaseous phase.[26] The photodegradation of diesel soot and wood smoke particle associated nPAHs via exposure to sunlight was carried out by Fan *et al.*, where it was found that degradation occurred faster on wood smoke particles than on the diesel soot particulate.[2] It is known that the photodegradation of nPAHs on surfaces is

strongly dependent on the physical and chemical nature of the surface onto which they are adsorbed.[2] A change in the nature of the carbonaceous particle has been shown to strongly influence the degradation of adsorbed PAHs and the same can be said to be true for nPAHs on carbonaceous surfaces.[2,58]

1.3. Carbon surfaces

1.3.1. Properties of Carbon

Carbon is stabilized in a number of molecular configurations called allotropes, including diamond, graphite, amorphous carbon, fullerenes and carbon nanotubes and the physical properties of carbon vary widely depending on the allotropic form. Diamond and graphite are crystalline forms of carbon with very different properties as shown in Table 1.1. For example, diamond is the hardest naturally occurring material whereas graphite is relatively soft; diamond is highly transparent whereas graphite is black and opaque. Diamond consists of carbon bonded to other carbons with tetrahedral coordination. Graphite has been likened to parallel sheets of chicken wire and consists of layers of carbon atoms bonded in regular hexagons with the layers held together by van der Waals forces.[87] Amorphous carbon (a-C) is essentially a form of carbon which is non-crystalline, and comprises of an irregular arrangement of carbon atoms with no long range order. Fullerenes are another allotrope of carbon which are made up of hollow clusters of carbon atoms in dome-like formations. Carbon nanotubes are single or multiple layers of graphite sheets rolled into cylindrical tubes which have varying diameter, length and termination pattern. Despite forming an enormous variety of compounds, most carbon allotropes are highly resistant to chemical reaction, and this stability is due to the strong C—C bonds that hold these structures together.

Table 1.1. Properties of diamond, graphite and amorphous carbon.[88-89]

	sp^3 (%)	Band Gap (eV)	Bond Energy (eV)
Diamond	100	55	3.68
Graphite	0	0	4.93
a-C	0 – 90	0 – 2.5	

It is the bonding of carbon to its neighbouring atoms which determines the allotrope of carbon obtained and this element has the ability to form two, three or four coordination bonds. Diamond is made up of tetrahedrally bonded carbons, which are often referred to as sp^3 centres; graphite, fullerenes and carbon nanotubes consist of sp^2 carbon sites in different arrangements, and a-Cs can have a mixture of sp^3, sp^2, sp and incorporated hydrogenated sites. a-Cs are a family of disordered carbons and are particularly useful from a technological viewpoint since their properties can be tuned over a wide range of conductivity and hardness and they tend to be relatively easy to integrate into typical fabrication processes.[90] To give an example of the versatility of carbon materials, a ternary phase diagram has been reproduced from Ferrari *et al.* in Figure 1.1., which shows the broad scope of possible compositions of a-Cs enabling an immense variety of applications.[91]

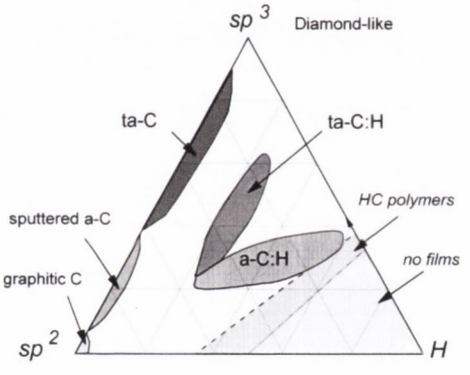

Figure 1.1. Ternary phase diagram of amorphous carbons reproduced from Robertson. [91]

The two key factors that determine the properties and structures of a-Cs are the fraction of sp^3 bonded carbon sites and the heteroatom content (e.g. H or N). The ordering of sp^2 sites is the third significant factor in the ternary phase diagram of a-Cs and is particularly important for the electronic properties of a-Cs.[88]

A detailed analysis of the electronic structure of amorphous carbons is given in the literature.[88,92-94] Briefly, due to the different possible arrangements of carbons, both sigma (σ) and pi (π) bonding states are present. For example, in the sp^3 configuration, a carbon forms a strong σ bond to a neighbouring atom, whereas in the sp^2 configuration, a carbon atom forms σ bonds and π bonds. The σ bonds of all carbon sites form occupied and unoccupied states in the valence and conduction band respectively, which are separated by

a wide σ - σ* gap. π bonds from sp^2 sites form filled and empty π and π* states which have a narrower π - π* gap.[88,95] This concept is illustrated in Figure 1.2. In basic terms, the electronic properties of a-Cs can change from metallic to semiconducting by increasing the sp^3 content. This, in effect, increases the band gap between the conductance and valence band in the carbon material and lowers the conductivity of the material.

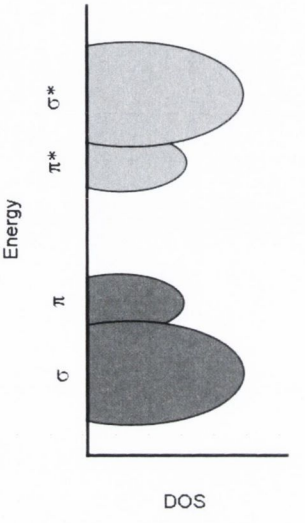

Figure 1.2. Density of states in a-C films as a result of the mixed π and σ states.

1.3.2. Carbonaceous aerosols in the environment

Carbonaceous aerosol constitutes a substantial fraction of the total particulate matter found in ambient air.[96-98] The carbon particulate matter in the atmosphere is made up of three components: organic compounds (PAHs and other hydrocarbons), elemental carbon (soot) and mineral carbon (inorganic carbon compounds).[99-101] Organic carbon is formed via direct emission from combustion sources or secondary condensation reactions whereas elemental carbon is formed exclusively from incomplete combustion processes. Another secondary process, which results in the formation of organic carbon, is the physical or chemical adsorption of gaseous species onto aerosol particle surfaces.[102] Mineral carbon is a primary carbonaceous species found in dust and is mostly made up of carbonates.[100,102] The organic components of carbon aerosols regularly adsorb onto the elemental fraction and result in a complex mixture of carbonaceous aerosols in the atmosphere. In more recent years, research has begun to focus on carbonaceous aerosols in the environment due to the

recognized effects they have on environmental, human health and biological systems.[100] Carbonaceous aerosols are incredibly important from an environmental perspective due to their ability to absorb and scatter solar radiation. These particles can upset the radiative balance by reducing solar radiation reaching the earth or reflecting radiation leaving the earth, processes which have been shown to lead to climate change.[103] Carbonaceous aerosol particles have also received attention as they remain a significant cause of visibility degradation in polluted atmospheres [104-105]

Atmospheric aerosols on which nPAHs are known to react are carbonaceous or soot particles. As discussed previously, carbonaceous particles originating from numerous combustion sources constitute a large percentage of atmospheric particulate and investigations into heterogeneous reactions which occur on these particles could provide valuable insight for chemistry of the polluted atmosphere. One highly important carbonaceous aerosol is the diesel soot particle; these particles are generated in large amounts in urban environments.[101] Diesel soot particles, and their associated pollutants represent a system which could provide valuable insight into the atmospheric chemistry of nPAHs on carbonaceous surfaces. A representation of the complex nature of the diesel soot particle and it's adsorbants (such as sulfates) is given in Figure 1.3.[1]

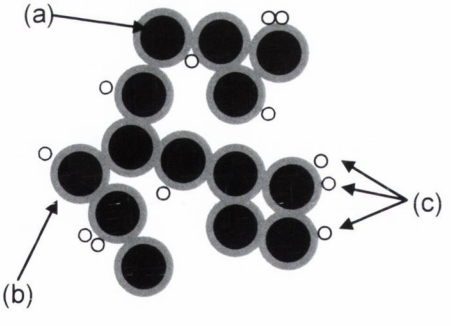

Figure 1.3. Schematic of diesel soot particle showing (a) elemental carbon, (b) surface adsorbed organics and (c) surface sulfates.

1.3.3. a-C as a model surface

Highly graphitic amorphous carbon (a-C) can be thought of as a disordered form of carbon, with a highly irregular arrangement of carbon atoms where sp^2 carbon centres are often arranged yielding graphitic clusters. It has been shown that a-Cs constitute the main component of soot, which is unsurprising as these materials are obtained via the heating of

carbon rich materials in limited air supply. We have decided to utilize a-C thin films as model surfaces for the nPAH reactions that occur on carbonaceous particles in the atmosphere. Part of the reason for choosing a-C as a surface for reaction was the versatility of the material. As discussed in Section 1.3.1, a-Cs consist of a mixture of bonding types, which impart certain characteristics onto the thin film. Another aspect of a-C films that changes is the degree of clustering of the sp^2 phase which can have a massive influence on the optical, mechanical and electronic properties of the surface. a-C films can be produced using evaporation or sputtering deposition methods and the composition of the film can be controlled and tuned depending on the preparation conditions. This means that, for example, the electronic properties of a-C films can range from semi-metallic to conducting. The ability to selectively choose the composition of a-C films has meant a plethora of applications are possible, in areas such as electronics, sensors, biomedical devices and catalysis.[106-107]

In this work, it is hoped that using a-C films as a model surface will allow us to probe the interfacial relationship of nPAHs at carbon surfaces in detail. Not only will adsorption onto carbon surfaces be investigated but the photodegradation of nPAHs associated with carbon particulates in the atmosphere will also be studied. Little is known about the photostability of nPAHs on atmospheric aerosols and further knowledge could greatly benefit understanding of the chemistry of polluted atmospheres. It has been proposed that, for carbonaceous materials, carbon content is one of the main factors in determining the photostability of adsorbed nPAHs [1-2] and so the ability to control the carbon content by using amorphous carbon thin films as our model surface will enable us to probe the photostability of adsorbed nPAHs more thoroughly.

1.4. Rationale and Methodology

1.4.1. Rationale

The rationale behind this work was to design a functional interface for fundamental studies of nPAH chemistry. a-C thin films were utilized as model surfaces to understand the environmentally relevant interactions of polycyclic pollutants with carbonaceous aerosols in the atmosphere. The interplay between PACs and carbon particulate in the environment

is not fully understood and this work aims to investigate their relationship in a number of ways. Firstly, by probing the reactions of structurally different nPAHs at amorphous carbon surfaces we can provide insight into the reliance on molecular conformation of nPAH adsorption. Secondly, by investigating a number of different amorphous carbon surfaces, a rational proposal of the influencing factors on adsorption of nPAHs on carbonaceous aerosols based on the electronic properties of both the model carbon surface and nPAHs can be discussed. This work aims to attain information on the role that the properties of the surface play in surface mediated nPAH adsorption reactions. We intend to gain an understanding as to which properties are important in determining the fate of nPAHs at surfaces. The photodegradation of nPAHs on particulate matter is an environmentally topical reaction as photodegradation constitutes the major loss pathway, therefore, a preliminary analysis of the photochemistry of some nPAHs on a-C surfaces is provided. Finally, a number of other functional surfaces that have been developed during this work, but which are not related to nPAH chemistry, will be examined under the broader umbrella of developing functional surfaces for environmental applications.

1.4.2. Methodology

Carbon surfaces with well-defined structure and composition will be utilized as model surfaces for carbonaceous or soot particles as found in the atmosphere. Details of the preparations of these surfaces will be presented in the experimental sections of the relevant chapters. In order to covalently attach nPAHs to carbon surfaces, fuctionalization using diazotiation reactions will be availed of. The methodology utilized for functionalization of nPAHs onto substrates will involve synthesizing or purchasing amine derivatives of the nPAHs and performing a diazotization reaction to them. This provides the reactive functionality of the diazonium group (N_2^+) which has been shown to spontaneously covalently graft onto surfaces.[108-110]

Aryldiazonium salts have served historically as reagents in transformations such as the Sandmeyer and Heck-Matsuda reactions,[111-112] however in recent years there has been increased interest into their applications for surface modification. Aryldiazonium salts are versatile reagents that can be utilized to modulate the surface chemistry of metals, semiconductors, carbon materials and polymers,[113-114] by forming strong covalent linkages

between the grafted compound and the substrate. The grafting process can be achieved via electroreduction of the diazonium moiety and loss of dinitrogen, followed by attachment of the aryl moiety to the surface through a covalent bond.[113,115-117] More recently, it was found that covalent attachment could occur spontaneously from solution;[108,118-121] this type of approach is advantageous since it does not require an electrical contact to be made to the substrate material and can therefore be applied to a wide range of substrates, including poor conductors, nanostructured materials and nanoparticles in suspension.[117,121-125]

While the electrochemical reduction of aryl diazonium salts followed by covalent attachment to surfaces such as carbon, copper, nickel, iron, silicon and even carbon nanotubes is a well-documented methodology, not as much is known about the spontaneous reaction.[117,126-129] A schematic of spontaneous grafting is given in Figure 1.4. Spontaneous grafting of aryldiazonium salts for the covalent attachment of organics to surfaces will provide a versatile methodology for implementation. This method has achieved effective covalent grafting on metallic and semiconducting substrates and offers a strong linkage between the grafted compound and the substrate. Conditions can then be tuned to attain desired coverage.[108-110]

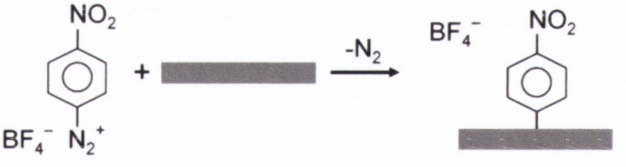

Figure 1.4. Schematic of spontaneous grafting of an aryldiazonium salt onto a surface.

The most widely used method for the preparation of diazonium salts involves reaction of aromatic amines with sodium nitrite in the presence of an acid. The mechanism of formation of the diazonium functionality involves the generation of the nitrosonium ion, followed by nitrosation of the amine and tautomerism producing the diazonium salt.[111] Diazonium salts are generally unstable at room temperature as the N_2^+ triple bond tends to be lost as nitrogen gas. However, tetrafluoroborate salts of the diazonium compounds which can be isolated at room temperature are relatively stable and will be utilized in our syntheses.

1.5. Applications of model interfaces in other fields

This thesis is entitled "Design and characterisation of functional interfaces for fundamental studies of nitro-polycyclic aromatic hydrocarbon chemistry" however, a number of model interfaces have been designed and investigated which are not connected to fundamental studies of nPAH chemistry. These interesting model interfaces represent a body of work which was also carried out during my research and will be discussed in the latter chapters of this thesis. Firstly, bioactive model interfaces which have been developed using diazonium chemistry will be presented. Secondly, fluorine-fluorine interactions for extraction and separation technologies are probed. This work focuses on trying to understand and harness adsoption at an interface. Introductions to these topics will be given in the corresponding chapters. All of the model interfaces presented in this work have real world potential applications which illustrate the relevance of the work.

1.6. References

(1) Finlayson-Pitts, B. J.; Pitts, J. J. N. In *Chemistry of the Upper and Lower Atmosphere*; Academic Press: San Diego, **2000**, 436.

(2) Fan, Z.; Kamens, R. M.; Hu, J.; Zhang, J.; McDow, S. *Environmental Science & Technology* **1996**, *30*, 1358.

(3) Warner, S. D.; Farant, J.-P.; Butler, I. S. *Chemosphere* **2004**, *54*, 1207.

(4) Benson, J. M.; Brooks, A. L.; Cheng, Y. S.; Henderson, T. R.; White, J. E. *Atmospheric Environment* **1985**, *19*, 1169.

(5) Harvey, R. G. *Polycyclic Aromatic Hydrocarbons*; Wiley-VCH, Inc: New York, **1997**.

(6) Harrison, R. M.; Smith, D. J. T.; Luhana, L. *Environmental Science & Technology* **1996**, *30*, 825.

(7) Baek, S. O.; Field, R. A.; Goldstone, M. E.; Kirk, P. W.; Lester, J. N.; Perry, R. *Water Air Soil Pollution* **1991**, *60*, 279.

(8) Fan, Z.; Chen, D.; Birla, P.; Kamens, R. M. *Atmospheric Environment* **1995**, *29*, 1171.

(9) Lee, B.-K.; Vu, V. T. *Sources, Distribution and Toxicity of Polyaromatic Hydrocarbons (PAHs) in Particulate Matter*, **1995**.

(10) Stewart, G.; Jiao, Y.; Valente, E. J.; Fu, P. P.; Li, T.; Hu, Z.; Yu, H. *Journal of Photochemistry and Photobiology A: Chemistry* **2009**, *201*, 39.

(11) Ravindra, K.; Sokhi, R.; Van Grieken, R. *Atmospheric Environment* **2008**, *42*, 2895.

(12) Carrasco, E. A.; Campos-Vallette, M.; Leyton, P.; Diaz, G.; Clavijo, R. E.; García-Ramos, J. V.; Inostroza, N.; Domingo, C.; Sanchez-Cortes, S.; Koch, R. *The Journal of Physical Chemistry A* **2003**, *107*, 9611.

(13) Morel, M. C.; Alers, I.; Arce, R. *Polycyclic Aromatic Compounds* **2006**, *26*, 207.

(14) Nielsen, T. *Environmental Science & Technology* **1984**, *18*, 157.

(15) Reisen, F.; Arey, J. *Environmental Science & Technology* **2004**, *39*, 64.

(16) Stewart, G.; Smith, K.; Chornes, A.; Harris, T.; Honeysucker, T.; Yu, H. *Environmental Chemistry Letters* **2010**, *8*, 301.

(17) Pitts Jr, J. N.; Grosjean, D.; Mischke, T. M.; Simmon, V. F.; Poole, D. *Toxicology Letters* **1977**, *1*, 65.

(18) Pitts Jr, J. N.; Van Cauwenberghe, K.; Grosjean, D.; Schmid, J.; Fitz, D.; Belser, W.; Knudson, G.; Hynds, P. *Science* **1978**, *202*, 515.

(19) Tokiwa, H.; Nakagawa, R.; Morita, K.; Ohnishi, Y. *Mutation Research* **1981**, *85*, 195.

(20) Brigante, M.; Charbouillot, T.; Vione, D.; Mailhot, G. *The Journal of Physical Chemistry A* **2010**, *114*, 2830.

(21) Heeb, N. V.; Schmid, P.; Kohler, M.; Gujer, E.; Zennegg, M.; Wenger, D.; Wichser, A.; Ulrich, A.; Gfeller, U.; Honegger, P. *Environmental Science & Technology* **2008**, *42*, 3773.

(22) Arey, J.; Zielinska, B.; Harger, W. P.; Atkinson, R.; Winer, A. M. *Mutation Research Letters* **1988**, *207*, 45.

(23) Kawanaka, Y.; Matsumoto, E.; Sakamoto, K.; Wang, N.; Yun, S.-J. *Atmospheric Environment* **2004**, *38*, 2125.

(24) Phousongphouang, P. T.; Arey, J. *Journal of Photochemistry and Photobiology A: Chemistry* **2003**, *157*, 301.

(25) Maddigapu, P. R.; Minero, C.; Maurino, V.; Vione, D.; Brigante, M.; Charbouillot, T.; Sarakha, M.; Mailhot, G. *Photochemical & Photobiological Sciences* **2011**, *10*, 601.

(26) Carrara, M.; Wolf, J.-C.; Niessner, R. *Atmospheric Environment* **2010**, *44*, 3878.

(27) Shailaja, M.; Rajamanickam, R.; Wahidulla, S. *Toxicological Sciences* **2006**, *91*, 440.

(28) Feilberg, A., *Atmospheric chemistry of polycyclic aromatic compounds with special emphasis on nitro derivatives*, Riso National Laboratory, **2000**.

(29) Cvrčková, O.; Ciganek, M. *Polycyclic Aromatic Compounds* **2005**, *25*, 141.

(30) Dabrowska, D.; Kot-Wasik, A.; Namiesnik, J. *Polish Journal of Environmental Studies* **2008**, *17*, 17.

(31) Edwards, N. T. *J. Environmental Quality* **1983**, *12*, 427.

(32) Mastral, A. M.; Callén, M. S. *Environmental Science & Technology* **2000**, *34*, 3051.

(33) Shen, G.; Tao, S.; Wei, S.; Zhang, Y.; Wang, R.; Wang, B.; Li, W.; Shen, H.; Huang, Y.; Chen, Y.; Chen, H.; Yang, Y.; Wang, W.; Wang, X.; Liu, W.; Simonich, S. L. M. *Environmental Science & Technology* **2012**, *46*, 8123.

(34) Hu, S.; Herner, J. D.; Robertson, W.; Kobayashi, R.; Chang, M.-C. O.; Huang, S.-m.; Zielinska, B.; Kado, N.; Collins, J.; Rieger, P. *Journal of the Air & Waste Management Association* **2013**.

(35) Jacob, J.; Karcher, W.; Belliardo, J. J.; Dumler, R.; Boenke, A. *Fresenius Journal of Analytical Chemistry* **1991**, *340*, 755.

(36) Moreira, J. C.; Barek, J. *Quimica Nova* **1995**, *18*, 4.

(37) Feilberg, A.; Nielsen, T. *Environmental Science & Technology* **2000**, *34*, 789.

(38) Plaza-Medina, E. F.; Rodríguez-Córdoba, W.; Morales-Cueto, R.; Peon, J. *The Journal of Physical Chemistry A* **2011**, *115*, 577.

(39) Tsakas, M. P.; Sitaras, I. E.; Siskos, P. A. *Chemistry and Ecology* **2010**, *26*, 251

(40) Rogge, W. F.; Hildemann, L. M.; Mazurek, M. A.; Cass, G. R.; Simoneit, B. R. T. *Environmental Science & Technology* **1993**, *27*, 636.

(41) Yamasaki, H. K. K., Y.; Miyamoto, H *Environmental Science & Technology* **1982**, *16*, 189.

(42) Pistikopoulos, P.; Masclet, P.; Mouvier, G. *Atmospheric Environment. Part A. General Topics* **1990**, *24*, 1189.

(43) Baek, S. O.; Goldstone, M. E.; Kirk, P. W. W.; Lester, J. N.; Perry, R. *Environmental Technology* **1991**, *12*, 107.

(44) Baek, S. O.; Goldstone, M. E.; Kirk, P. W. W.; Lester, J. N.; Perry, R. *Chemosphere* **1991**, *22*, 503.

(45) Vione, D.; Maurino, V.; Minero, C.; Pelizzetti, E.; Harrison, M. A.; Olariu, R.-I.; Arsene, C. *Chemical Society Reviews* **2006**, *35*, 441.

(46) Collado-Fregoso, E.; Zugazagoitia, J. S.; Plaza-Medina, E. F.; Peon, J. *The Journal of Physical Chemistry A* **2009**, *113*, 13498.

(47) Vione, D.; Barra, S.; de Gennaro, G.; de Rienzo, M.; Gilardoni, S.; Perrone, M. G.; Pozzoli, L. *Annali di Chimica* **2004**, *94*, 257.

(48) Nielsen, T.; Ramdahl, T.; Bjorseth, A. **1983**.

(49) Atkinson, R.; Aschmann, S. M.; Arey, J.; Barbara, Z.; Schuetzle, D. *Atmospheric Environment* **1989**, *23*, 2679.

(50) Chapman, O. L.; Heckert, D. C.; Reasoner, J. W.; Thackaberry, S. P. *Journal of the American Chemical Society* **1966**, *88*, 5550.

(51) Kamens, R. M.; Zhi-Hua, F.; Yao, Y.; Chen, D.; Chen, S.; Vartiainen, M. *Chemosphere* **1994**, *28*, 1623.

(52) Ioki, Y. *Journal of the Chemical Society* **1977**, *10*, 1240.

(53) Hamanoue, K.; Nakayama, T.; Kajiwara, K.; Yamanaka, S.; Ushida, K. *Journal of the Chemical Society, Faraday Transactions* **1992**, *88*, 3145.

(54) Hamanoue, K.; Nakayama, T.; Ushida, K.; Kajiwara, K.; Yamanaka, S. *Journal of the Chemical Society, Faraday Transactions* **1991**, *87*, 3365.

(55) Hamanoue, K.; Nakayama, T.; Amijima, Y.; Ibuki, K. *Chemical Physics Letters* **1997**, *267*, 165.

(56) Holloway, M. P.; Biaglow, M. C.; McCoy, E. C.; Anders, M.; Rosenkranz, H. S.; Howard, P. C. *Mutation Research/Genetic Toxicology* **1987**, *187*, 199.

(57) Behymer, T. D.; Hites, R. A. *Environmental Science & Technology* **1988**, *22*, 1311.

(58) Esteve, W.; Budzinski, H.; Villenave, E. *Atmospheric Environment* **2006**, *40*, 201.

(59) Sigman, M. E.; Chevis, E. A.; Brown, A.; Barbas, J. T.; Dabestani, R.; Burch, E. L. *Journal of Photochemistry and Photobiology A: Chemistry* **1996**, *94*, 149.

(60) Fu, P. P.; Heflich, R. H.; Unruh, L. E.; Shaikh, A. U.; Wu, Y.-S.; Lai, C.-C.; Lai, J.-S. *Mutation Research Letters* **1988**, *209*, 115.

(61) Jung, H.; Heflich, R. H.; Fu, P. P.; Shaikh, A. U.; Hartman, P. *Environmental and molecular mutagenesis* **1991**, *17*, 169.

(62) Lane, D. A.; Katz, M. *Advances in Environmental Science & Technology* **1977**, *8*, 137.

(63) Pitts Jr, J. N.; Paur, H.-R.; Zielinska, B.; Arey, J.; Winer, A. M.; Ramdahl, T.; Mejia, V. *Chemosphere* **1986**, *15*, 675.

(64) Atkinson, R.; Aschmann, S. M. *International journal of chemical kinetics* **1986**, *18*, 569.

(65) De Raat, W.; Boers, J.; Bakker, G.; De Meijere, F.; Hooimeijer, A.; Lohman, P.; Mohn, G. *Science of The Total Environment* **1994**, *153*, 7.

(66) Johnsen, A. R.; Wick, L. Y.; Harms, H. *Environmental Pollution* **2005**, *133*, 71.

(67) Yamagiwa, K.; Ichikawa, K. *The Journal of Cancer Research* **1918**, *3*, 1.

(68) Rosenkranz, H. S.; Mermelstein, R. *Mutation Research* **1983**, *114*, 217.

(69) Von Tungeln, L. S.; Xia, Q.; Herreno-Saenz, D.; Bucci, T. J.; Heflich, R. H.; Fu, P.P. *Cancer Letters* **1999**, *146*, 1.

(70) Jacob, J. *Polycyclic Aromatic Compounds* **2008**, *28*, 242.

(71) Sheu, C.; Dobras, S.; Rodriguez, I.; Lee, J.; Fu, P. *Food and chemical toxicology* **1994**, *32*, 611.

(72) Wislocki, P. G.; Bagan, E. S.; Lu, A. Y.; Dooley, K. L.; Fu, P.; Han-Hsu, H.; Beland, F. A.; Kadlubar, F. F. *Carcinogenesis* **1986**, *7*, 1317.

(73) West, R.; Rowland, K. *Toxicology in vitro* **1994**, *8*, 301.

(74) Rosenkranz, H. S. *Mutation Research/Genetic Toxicology* **1996**, *367*, 65.

(75) Topinka, J.; Schwarz, L. R.; Kiefer, F.; Wiebel, F. J.; Gajdoš, O.; Vidová, P.; Dobiáš, L.; Fried, M.; Šrám, R. J.; Wolff, T. *Mutation Research/Genetic Toxicology and Environmental Mutagenesis* **1998**, *419*, 91.

(76) Talaska, G.; Underwood, P.; Maier, A.; Lewtas, J.; Rothman, N.; Jaeger, M. *Environmental Health Perspectives* **1996**, *104*, 901.

(77) Fu, P. P.; Herreno-saenz, D.; Von Tungeln, L. S.; Hart, R. W.; Lin, S.-D. *Polycyclic Aromatic Compounds* **1994**, *6*, 71.

(78) Petry, T.; Schmid, P.; Schlatter, C. *Chemosphere* **1996**, *32*, 639.

(79) Halek, F.; Nabi, G.; Kavousi, A. *Environmental monitoring and assessment* **2008**, *143*, 303.

(80) Collins, J.; Brown, J.; Alexeeff, G.; Salmon, A. *Regulatory Toxicology and Pharmacology* **1998**, *28*, 45.

(81) Menzie, C. A.; Potocki, B. B.; Santodonato, J. *Environmental Science & Technology* **1992**, *26*, 1278.

(82) Møller, H.; Mellemgaard, A.; Lindvig, K.; Olsen, J. H. *European Journal of Cancer* **1994**, *30*, 344.

(83) Halsall, C. J.; Barrie, L. A.; Fellin, P.; Muir, D.; Billeck, B.; Lockhart, L.; Rovinsky, F. Y.; Kononov, E. Y.; Pastukhov, B. *Environmental Science & Technology* **1997**, *31*, 3593.

(84) Masclet, P.; Hoyau, V.; Jaffrezo, J. L.; Cachier, H. *Atmospheric Environment* **2000**, *34*, 3195.

(85) Vincenti, M.; Maurino, V.; Minero, C.; Pelizzetti, E. *International Journal of Environmental Analytical Chemistry* **2001**, *79*, 257.

(86) Simonich, S. L.; Hites, R. A. *Nature* **1994**, *370*, 49.

(87) McCreery, R. L. *Chemical Reviews* **2008**, *108*, 2646.

(88) Robertson, J. *Materials Science and Engineering: R: Reports* **2002**, *37*, 129.

(89) Brenner, D. W.; Shenderova, O. A.; Harrison, J. A.; Stuart, S. J.; Ni, B.; Sinnott, S. B. *Journal of Physics: Condensed Matter* **2002**, *14*, 783.

(90) Galli, G.; Martin, R. M.; Car, R.; Parrinello, M. *Physical Review Letters* **1989**, *62*, 555.

(91) Ferrari, A.; Robertson, J. *Physical review B* **2000**, *61*, 14095.

(92) Robertson, J.; O'Reilly, E. P. *Physical review B* **1987**, *35*, 2946.

(93) Wang, C. Z.; Ho, K. M. *Physical Review Letters* **1993**, *71*, 1184.

(94) Silva, S. R. P. *Properties of amorphous carbon*; IET: London, **2003**.

(95) Miyajima, Y.; Tison, Y.; Giusca, C. E.; Stolojan, V.; Watanabe, H.; Habuchi, H.; Henley, S. J.; Shannon, J. M.; Silva, S. R. P. *Carbon* **2011**, *49*, 5229.

(96) Putaud, J. P.; Van Dingenen, R.; Alastuey, A.; Bauer, H.; Birmili, W.; Cyrys, J.; Flentje, H.; Fuzzi, S.; Gehrig, R.; Hansson, H. C.; Harrison, R. M.; Herrmann, H.; Hitzenberger, R.; Hüglin, C.; Jones, A. M.; Kasper-Giebl, A.; Kiss, G.; Kousa, A.; Kuhlbusch, T. A. J.; Löschau, G.; Maenhaut, W.; Molnar, A.; Moreno, T.; Pekkanen, J.; Perrino, C.; Pitz, M.; Puxbaum, H.; Querol, X.; Rodriguez, S.; Salma, I.; Schwarz, J.; Smolik, J.; Schneider, J.; Spindler, G.; ten Brink, H.; Tursic, J.; Viana, M.; Wiedensohler, A.; Raes, F. *Atmospheric Environment* **2010**, *44*, 1308.

(97) Tanner, R. L.; Parkhurst, W. J. *Journal of the Air & Waste Management Association* **2000**, *50*, 1299.

(98) Hansen, D. A.; Edgerton, E. S.; Hartsell, B. E.; Jansen, J. J.; Kandasamy, N.; Hidy, G. M.; Blanchard, C. L. *Journal of the Air & Waste Management Association* **2003**, *53*, 1460.

(99) Jacobson, M.; Hansson, H. C.; Noone, K.; Charlson, R. *Reviews of Geophysics* **2000**, *38*, 267.

(100) Querol, X.; Alastuey, A.; Viana, M.; Moreno, T.; Reche, C.; Minguillón, M.; Ripoll, A.; Pandolfi, M.; Amato, F.; Karanasiou, A. *Atmospheric Chemistry and Physics Discussions* **2013**, *13*, 6971.

(101) Ancelet, T.; Davy, P. K.; Trompetter, W. J.; Markwitz, A.; Weatherburn, D. C. *Atmospheric Environment* **2011**, *45*, 4463.

(102) Castro, L. M.; Pio, C. A.; Harrison, R. M.; Smith, D. J. T. *Atmospheric Environment* **1999**, *33*, 2771.

(103) Ramanathan, V.; Crutzen, P. J.; Kiehl, J. T.; Rosenfeld, D. *Science* **2001**, *294*, 2119.

(104) Larson, S. M.; Cass, G. R.; Gray, H. A. *Aerosol science and technology* **1989**, *10*, 118.

(105) Park, R. J.; Jacob, D. J.; Chin, M.; Martin, R. V. *Journal of Geophysical Research* **2003**, *108*, 4355.

(106) Biehl, S.; Lüthje, H.; Bandorf, R.; Sick, J.-H. *Thin Solid Films* **2006**, *515*, 1171.

(107) Grill, A. *Diamond and Related Materials* **2003**, *12*, 166.

(108) Adenier, A.; Cabet-Deliry, E.; Chaussé, A.; Griveau, S.; Mercier, F.; Pinson, J.; Vautrin-Ul, C. *Chemistry of Materials* **2005**, *17*, 491.

(109) Dyke, C. A.; Tour, J. M. *Journal of the American Chemical Society* **2003**, *125*, 1156.

(110) Strano, M. S.; Dyke, C. A.; Usrey, M. L.; Barone, P. W.; Allen, M. J.; Shan, H.; Kittrell, C.; Hauge, R. H.; Tour, J. M.; Smalley, R. E. *Science* **2003**, *301*, 1519.

(111) March, J. *Advanced Organic Chemistry: Reactions, Mechanisms, and Structure.*; 4 ed.; John Wiley & Sons, Inc: New York, **1992**.

(112) Kikukawa, K.; Matsuda, T. *Chemistry Letters* **1977**, 159.

(113) Belanger, D.; Pinson, J. *Chemical Society Reviews* **2011**, *40*, 3995.

(114) Mahouche-Chergui, S.; Gam-Derouich, S.; Mangeney, C.; Chehimi, M. M. *Chemical Society Reviews* **2011**, *40*, 4143.

(115) Ahlberg, E.; Helgee, B.; Parker, V. D. *Acta Chemica Scandinavica Series B-Organic Chemistry and Biochemistry* **1980**, *34*, 181.

(116) Delamar, M.; Hitmi, R.; Pinson, J.; Savéant, J. M. *Journal of the American Chemical Society* **1992**, *114*, 5883.

(117) Pinson, J.; Podvorica, F. *Chemical Society Reviews* **2005**, *36*, 429.

(118) Bahr, J. L.; Tour, J. M. *Chemistry of Materials* **2001**, *13*, 3823.

(119) Fan, F. R. F.; Yang, J. P.; Cai, L. T.; Price, D. W.; Dirk, S. M.; Kosynkin, D. V.; Yao, Y. X.; Rawlett, A. M.; Tour, J. M.; Bard, A. J. *Journal of the American Chemical Society* **2002**, *124*, 5550.

(120) Stewart, M. P.; Maya, F.; Kosynkin, D. V.; Dirk, S. M.; Stapleton, J. J.; McGuiness, C. L.; Allara, D. L.; Tour, J. M. *Journal of the American Chemical Society* **2004**, *126*, 370.

(121) Barriere, F.; Downard, A. J. *J. Solid State Electrochemistry* **2008**, *12*, 1231.

(122) Ghosh, D.; Pradhan, S.; Chen, W.; Chen, S. W. *Chemistry of Materials* **2008**, *20*, 1248.

(123) Griffete, N.; Herbst, F.; Pinson, J.; Ammar, S.; Mangeney, C. *Journal of the American Chemical Society* **2011**, *133*, 1646.

(124) Laurentius, L.; Stoyanov, S. R.; Gusarov, S.; Kovalenko, A.; Du, R. B.; Lopinski, G. P.; McDermott, M. T. *ACS Nano* **2011**, *5*, 4219.

(125) Mirkhalaf, F.; Paprotny, J.; Schiffrin, D. J. *Journal of the American Chemical Society* **2006**, *128*, 7400.

(126) Hermans, A.; Seipel, A. T.; Miller, C. E.; Wightman, R. M. *Langmuir* **2006**, *22*, 1964.

(127) D'Amour, M.; Belanger, D. *Journal of Physical Chemistry B* **2003**, *107*, 4811.

(128) Adenier, A.; Bernard, M.-C.; Chehimi, M. M.; Cabet-Deliry, E.; Desbat, B.; Fagebaume, O.; Pinson, J.; Podvorica, F. *Journal of the American Chemical Society* **2001**, *123*, 4541.

(129) Wildgoose, G. G.; Wilkins, S. J.; Williams, G. R.; France, R. R.; Carnahan, D. L.; Jiang, L.; Jones, T. G. J.; Compton, R. G. *ChemPhysChem* **2005**, *6*, 352.

2. Understanding the spontaneous grafting of nPAH aryldiazonium salts at amorphous carbon surfaces: Influence of structure and stability of the aryldiazonium salt on attachment

An investigation into the spontaneous attachment of two nitro substituted polycyclic aromatic positional isomers and their monocyclic analogue at amorphous carbon surfaces is presented. We have focused on the adsorption kinetics of these polycyclic aryldiazonium salts and examined how their grafting rate and yield depends on the structure and stability of the salt. In situ grafting was monitored spectroscopically and results were complemented by electrochemical ex situ studies in order to determine surface chemisorption rates. The adsorption rates of the two positional isomers were found to be significantly different at amorphous carbon surfaces, a disparity which is attributed to a shift in reduction potential of the aryldiazonium salts.

Murphy, D. M.; Cullen, R. J.; Jayasundara, D. R.; Scanlan, E. M.; Colavita, P. E.;
Study of the spontaneous attachment of polycyclic aryldiazonium salts onto amorphous carbon substrates
RSC Advances, **2012**, *2*, 6527–6534.

2.1. Introduction

In this work we report studies on the spontaneous grafting of diazonium derivatives of nPAH compounds at amorphous carbon surfaces. More specifically, we investigated the dependance of spontaneous grafting of aryldiazonium salts at amorphous carbon surfaces on the structure of the aryldiazonium salt. The spontaneous reaction of aryldiazonium salts on surfaces is mechanistically less well understood than electrografting, however it has been shown that the specific substitutents on the aryldiazonium, the type of substrate and the solvent used for the deposition affect reaction yields and rates.[1-2] General trends have been identified showing that electron-withdrawing substituents and easily oxidizable metals tend to display faster grafting reactions. Based on these results a mechanism involving spontaneous electron transfer from metal substrates to aryldiazonium with loss of dinitrogen has been proposed, in analogy with the electrografting process. The grafting yield on carbon appears to depend, as for metals, on the relative position of donor and acceptor levels at the carbon and aryldiazonium cation, respectively, thus suggesting that the surface acts as a mild reductant.[3]

However, it has been hypothesized that multiple routes could lead to the formation of aryldiazonium layers and multilayers.[4-7] In particular, it has been proposed that the thermal decomposition of aryldiazonium salts via either homolytic or heterolytic cleavage of C—N_2^+ bonds gives rise to alternative pathways of covalent aryldiazonium attachment at surfaces, as illustrated in Scheme 2.1.

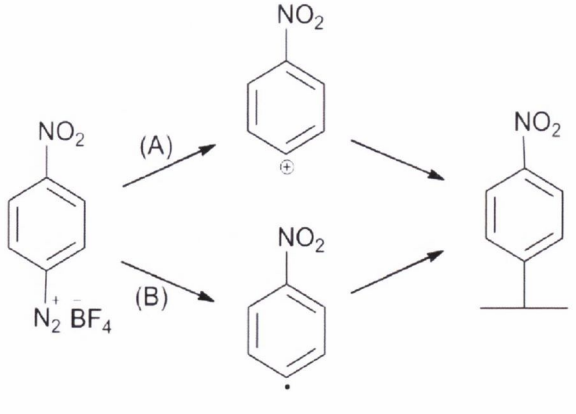

Scheme 2.1. Heterolytic (A) and homolytic (B) pathways of covalent aryldiazonium attachment at surfaces.

The spontaneous grafting process has been mainly studied using p-substituted benzenediazonium salts on metals and carbon. The most popular reagent choice is 4-nitrobenzenediazonium tetrafluoroborate (4NBD) due to the fact that it is relatively stable, it is commercially available and it possesses a nitrophenyl group that can be used to electrochemically monitor the surface coverage via its electroreduction to phenylamine. Few reports however exist on the spontaneous grafting of diazonium salts with polynuclear aromatic backbones. Polynuclear aromatic molecules, such as biphenyls, azobenzenes, stilbenes, oligo(phenylenes), or anthracene, have been the subject of intense investigation due to their extended conjugated systems. Diazonium derivatives of these molecules have been used for fundamental studies of charge transfer through thin organic films and molecular aggregates,[8-15] as well as for sensing applications in which the extended π-system and backbone rigidity are leveraged to allow fast electron transfer.[16] With few exceptions, previous work on surface modifications using polynuclear aromatic diazonium derivatives has been almost exclusively carried out using an electrochemical approach. The spontaneous grafting of diazonium derivatives of polycyclic aromatic hydrocarbons (PAH-N_2^+), on the other hand, has not yet been investigated. This is surprising, since spontaneous grafting of aryldiazonium salts has been shown to lead to greater control over surface coverage and layer ordering, two properties that are of great importance for electronic and sensing applications.[2] We are interested in nitro-substituted polycyclic aromatic hydrocarbons specifically due to their relevence in environmental systems.

In this chapter, studies on the spontaneous grafting of diazonium derivatives of nPAH compounds at carbon surfaces are presented. Two diazonium salts that share a 1-nitronaphthalene backbone were synthesised: 4-Nitronaphthalene diazonium tetrafluoroborate (4NND) and 5-nitronaphthalene diazonium tetrafluoroborate (5NND); the structure of these two compounds are shown in Scheme 2.2. A combination of electrochemical and spectroscopic techniques were used in order to investigate their covalent attachment to carbon and compare it to that of their monocyclic analogue 4NBD. The nitro group allowed the grafting process to be monitored, both *in situ* via infrared spectroscopy at the solid/liquid interface and *ex situ* via electrochemical methods. Thermal or solvolytic decomposition of aryldiazonium salts has been shown to play a role in the covalent grafting of aryldiazonium salts.[17] Therefore, the thermal stability and rate of

solvolysis of 4NND and 5NND were investigated in order to understand whether these can affect their spontaneous attachment to carbon. Marked differences in the attachment rate of these two molecules was observed and is discussed in terms of their structural differences.

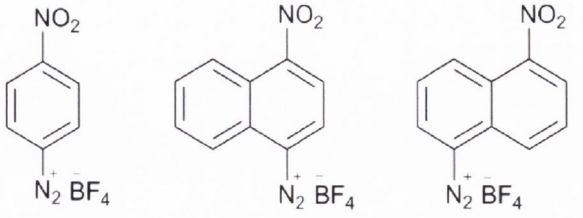

4NBD 4NND 5NND

Scheme 2.2. Structures of 4-nitrobenzene diazonium tetrafluoroborate (4NBD), 4-nitronaphthalene diazonium tetrafluoroborate (4NND) and 5-nitronaphthalene diazonium tetrafluoroborate (5NND).

2.2. Experimental

2.2.1. Chemicals and Materials

Acetonitrile (ACN, Fisher, HPLC grade), anhydrous acetonitrile (99.8%, Sigma) sulphuric acid (95-97%, Sigma) and fluoroboric acid (48% in H_2O, Sigma) were used without further purification. All other solvents were reagent grade and used as received. Ammonium chloride (≥99.5), hydroxylamine hydrochloride (>98%), potassium hydroxide (pellets, >85%), potassium nitrate (≥98%), sodium nitrite (≥99%), tetrabutylammonium perchlorate (≥99%), 1-nitronaphthalene (99%), 1,5-dinitronaphthalene (≥97%) and 4-nitrobenzene diazonium tetrafluoroborate (4NBD, 97%) were all obtained from Sigma and used as received. Sodium sulphide hydrate and ammonia hydroxide solution (35%) were sourced from Riedel-de Haen and AnalaR, respectively. Amorphous carbon substrates were prepared via DC magnetron sputtering as previously described in the literature,[18] and consisted of a 70 nm carbon layer with a 300 nm thick titanium underlayer.[19] Structural characterization of these films has previously shown that they are highly graphitic with an sp^2 content of approximately 85%.[18] Glassy carbon substrates were purchased from SPI (Glas 11), polished using 0.3 μm alumina slurry and rinsed in acid and in abundant water prior to our experiments.

2.2.2. Synthesis of compounds for modification of surfaces

Diazonium derivatives of required nitro-polycyclic aromatic hydrocarbons (nPAHs) were synthesized as they were either not available commercially at a reasonable price, or were not commercially available. In some cases, the amine derivatives of required nPAH was synthesised first, which could then be diazotized to the required molecule. Synthesis of the diazonium derivative of 4-nitronaphthalene is reported on for the first time.

4-Nitro-1-naphthylamine (4NNA).

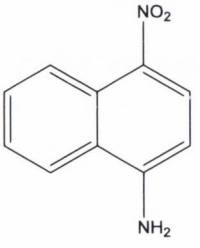

Scheme 2.3. Structure of 4-nitro-1-naphthylamine (4NNA).

4-Nitro-1-naphthylamine (4NNA) was prepared according to reported literature procedures starting from 1-nitronaphthalene.[20] 1-Nitronaphthalene (1.00 g, 0.006 mol) and hydroxylamine hydrochloride (2.50 g, 0.036 mol) were dissolved in 60 mL of ethanol in a 250 mL flask. While maintaining the temperature between 50°C and 60°C, a filtered solution of potassium hydroxide (5.00 g, 0.089 mol) dissolved in 32 mL methanol was added gradually with mechanical stirring over a period of 45 minutes. After an additional hour of vigorous stirring the solution was poured into 350 mL of cold water. The resulting precipitate was filtered by suction and washed with water. Purification by recrystallisation in ethanol and drying under high vacuum results in 4NNA as long golden orange needles (0.77 g, 77%); ν_{max} (thin film) 3401 (NH_2), 1515, 1311 (NO_2), 824 (two adjacent Ar-H), 777 (four adjacent Ar-H) cm^{-1}; ^1H NMR (400 MHz, $CDCl_3$) δ 9.01 (d, 1H, J = 8.5 Hz, Ar-H) 8.41 (d, 1H, J = 8.5 Hz, Ar-H) 7.86 (d, 1H, J = 8.5 Hz, Ar-H) 7.75 (t, 1H, J = 8.5 Hz Ar-H) 7.59 (t, 1H, J = 8.5 Hz Ar-H) 6.71 (d, 1H, J = 8.5 Hz, Ar-H) 4.96 (broad s, 2H, NH_2); ^{13}C NMR (400 MHz, $CDCl_3$) δ 149.0 (q), 137.0 (q), 130.0, 128.7, 127.7 (q), 126.0, 124.9, 121.8 (q), 121.0, 106.4; m/z (HRMS (EI^+) Calcd. for $C_{10}H_8N_2O_2$ $[M]^+$ 188.0586, Found 188.0596.

4-Nitro-naphthalene diazonium tetrafluoroborate (4NND).

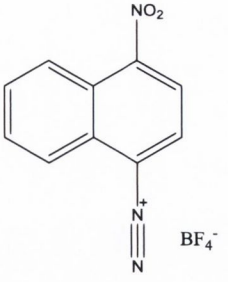

Scheme 2.4. Structure of 4-nitro-naphthalene diazonium tetrafluoroborate (4NND).

4-Nitro-naphthalene diazonium tetrafluoroborate (4NND) was prepared from 4NNA (0.20 g, 1.0 mmol) according to reported literature procedures.[21] (0.20 g, 1.0 mmol) of 4NNA was dissolved in a 48% solution of tetrafluoroboric acid (0.18 g, 2.0 mmol) was cooled to -5°C. Additional tetrafluoroboric acid (approx 5 mL) was used in order to fully dissolve the starting material. Sodium nitrite (0.14 g, 1.0 mmol) was dissolved in the minimum volume of cold water and was added dropwise with mechanical stirring over a 30 minute period, during which a precipitate formed. The precipitate was filtered by suction, washed with an ice cold ether methanol mixture (4:1) and cold ethanol, and dried under high vacuum yielding the diazonium salt, 4NND, as a dark green/yellow solid (0.19 g, 95%); ν_{max} (thin film) 2275 (N_2) 1538, 1505, 1356 (NO_2) cm^{-1}; ^1H NMR (600 MHz, d-MeOH) δ 9.34 (d, 1H, J = 8.5, Ar-H) 8.64 (d, 1H, J = 8.5, Ar-H) 8.57 (d, 1H, J = 8.5, Ar-H) 8.53 (d, 1H, J = 8.5, Ar-H) 8.29 (t, 1H, J = 8.5, Ar-H) 8.19 (t, 1H, J = 8.5, Ar-H); ^{13}C NMR (600 MHz, d-MeOH) δ 136.9, 134.0, 132.9, 129.7 (q), 125.0 (q), 125.0, 122.7, 122.0, 115.0 (q), 115.0 (q); m/z (HRMS (ESI^+), (EI^+) Calcd. for $C_{10}H_6N_3O_2^+$ $[M]^+$ 200.1730, Not found. Found 174.0741 ($C_{10}H_6N_3O_2^+ - N_2^+$).

5-Nitro-1-naphthylamine (5NNA).

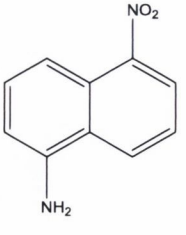

Scheme 2.5. Structure of 5-nitro-1-naphthalen-1-amine (5NNA).

5-Nitro-1-naphthalen-1-amine (5NNA) was prepared according to reported literature procedures starting from 1,5-dinitronaphthalene.[22] A solution of ammonium chloride (2.80 g, 53 mmol) in concentrated aqueous ammonia was added to a suspension of 1,5 dinitronaphthalene (1.60 g, 7.0 mmol) in water (22 mL). The solution was heated at 80 -85 °C with mechanical stirring. Sodium sulphide (1.91 g, 24 mmol) was added in three separate portions over 30 min. The mixture was heated for 4 h at 85 °C and filtered through a heated Büchner funnel. The solid was extracted twice with dichloromethane and dried over anhydrous magnesium sulphate. Excess solvent was removed and the residual material was purified by silica gel column chromatography. Elution with hexane–ethyl acetate (4 : 1), removal of solvent and drying under high vacuum results in 5NNA as a brown-red solid (0.38 g, 40%); ν_{max} (thin film) 3414, 3335, 3238, 1509, 1316, 1278, 773 cm^{-1}; ^1H NMR (400 MHz, $CDCl_3$) d 8.15 (d, 2H, J = 7.5 Hz), 7.92 (d, 1H, J = 8.7 Hz), 7.52 (m, 2H), 6.93 (d, 1H, J = 7.5 Hz), 4.29 (br s, 2H, NH_2); ^{13}C NMR (400 MHz, $CDCl_3$) d 147.5 (q), 142.7 (q), 130.0, 127.0, 126.1 (q), 124.8 (q), 123.6, 122.8, 113.5, 111.3; m/z HRMS (EI^+) Calcd. for $C_{10}H_8N_2O_2$ $[M]^+$ 188.0586. Found [M]+H 189.0662.

5-Nitro-naphthalene diazonium tetrafluoroborate (5NND).

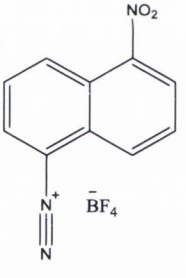

Scheme 2.6. Structure of 5-nitro-naphthalene diazonium tetrafluoroborate (5NND).

5-Nitro-naphthalene diazonium tetrafluoroborate (5NND) was prepared from 5NNA (0.19 g, 1.0 mmol) according to reported literature procedures.[21] Additional tetrafluoroboric acid (approx. 5 mL) and water (approx. 5 mL) was used in order to fully dissolve the starting material. The precipitate obtained was filtered by suction, washed with an ice cold ether–methanol mixture (4 : 1) and cold ethanol, and dried under high vacuum yielding the diazonium salt, 5NND, as a brown solid (0.13 g, 75%); ν_{max} (thin film) 2276, 1531, 1348, 800, 755 cm^{-1}; ^1H NMR (600 MHz, d-MeOH) d 9.39 (d, 1H, J = 8.5 Hz), 9.29 (d, 1H, J = 8.0 Hz), 8.81 (d, 1H, J = 8.5 Hz), 8.70 (d, 1H, J = 8.0 Hz), 8.27 (m, 2H); ^{13}C NMR (600

MHz, d-MeOH) d 148.2 (q), 138.4, 138.3, 131.8, 129.1, 128.6 (q), 127.7, 127.6, 126.6 (q), 112.8 (q).

2.2.3. Sample characterization

Infrared reflection absorption spectroscopy (IRRAS) was carried out on a Bruker Tensor 27 Fourier transform infrared (FTIR) spectrometer, equipped with a mercury-cadmium-telluride (MCT) detector, using a VeeMaxII variable angle specular reflectance accessory with wire grid polarizer. All IRRAS measurements were obtained using p-polarized light at an 80° angle of incidence from the surface normal. 256 scans with a resolution of 4 cm^{-1} were collected for each sample and a bare a-C carbon substrate was used as a background. *In situ* monitoring of the spontaneous grafting of 4NBD, 4NND and 5NND onto carbon substrates was carried out using a custom-built ATR cell, a schematic of which is given in Figure 2.1.[18] The internal reflection element was a trapezoid made from 1245 μm thick, double sided polished, undoped silicon wafers (Virginia Semiconductors, resistivity > 100 Ω-cm) with polished 45° edges. The trapezoid was sputter coated on its longest face with amorphous carbon films and a PDMS gasket was used to seal the carbon side of the trapezoid forming a liquid cell. Background spectra were collected via injection of deionized water; afterwards, a degassed solution of the aryldiazonium in deionized water was injected into the cell. Spectra were collected at regular time intervals after injection; 100 scans at 4 cm^{-1} resolution were averaged for each time point over the course of 3 h. Upon completion of the grafting experiment, a 0.2 M aqueous KNO_3 solution was injected into the cell; the nitrate peak at 1338 cm^{-1} from this spectrum was used to normalize all spectra in order to correct for differences in optical pathlength (l).

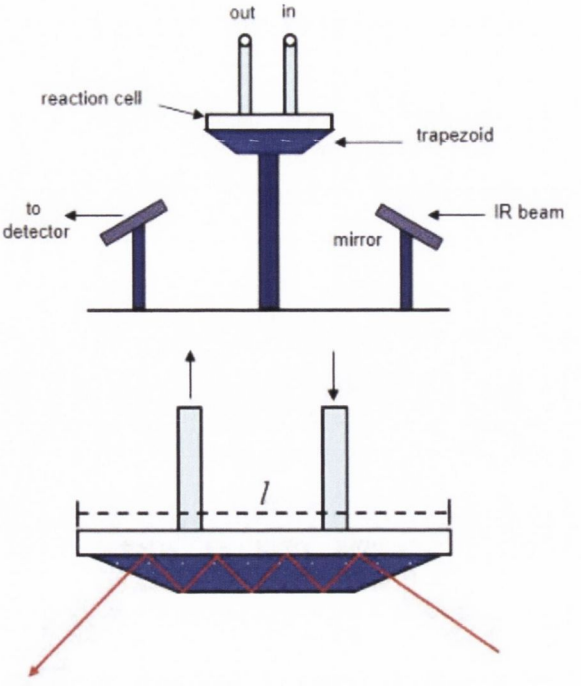

Figure 2.1. Schematic of custom built ATR cell for in situ monitoring with pathlength (l) indicated.

In order to compare grafting rates for the different compounds an internal standard method was used to normalize for differences in cross section among 4NBD, 4NND and 5NND.[23] This method was used to normalize *in situ* monitoring data to reflect the surface density of absorbed molecules at the carbon surface as a function of time. Briefly, potassium ferriccyanide ($K_3[FeCN_6]$) was chosen as the internal standard as it displays a single strong absorbance at 2115 cm^{-1} that does not interfere with infrared peaks of the three compounds. The IR absorption of $K_3[FeCN_6]$ is shown in Figure 2.2.

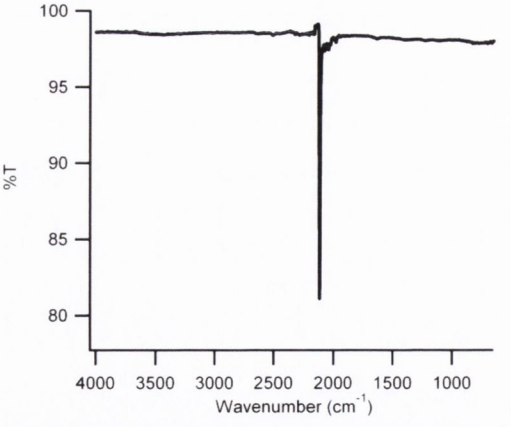

Figure 2.2. IR spectrum of $K_3[FeCN_6]$.

A known percentage (per weight) of internal standard and compound were combined and their absorption spectra measured using ATR spectroscopy. An example of a spectrum obtained for 4NND is shown in Figure 2.3., with the internal standard (IS) peak labelled. Experiments were carried out three times and the average ratio of the internal standard to symmetric N—O stretching peaks were used to normalize for differences in cross section among 4NBD, 4NND and 5NND.

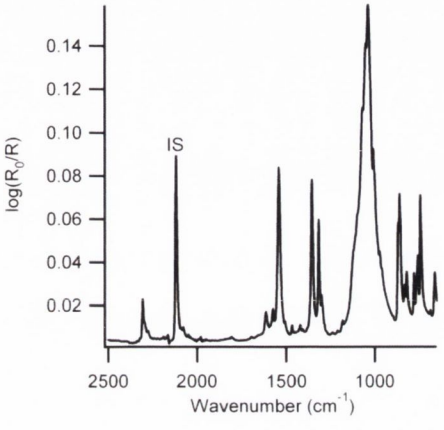

Figure 2.3. IR spectrum of 4NND.

X-ray photoelectron spectroscopy (XPS) measurements of carbon substrates were carried out in an Omicron system with a multichannel array detector, at 1×10^{-10} mbar base pressure. XP spectra were recorded at room temperature at 45° take-off angle with an analyzer resolution of 0.5 eV using a monochromatized Al K_α source (1486.6 eV). Peaks were fitted to Voigt functions, using commercial software (Igor Pro 6.04). Thermogravimetric analysis (TGA) was performed on a Pyris 1 TGA (Perkin Elmer). Measurements were recorded under N_2 atmosphere in the range 0-900 °C at 10 °C/min. Differential Scanning Calorimetry (DSC) was carried out on a Diamond DSC (Perkin Elmer). These measurements were collected in the range 0-200 °C at 5 °C/min and in the range 90-180 °C at 0.5 °C/min. UV-Vis absorption was carried out on a Lambda35 (Perkin Elmer) spectrometer equipped with a thermostated cell; spectra were collected at 1 nm resolution in the range 220-470 nm at 37 °C, at regular time intervals.

Aryldiazonium grafting on a-C substrates was carried out by immersing the samples in aqueous solutions of 4NND and 5NND for varying lengths of time. After grafting, the substrates were washed and sonicated in water and dried under argon prior to

electrochemical analysis. Cyclic voltammetry was carried out on a CHI660C potentiostat using Pt wire and Ag/AgCl, KCL (3M), as counter and reference electrodes, respectively. Experiments were carried out in a previously described Teflon cell with an electrode area of 0.067 cm^2.[24] Electrochemical analysis was performed at room temperature in argon purged 0.1 M H_2SO_4 solutions. Electrochemistry of aryldiazonium salts in non-aqueous solutions was carried out in anhydrous acetonitrile using 0.1 M tetrabutylammonium perchlorate (NBu_4ClO_4) as supporting electrolyte; potentials were measured against a Pt pseudo-reference electrode and corrected using Ferrocene as a standard.[25]

2.2.4. Characterization techniques

A number of different infrared spectroscopy techniques were used during the completion of this work, including attenuated total reflection Fourier transform infrared spectroscopy (ATR-FTIR) and infrared reflection adsorption spectroscopy (IRRAS) in order to determine functional groups on functionalised surfaces. These infrared spectroscopy techniques differ slightly in instrumentation setup and/or method of data collection and have individual benefits; ATR-FTIR measurements require no sample preparation and the Fourier transform ensures a low signal/noise ratio whereas IRRAS, which can be used for both solid and liquid analysis, allows reactions occurring *in situ* on surfaces to be monitored as they occur.

ATR is a technique in which the changes that occur in a totally internally reflected infrared beam are measured when a sample is in optical contact crystal with a high index of refraction, which is termed the ATR crystal. During the course of this work, ATR-FTIR was utilized to attain infrared spectra of bulk solids. The principle of ATR-FTIR measurements is illustrated in Figure 2.4.

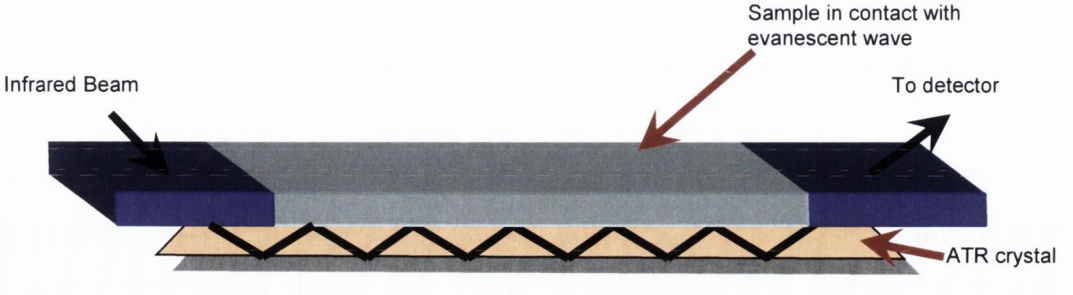

Figure 2.4. Principle of ATR-FTIR measurement.

IRRAS is used to measure infrared spectra of absorbed matter and thin layers on surfaces. The theoretical principle behind this technique is that incident infrared light can be resolved into p- and s- polarised components in which the electric vector oscillation is parallel and perpendicular to the plane of incidence, respectively. A depiction of the p- and s- polarised components of light is given in Figure 2.5.

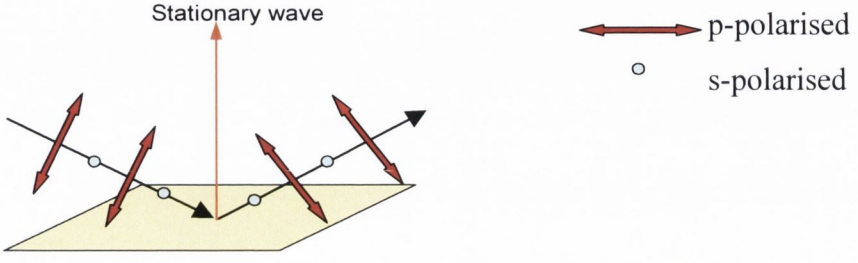

Figure 2.5. Depiction of p- and s- polarised components of light.

The intensity of an IR spectrum is defined by the interaction between the oscillating dipoles of the samples molecules and the electric field. According to Gauss' Law, the electric field on the surface of a conductor is always perpendicular to the surface, while at any point within the conductor, the electric field is always zero. This law can also be applied to metals. Therefore, with parallel external electric field (s-polarised light) the electric fields inside and on the surface of the metal cancel as shown in Figure 2.6.(a). If the external electric field is perpendicular as shown in Figure 2.6.(b), the induced dipole moment has an electric field which is parallel to the external electric field resulting in a net perpendicular electric field strength. This is known as the surface selection rule for metal surfaces.

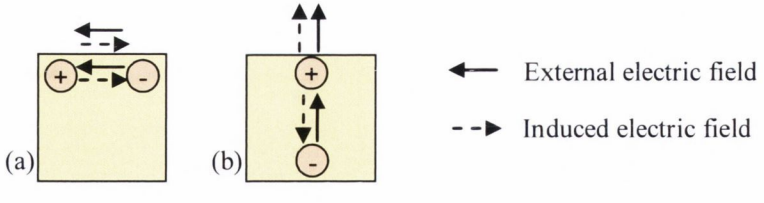

Figure 2.6. Electric fields at metal interface for (a) parallel and (b) perpendicular external electric field.

Consequently, the optimum condition for collection of signals as a result of absorbed surface species on metal surfaces and highly doped semiconductive surfaces is through use of p-polarised light at high angles of incidence. In this work, a titanium underlayer was utilized to enhance the surface selection rules. IRRAS can be used to determine the

presence of functional groups on surfaces which that have transition dipoles with a component perpendicular to the surface and it can also be used to monitor the disappearance of such functional groups over time during the course of a reaction, which was the rationale for the use of this technique in the work presented.

2.3. Results and Discussion

2.3.1. Grafting of 4NND and 5NND at carbon surfaces

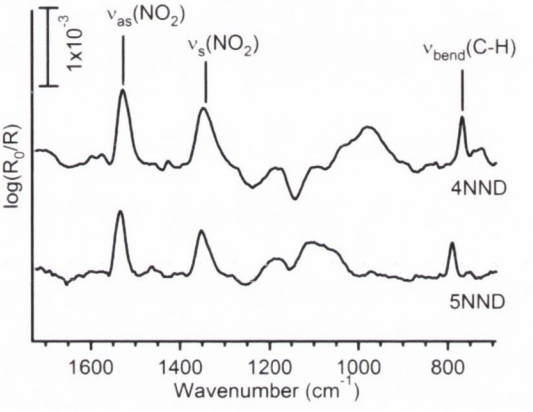

Figure 2.7. IRRAS spectra of a-C substrates following immersion in 1×10^{-3} M 4NND and 5NND solutions for 1 h.

The assembly of diazonium salt derivatives of nitronaphthalene was first investigated *ex situ*. Carbon samples were immersed in 4NND and 5NND solutions, following which they were thoroughly rinsed and dried prior to characterization via surface spectroscopy and electrochemical techniques. Figure 2.7. shows the IRRAS spectra of amorphous carbons (a-C) after modification in 1×10^{-3} M acetonitrile solutions of 4NND and 5NND for 1 h. The spectra show peaks at 1533 cm^{-1} and 1352 cm^{-1} that are assigned to the asymmetric and symmetric N—O stretching modes ($\nu_{as}(NO_2)$ and $\nu_s(NO_2)$), respectively, of nitro groups.[26-27] The peaks at 767 and 790 cm^{-1} in the 4NND and 5NND traces, respectively, can be attributed to the C—H out of plane bending of the naphthalene backbone.[26-27] Measurement of the bulk unattached diazonium salt via ATR results in the same distingushing peaks as can be seen in Figure 2.8., however some peaks may be slightly shifted. A table with peak assignments for the bulk compound is presented in Table 2.1. The IRRAS spectroscopic signature of 4NND- and 5NND-modified surfaces shown in Figure 2.7. is in good agreement with that obtained from other nitroaromatic diazonium salts, such as 4-

nitrobenezenediazonium tetrafluoroborate, and suggests that surface immobilization takes place spontaneously, as in the case of monocyclic aryldiazonium salts.[18,28]

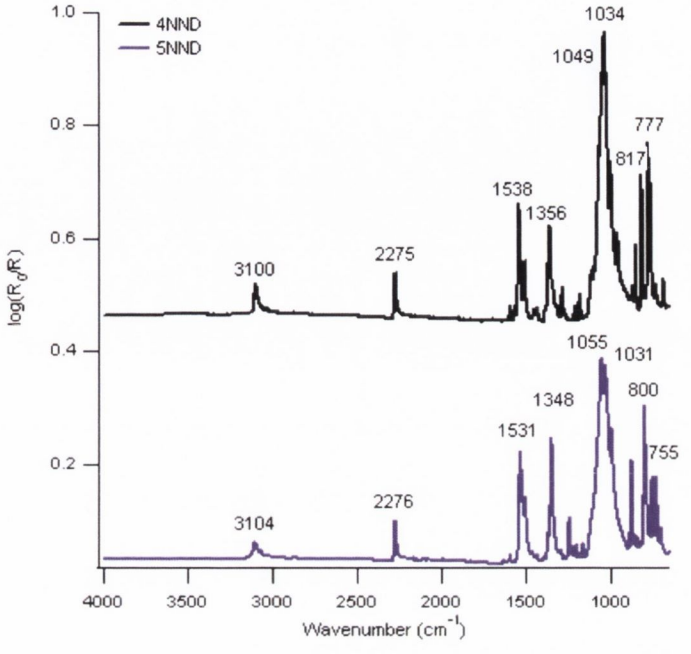

Figure 2.8. IR spectra of the bulk unattached diazonium salt measured via ATR.

Table 2.1. Assignment table for bulk diazonium salts.[27]

Literature (cm^{-1})	4NND (cm^{-1})	5NND (cm^{-1})	Assignment
3105-3000	3100	3104	Aromatic =C-H stretching vib
2300-2130	2275	2276	N_2^+ stretch
1570-1485	1538	1531	Asym NO_2 stretch, aromatic
1370-1320	1356	1348	Sym NO_2 stretch, aromatic
1180-865	1136-885	1141-904	CN stretch
1160-760	1049, 1034	1055, 1031	Asym B-F stretch, Shoulder 1060 cm^{-1}
810-775	777	800	C-H, out of plane bending, naphthalene
850-800	817		Naphthalenes, 2 adj H atoms
815-775, 760-730		800, 755	Naphthalenes, 3 adj H atoms

It is also important to note that no peaks could be detected in the 2300-2130 cm^{-1} region, where $-N{\equiv}N^+$ stretching modes would be expected.[27] This is illustrated in Figure 2.9., which shows examples of an *ex situ* IRRAS spectra and an *in situ* ATR-FTIR spectra. The large peak (negative or positive) at 2350 cm^{-1} in these spectra is due to atmospheric carbon dioxide.

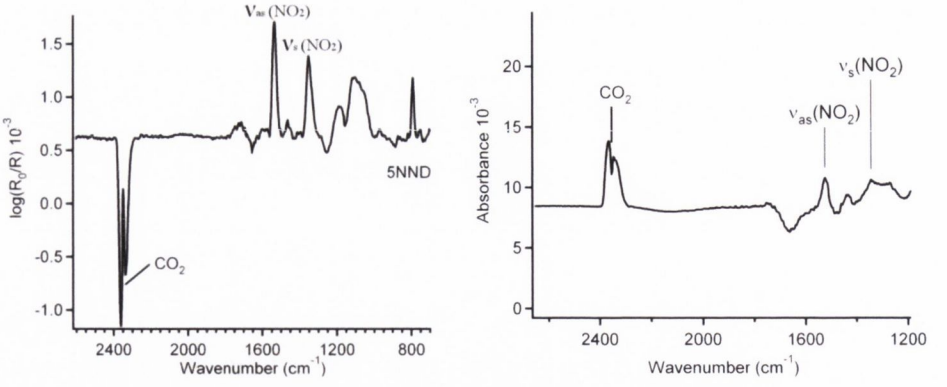

Figure 2.9. (a) IRRAS spectra of a-C substrates following immersion in 1×10^{-3} M 5NND aqueous solution for 1 h and (b) ATR-FTIR spectra collected at 5.3 h following injection of a 1×10^{-4} M 4NND aqueous solution.

Grafting of nitronaphthalene diazonium salts on carbon was also investigated via electrochemistry using amorphous carbon electrodes. Figure 2.10. shows the cyclic voltammetric (CV) response of 4NND and 5NND modified a-C electrodes in 0.1 M H_2SO_4 aqueous solutions. The modified a-C electrodes in Figure 2.10. were prepared via spontaneous modification in 1×10^{-4} M aqueous solutions of the diazonium salts for 10 min. The CV's show an irreversible cathodic peak at -0.87 V and -0.59 V (vs. Ag/AgCl, KCL (3M)) for 4NND and 5NND, respectively, that we attribute to the electroreduction of nitrophenyl groups.[29] Subsequent potential sweeps do not display these peaks, which is consistent with a near complete reduction of surface-bound $ArNO_2$ groups. The difference of ~0.28 V in cathodic peak position for 4NND and 5NND suggests that the organic layers resulting from spontaneous grafting of these two molecules over 10 min are different in structure and/or thickness. The cathodic peak for 4NND has a larger integrated area than that observed for 5NND. This result also suggests that a higher surface density of reducible nitroaryl groups is present at the carbon surface in the case of 4NND, which would be consistent with a thicker organic film. Both IRRAS and electrochemical results, however, indicate that both nitronaphthalene diazonium salts can be spontaneously grafted from solution onto amorphous carbon films.

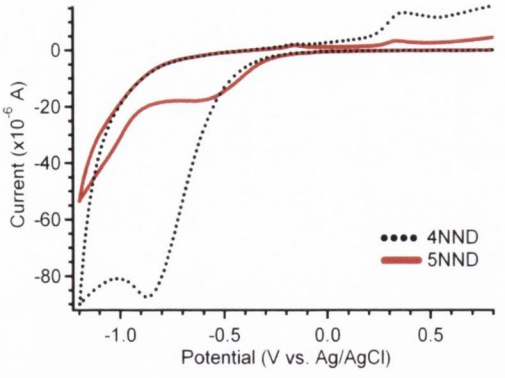

Figure 2.10. Cyclic voltammograms of 4NND and 5NND-modified a-C electrodes obtained in 0.1 M H_2SO_4 at 0.2 V s^{-1}; the substrates were modified via immersion in 1×10^{-4} M aqueous solutions of 4NND and 5NND for 10 min.

2.3.2. *In situ* adsorption rate studies at carbon/solution interfaces

4NND and 5NND are positional isomers: in 4NND the $-N_2^+$ group is positioned on the same aromatic ring as the electron withdrawing $-NO_2$ group, whereas in 5NND the $-N_2^+$ is positioned in the neighbouring aromatic ring of the nitronaphthalene backbone. This is illustrated in Scheme 2.2. In order to investigate whether this difference affected the spontaneous attachment of these molecules onto carbon surfaces we carried out *in situ* and *ex situ* studies of their reactions at the carbon surface.

The *in situ* monitoring of the spontaneous grafting of 4NND and 5NND onto a-C substrates was carried out via attenuated total internal reflection Fourier Transform infrared spectroscopy (ATR-FTIR) techniques as previously reported.[18] Carbon coated trapezoids were used as ATR optical elements in a liquid cell containing water; at time zero, a 1×10^{-4} M aqueous solution of the diazonium salt was introduced into the cell and left to react at the carbon surface. Figure 2.11.(a) shows an example of ATR-FTIR spectra in the $\nu(NO_2)$ spectral region measured at different times after the injection of the 4NND solutions into the liquid cell. Surface adsorption was monitored by plotting the net absorbance at the ~1340 cm^{-1} peak maximum associated to the $\nu_s(NO_2)$ mode; this peak was chosen over the asymmetric stretching because it was least affected by water vapour peaks across all of the ATR-FTIR datasets.

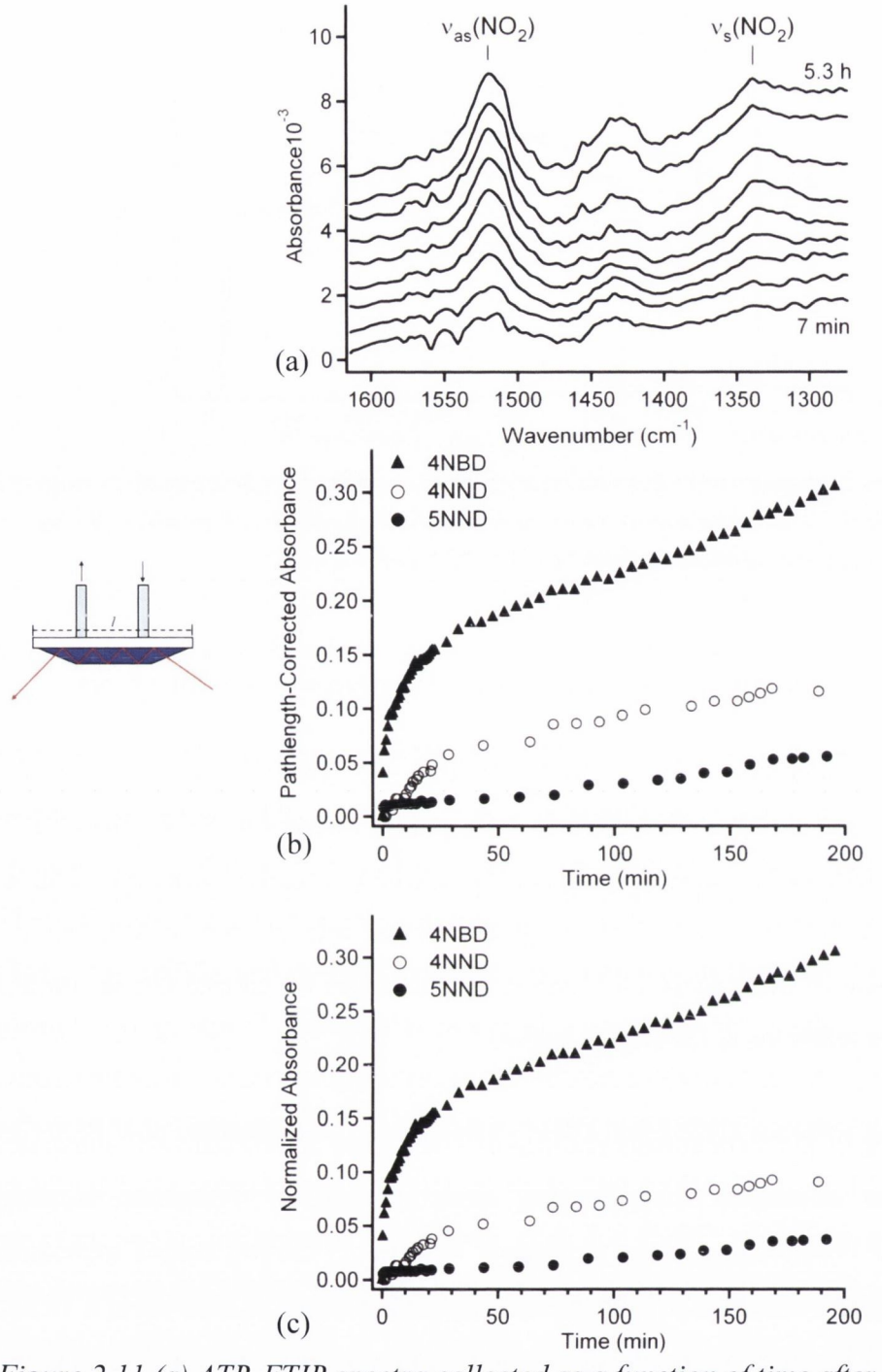

Figure 2.11.(a) ATR-FTIR spectra collected as a function of time after injection of a 1×10^{-4} M 4NND aqueous solution into the liquid cell; spectra are offset for the sake of clarity. (b) Plot of the pathlength-corrected net absorbance of $\nu_s(NO_2)$ as a function of deposition time obtained for 4NBD, 4NND and 5NND. (c) Plot of the $\nu_s(NO_2)$ net absorbance normalized by pathlength and absorption cross-section (Normalized Net Absorbance), as a function of deposition time.

The $\nu_s(NO_2)$ net absorbance was corrected for any differences in pathlength by normalizing spectra against the same peak obtained from a standard KNO_3 solution, thus obtaining curves of corrected net absorbance as a function of time. Figure 2.11.(b) shows adsorption curves obtained via this methodology for 4NND and 5NND; curves obtained for the

monocyclic aromatic analogue, 4NBD, previously investigated in our group[18] are also reported for comparison purposes. A schematic of ATR flow cell is also shown in Figure 2.11.(b) for clarity, with pathlength, (l),

In order to obtain curves that reflect the density of adsorbed molecules at the carbon surface as a function of time, we further normalized the curves in Figure 2.11. (b) by the relative absorption cross sections of the $\nu_s(NO_2)$ mode for the three different molecules, as described in Section 2.2.3. Figure 2.11.(c) shows the results of normalization by both pathlength and absorption cross section; these curves display the changes in surface density of nitroaryl groups as a function of deposition time obtained during adsorption of 4NBD, 4NND and 5NND at the same carbon surface.

The deposition curves shown in Figure 2.11.(c) indicate that the rate of adsorption of nitroaryl groups follows the order 4NBD>4NND>5NND. In all three cases two adsorption regimes can be observed: a first fast adsorption process that takes place within the first 20 min followed by a slower adsorption process at longer times, in agreement with previous reports on 4NBD by Lehr and Downard.[7] A first notable difference that emerges from Figure 2.11.(c) is the difference between the adsorption rates of 4NBD and 4NND. These two molecules share a p-nitrosubstituted benzenediazonium backbone, but differ in size due to the presence of an additional fused aromatic ring in 4NND. After the first 20 min of deposition, the average surface density of arylnitro groups at 4NBD modified carbon surfaces is equal to 3.4 times the density observed via modification with 4NND. This value is in excellent agreement with previously observed surface density ratios of 2.7 obtained by Allongue *et al.* from electrografting experiments on the same diazonium salts, which were attributed to differences in diazonium cation size.[30] The similar surface density ratios obtained via electrografting and spontaneous adsorption suggest that differences in adsorption rate between 4NBD and 4NND in Figure 2.11.(c) arise predominantly from differences in molecular cross section.

A second significant difference is that observed between the two positional isomers, 4NND and 5NND. After the first 20 min of deposition, the average surface density of nitroaryl groups at 4NND modified carbon surfaces is equal to 3.1 times the density

observed via modification with 5NND indicating that 4NND accumulates in significantly higher yields at a-C surfaces. 4NND and 5NND do not differ by their geometric molecular cross sections; therefore, the difference in surface density shown in Figure 2.11.(c) must arise from the difference in position of the $-N_2^+$ relative to the $-NO_2$ group.

2.3.3. *Ex situ* studies of grafting rates at carbon surfaces

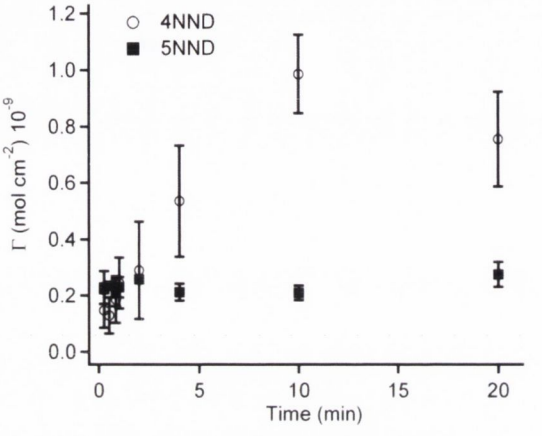

Figure 2.12. Surface coverage of nitrophenyl groups (Γ) on a-C substrates as a function of deposition time in 1×10^{-4} M 4NND (○) and 5NND (■) solutions.

Ex situ data on surface grafting of 4NND and 5NND at a-C substrates was obtained via electrochemical methods. Surface coverage (Γ) of the electroactive nitroaryl group was determined via integration of reduction peaks after progressively longer immersion times.[18,30] Figure 2.12. shows Γ as a function of time for 1×10^{-4} M 4NND and 5NND on a-C substrates. The magnitude of Γ obtained from our experiments is in good agreement with literature reports of 15×10^{-10} mol cm^{-2} for the saturation coverage of 4NND at a flat surface.[30] Results from *ex situ* characterisation are in agreement with those obtained via *in situ* spectroscopic monitoring at a-C surfaces: 4NND modified substrates show increased surface density when compared to 5NND samples after the same deposition time. The difference in Γ values for 4NND and 5NND is consistent with differences in nitroaryl electroreduction potentials observed in Figure 2.6.(~0.28 V difference, see above), since a thicker 4NND layer can result in increased impedance to electron transfer at the organic/solution interface when compared to 5NND chemisorbed films.

Differences in the adsorption of the two positional isomers observed *in situ*, ultimately lead

to different surface coverage in the chemisorbed organic layer, as shown by *ex situ* techniques. Since the geometric molecular cross section of 4NND and 5NND is similar, differences observed in adsorption rates must be attributed to differences in the position of $-N_2^+$ relative to the $-NO_2$ group. A change in substitution position can have two important effects on these molecules: substitution position at C4 compared to C5 should lead to (a) higher diazonium salt stability towards dediazoniation and/or (b) changes in electron density, in particular at the diazo-substituted carbon. In order to understand whether one or both of these effects plays a role in determining the adsorption rate at the carbon/solution interface we carried out an investigation on the stability of 4NND and 5NND towards dediazoniation.

2.3.4. Dediazoniation of 4NND and 5NND salts

If dediazoniation of aryldiazonium cations in solution were an important factor in determining adsorption rates at the carbon surface, a significant difference in the dediazoniation rates in solution should also be observed. Based on the different positioning of the stabilizing nitro group with respect to the diazo group in 4NND and 5NND it is reasonable to expect differences in stability and/or rate of dediazoniation. In order to test this hypothesis we investigated the thermal decomposition of 4NND and 5NND in the solid state and in solution.

The stability towards thermal decomposition of 4NND and 5NND was first investigated in the solid state using TGA (thermogravimetric analysis) and DSC (differential scanning calorimetry). The weight percentage loss of both 4NND and 5NND upon heating under inert atmosphere was measured using TGA for both compounds as illustrated in Figure 2.13. These results display an initial sharp weight loss between 120 °C and 160 °C for both compounds and then a gradual decline in weight as the temperature increased to 900 °C. Extrapolated onset temperatures of thermal decomposition were found to be (145 ± 2) °C and (126 ± 1) °C (90% Confidence Interval (C.I.)) for 4NND and 5NND, respectively. DSC data was used to calculate a reaction enthalpy $\Delta_R H$ associated with this decomposition process of -132.1 kJ/mol and -133.3 kJ/mol for 4NND and 5NND, respectively. Bräse *et al.*[31] have proposed that the first step in the thermal decomposition of aryldiazonium

tetrafluoroborate salts in the solid phase involves dediazoniation, in a process similar to a Schiemann reaction.[32] Therefore, our results indicate that 5NND is more thermally labile than 4NND, as would be expected based on the stabilizing effect of a nitro group closer to the diazo group in the case of 4NND.[33]

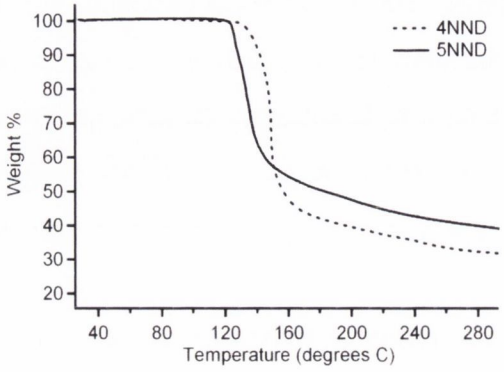

Figure 2.13. Thermogravimetic analysis of 4NND and 5NND under N_2 in the range 0-900 °C at 10 °C/min.

In order to determine if any significant differences in dediazoniation rates were observed in solution, we carried out hydrolysis experiments using 4NND and 5NND. Aryldiazonium compounds hydrolise via dediazoniation followed by formation of phenolic derivatives;[34-36] this process can be followed via UV-Vis by monitoring the disappearance of the absorption peak at ~260 nm, as previously reported.[33,35,37] The comparative UV absorption spectra of 4NBD, 4NND and 5NND are given in Figure 2.14.

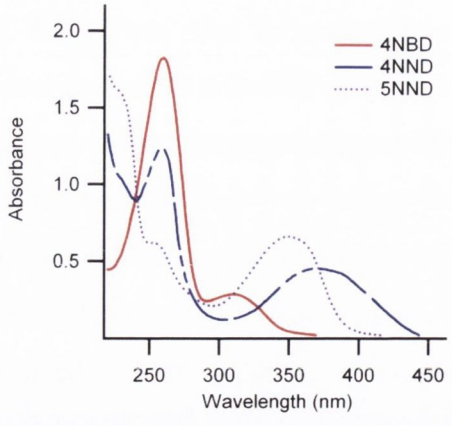

Figure 2.14. Comparative UV spectra of 4NBD, 4NND and 5NND.

Aqueous solutions (1×10^{-4} M) of 4NBD, 4NND and 5NND were prepared and their UV-Vis absorption spectra obained which are displayed in Figure 2.14. Similar to 4NBD, its monocyclic analogue, 4NND has a maximum at ~260 nm, characteristic of the nitrobenzene chromophore. This absorption is assigned to an intramolecular transfer band from the benzene ring towards the NO_2 group. However the second smaller maxima observed at ~320 nm in 4NBD is shifted to 370 nm in 4NND due to the additional aromatic ring. This peak is shifted to lower wavenumber of ~350 nm for 5NND.

Figure 2.15.(a) and (b) show the evolution of the absorption spectra of 1×10^{-4} M 4NND and 5NND solutions, respectively, as a function of time at 37 °C over 7 h: as hydrolysis of the aryldiazonium cation progresses, the absorption peaks at 259 nm (Figure 2.15.(a)) and 232 nm (Figure 2.15.(b)) decrease. Observed first-order hydrolysis rate constants were obtained by fitting the absorbance vs. time according to Equation 2.1. (shown in the insets in Figure 2.15.).[33,38-39]

$$\ln\left(\frac{A_t - A_\infty}{A_0 - A_\infty}\right) = -k_{obs}t \qquad \text{(Eqn 2.1.)}$$

where A_t, A_0 and A_∞ are the absorbances at the peak maximum at time t, at time 0 and after 48 h.

The rate constants, k_{obs}, thus calculated were found to be $(1.5 \pm 0.9)\times10^{-5}$ s^{-1} and $(6 \pm 3)\times10^{-6}$ s^{-1} for 4NND and 5NND, respectively. These values compare well to previously measured hydrolysis rate constants,[33,35] and suggest that both 4NND and 5NND are stable in water over the course of typical surface modification reactions; their two hydrolysis constants, however, cannot be distinguished statistically to a significance level better than 25%.

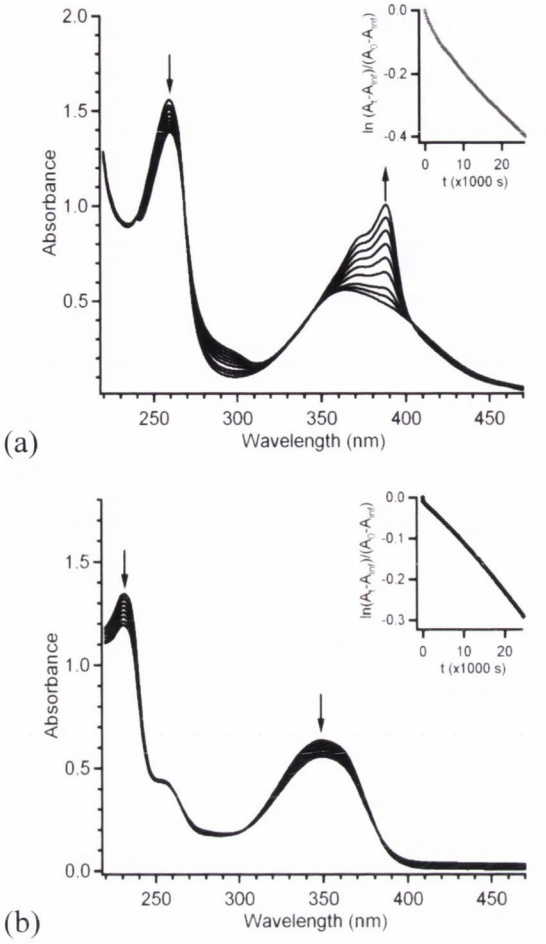

Figure 2.15. UV-Vis spectra of 1×10^{-4} M solutions of (a) 4NND and (b) 5NND) during hydrolysis at 37 °C over a period of 7 h. The insets show the corresponding first-order kinetic plots obtained from the UV-Vis data (see Equation 2.1.).

2.3.5. XPS Characterization of 4NND and 5NND adlayers

Previous work from our group has shown that surface coverage determined via *in situ* methods contains contributions from both physisorbed and chemisorbed molecules, as only a certain portion of molecules at the surface have actually undergone dediaziation.[40] XPS characterization of 4NND and 5NND adlayers was carried out to investigate if this were also the case for these nPAHs. XPS spectra are obtained by simultaneously measuring the kinetic energy and number of electrons that escape from the surface of the material being analyzed while irradiating with an X-ray excitation source. Following irradiation, X-ray photons hit and transfer their energy to core-level electrons whose emitted kinetic energies are dependent on the incident X-ray and binding energies of the atomic orbital from where

they came. Analysis of the energy and intensity of the emitted photoelectrons reveals the identity and concentrations of the elements present.

The N 1s regions of the spectra were investigated in order to determine the proportion of molecules that undergo dediazoniation, using the following methodology.[40] Characterization of modified surfaces was taken at early reaction times, after a gentle water rinse; this method has been shown to leave most of the adsorbed layer intact, thus allowing for the determination of chemical composition of adsorbed aryldiazonium layers.[40]

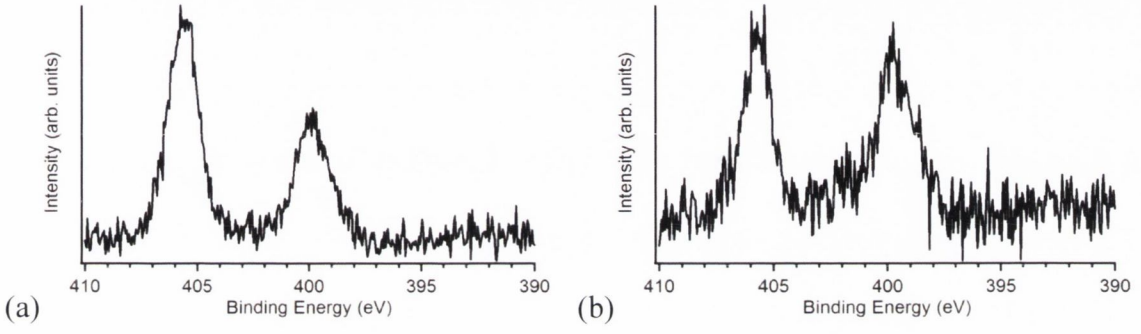

Figure 2.16. XP spectra in the N 1s region of (a) 4NND and (b) 5NND adlayers at a-C surfaces.

Figure 2.16.(a) and (b) show the N 1s region of the XP spectra of 4NND and 5NND adlayers, respectively, at a-C surfaces. The samples were prepared via immersion in 0.1 mM solutions of the aryldiazonium salt for 5 min, followed by gentle rinsing in water. XP spectra display two peaks with maxima centered around 406 and 400 eV; the peak at 406 eV is assigned to $-NO_2$ groups, whereas the broader peak at 400 eV can be attributed to the presence of –N=N– moieties. The expected A_{400} : A_{406} peak area ratio for molecules that adsorb with a diazo-group intact is 2 : 1; therefore, the ratio ($A_{400}/2$) : A_{406} provides an estimate of the proportion of molecules that have not undergone nitrogen elimination (dediazoniation) upon adsorption.

A fit of the peaks at 406 and 400 eV in Figure 2.16.(a) and (b) yielded estimates of 33% and 71% for the proportion of 4NND and 5NND molecules, respectively, that have not undergone dediazoniation upon adsorption. This indicates that for 4NND adlayers, at early reaction times, the vast majority of molecules eliminate nitrogen and therefore the adlayer

consists of mainly chemisorbed molecules with a small proportion of weakly sorbed molecules (33%). In the case of 5NND we find the opposite is true, with approximately 71% of molecules not having undergone dediazoniation upon adsorption, and these molecules are therefore expected to remain weakly physisorbed at the carbon surface.

The XPS characterization of 4NND and 5NND adlayers at a-C surfaces reaffirms our observations from previous sections. The CV's shown in Section 2.3.1., (Figure 2.10.) indicate that organic layers resulting from spontaneous grafting of the positional isomers were different in structure. *In situ* and *ex situ* experiments of the spontaneous adsorption of 4NND and 5NND showed very different adsorption regimes for the two molecules. The XPS analysis has confirmed that spontaneous grafting of 4NND and 5NND aryldiazonium salts lead to the formation of mixed physi/chemisorbed layers and provides further understanding for the observed differences in the adsorption behaviours of these molecules. The XPS result suggests that in the case of 4NND chemisorption is a faster process than for 5NND at the same a-C surface.

2.3.6. Electrochemical analysis of electron density differences

Our results indicate that, despite showing differences in thermal stability in the solid phase, 4NND and 5NND are equally stable towards dediazoniation under typical conditions used for spontaneous adsorption at surfaces. We have shown in Section 2.3.4. that the remarkable difference in adsorption rate observed in Figure 2.11.(c) and Figure 2.12. therefore cannot be attributed to dediazoniation reactions that take place in solution but must arise from differences in the interaction of 4NND and 5NND at the carbon surface due to differences in electron density between the two positional isomers.

Therefore, electrochemical measurements were carried out to find the reduction potential of the aryldiazonium functional group. The peak potential at which the reduction peak is observed shifts with the position of acceptor levels in solution. A cathodic sweep in 7×10^{-4} M solutions of 4NND and 5NND in anhydrous acetonitrile containing also 0.1 M tetrabutylammonium perchlorate as supporting electrolyte shows an irreversible cathodic wave with E_p at 0.05 ± 0.01 V and -0.20 ± 0.02 V (vs. SCE, C.I. = 90%) for 4NND and

5NND, respectively as shown in Figure 2.17. The more negative potential obtained for 5NND indicates that its reduction is more difficult to achieve than that of its positional isomer 4NND.

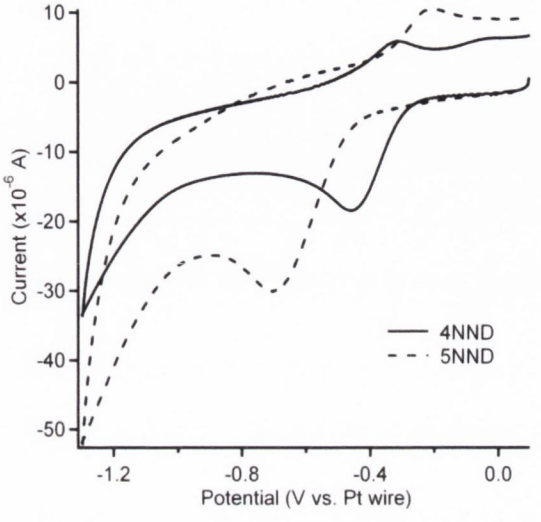

Figure 2.17. Cyclic voltammetry at 0.2 V s^{-1}, showing reduction peaks of diazonium ($-N_2^+$) groups of 4NND and 5NND in anhydrous acetonitrile solution.

2.4. Conclusions

The spontaneous grafting of fused aromatic nitro compounds onto amorphous carbon surfaces was investigated using a combination of spectroscopic and electrochemical techniques. The *in situ* grafting of 4NND and 5NND onto amorphous carbon surfaces was monitored and compared with that of their monocyclic analogue 4NBD. Differences in adsorption rate and final surface coverage between 4NBD and 4NND could be explained based on geometric molecular cross-sections, however, the remarkable difference in adsorption and chemisorption rates between 4NND and 5NND could not be explained via steric arguments.

Solvolysis of 4NND and 5NND was found to occur over similar timescales under experimental conditions used for spontaneous attachment of these two aryldiazonium salts, therefore, differences in coverage cannot be ascribed to faster degradation in solution of one of the positional isomers. Adsorption rates, on the other hand, appear to correlate very

well with the reduction potential of the aryldiazonium cation, which was found to be more positive for 4NND compared to 5NND. These results are in agreement with reactivity trends observed for monocyclic aryldiazonium salts, which suggest that cations with lower lying electron-acceptor levels are more easily grafted than electron rich cations.

This work shows, for the first time, the spontaneous grafting of diazonium derivatives of nPAHs onto amorphous carbon substrates. Our results indicate that the spontaneous grafting of diazonium derivatives of nPAHs can lead to different layers at carbon surfaces, depending on the position of the $-N_2^+$ functional group with respect to other substituents in the condensed ring system. This work presents a clear example of positional isomers displaying very different grafting behaviours and highlights the importance of substituent position which may be useful when choosing compounds for sensing and electronic applications.

2.5. References

(1) Adenier, A.; Barre, N.; Cabet-Deliry, E.; Chausse, A.; Griveau, S.; Mercier, F.; Pinson, J.; Vautrin-Ul, C. *Surface Science* **2006**, *600*, 4801.

(2) Barriere, F.; Downard, A. J. *Journal of Solid State Electrochemistry* **2008**, *12*, 1231.

(3) Le Floch, F.; Simonato, J.-P.; Bidan, G. *Electrochimica Acta* **2009**, *54*, 3078.

(4) Seinberg, J.-M.; Kullapere, M.; Mäeorg, U.; Maschion, F. C.; Maia, G.; Schiffrin, D. J.; Tammeveski, K. *Journal of Electroanalytical Chemistry* **2008**, *624*, 151.

(5) Abiman, P.; Wildgoose, G. G.; Compton, R. G. *Journal of Physical Organic Chemistry* **2008**, *21*, 433.

(6) Toupin, M.; Belanger, D. *Langmuir* **2008**, *24*, 1910.

(7) Lehr, J.; Williamson, B. E.; Downard, A. J. *Journal of Physical Chemistry C* **2011**, *115*, 6629.

(8) Bonifas, A. P.; McCreery, R. L. *Nature Nanotechnology* **2010**, *5*, 612.

(9) Bergren, A. J.; Harris, K. D.; Deng, F.; McCreery, R. L. *Journal of Physics: Condensed Matter* **2008**, *20*, 374117.

(10) Ru, J.; Szeto, B.; Bonifas, A.; McCreery, R. L. *ACS Applied Materials & Interfaces* **2010**, *2*, 3693.

(11) Ranganathan, S.; Steidel, I.; Anariba, F.; McCreery, R. L. *Nano Letters* **2001**, *1*, 491.

(12) Fan, F. R. F.; Yang, J. P.; Cai, L. T.; Price, D. W.; Dirk, S. M.; Kosynkin, D. V.; Yao, Y. X.; Rawlett, A. M.; Tour, J. M.; Bard, A. J. *Journal of the American Chemical Society* **2002**, *124*, 5550.

(13) James, D. K.; Tour, J. M. *Chemistry of Materials* **2004**, *16*, 4423.

(14) Jian, H.; Tour, J. M. *Journal of Organic Chemistry* **2005**, *70*, 3396.

(15) He, J.; Chen, B.; Flatt, A. K.; Stephenson, J. J.; Doyle, C. D.; Tour, J. M. *Nature Materials* **2006**, *5*, 63.

(16) Blanford, C. F.; Heath, R. S.; Armstrong, F. A. *Chemical Communications* **2007**, *17*, 1710.

(17) Agullo, J.; Canesi, S.; Schaper, F.; Morin, M.; Bèlanger, D. *Langmuir* **2012**, *28*, 4889.

(18) Cullen, R. J.; Jayasundara, D.; Soldi, L.; Cheng, J.; DuFaure, G.; Colavita, P. E. *Chemistry of Materials* **2012**, *24*, 1031.

(19) Sun, B.; Colavita, P. E.; Kim, H.; Lockett, M.; Marcus, M. S.; Smith, L. M.; Hamers, R. J. *Langmuir* **2006**, *22*, 9598.

(20) Price, C. C.; Voong, S.-T. *Organic Syntheses* **1948**, *28*, 80.

(21) Hermans, A.; Seipel, A. T.; Miller, C. E.; Wightman, R. M. *Langmuir* **2006**, *22*, 1964.

(22) Rodríguez, J. G.; Tejedor, J. L. *Journal of Organic Chemistry* **2002**, *67*, 7631.

(23) Bellamy, M. K. *Journal of Chemical Education* **2010**, *87*, 1399.

(24) Soldi, L.; Cullen, R. J.; Jayasundara, D. R.; Scanlan, E. M.; Giordani, S.;Colavita, P. E. *Journal of Physical Chemistry C* **2011**, *115*, 10196.

(25) Delamar, M.; Hitmi, R.; Pinson, J.; Savéant, J. M. *Journal of the American Chemical Society* **1992**, *114*, 5883.

(26) Librando, V.; Alparone, A. *Journal of Hazardous Materials* **2008**, *154*, 1158.

(27) Socrates, G. *Infrared and Raman characteristic group frequencies. Tables and Charts*; 3rd ed.; John Wiley & Sons: Chichester, **2001**.

(28) Jayasundara, D. R.; Cullen, R. J.; Soldi, L.; Colavita, P. E. *Langmuir* **2011**, *27*, 13029.

(29) Brooksby, P. A.; Downard, A. J. *Langmuir* **2004**, *20*, 5038.

(30) Allongue, P.; Delamar, M.; Desbat, B.; Fagebaume, O.; Hitmi, R.; Pinson, J.; Savéant, J.-M. *Journal of the American Chemical Society* **1997**, *119*, 201.

(31) Bräse, S.; Dahmen, S.; Popescu, C.; Schroen, M.; Wortmann, F.-J. *Chemistry--A European Journal* **2004**, *10*, 5285.

(32) Balz, G.; Schiemann, G. *Berichte der Deutschen Chemischen Gesellschaft* **1927**, *60*, 1186.

(33) Canning, P. S. J.; McCrudden, K.; Maskill, H.; Sexton, B. *Journal of the Chemical Society, Perkin Transactions 2: Physical Organic Chemistry* **1999**, *12*, 2735.

(34) March, J. *Advanced Organic Chemistry: Reactions, Mechanisms, and Structure.*; 4 ed.; John Wiley & Sons, Inc: New York, **1992**.

(35) Quintero, B.; Cabeza, M. C.; Martínez, M. I.; Gutiérrez, P.; Martínez, P. J. *Canadian Journal of Chemistry* **2003**, *81*, 832.

(36) Galli, G.; Martin, R. M.; Car, R.; Parrinello, M. *Physical Review Letters* **1989**, *62*, 555.

(37) Quintero, B.; Martínez Puentedura, M. I.; Megías, M. T.; Cabeza, M. C.; Gutiérrez, M. P.; Martínez de las Parras, P. J. *Journal of Chromatography, A* **2004**, *1035*, 227.

(38) Pazo-Llorente, R.; Maskill, H.; Bravo-Diaz, C.; Gonzalez-Romero, E. *European Journal of Organic Chemistry* **2006**, *9*, 2201.

(39) Pazo-Llorente, R.; Sarabia-Rodriguez, M. J.; Bravo-Diaz, C.; Gonzalez-Romero, E. *International Journal of Chemical Kinetics* **1999**, *31*, 73.

(40) Jayasundara, D.; Cullen, R. J.; Colavita, P. E. *Chemistry of Materials* **2013**, *25*, 1144.

3. Heterogeneous charge transfer at the amorphous carbon/solution interface: effect on the spontaneous attachment of nPAH aryldiazonium salts

An experimental investigation into the kinetics of spontaneous grafting of nPAH aryldiazonium salts onto amorphous carbon surfaces is presented. This work aimed to explore the fundamental processes occurring at the carbon/solution interface during the spontaneous grafting reaction and to provide a detailed study of charge transfer properties of the carbon materials used. The effect that changes in carbon composition and electronic properties have on rates and yields of this reaction are not well understood. Disordered amorphous carbon surfaces provide an interesting platform for investigating these effects via interfacial reactions. This is owing to the fact that the electronic structure and chemical composition of amorphous carbons can be fine-tuned over a wide range, allowing a systematic approach to understanding carbon surface chemistry. The following chapter presents an investigation into the effect that heterogeneous charge transfer at the carbon/solution interface and changes in carbon sp^2 content have on the rate, yield and mechanism of the spontaneous chemisorption of nPAH aryldiazonium salts.

Murphy, D. M.; Cullen, R. J.; Jayasundara, D. R.; Doyle, R. L.;
Lyons, M. E. G.; Colavita, P. E.;
Heterogeneous charge transfer at the amorphous carbon/solution interface; effect on the spontaneous attachment of aryldiazonium salts
J. Phys. Chem. C, **2013**, *117*, 22768-22777.

3.1. Introduction

The chemisorption of aryldiazonium salts at carbons is a versatile surface modification methodology that has found multiple applications in fields as diverse as bioimaging, electronic devices and sensors.[1-4] There has been great interest in trying to understand the mechanism of this reaction at carbons in order to, in turn, improve control over structure, morphology and composition of resulting organic layers.

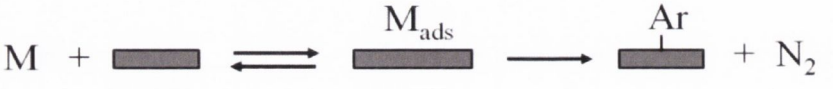

Scheme 3.1. Proposed mechanism of aryldiazonium salt chemisorption reactions.

The spontaneous chemisorption reaction is thought to proceed via a first step in which electron transfer from the substrate to the aryldiazonium cation leads to the formation of a reduced adsorbate species. In a second step, the adsorbate undergoes dediazoniation leading to chemisorption via aryl—surface covalent bonds as shown in Scheme 3.1.[5-8] Assuming reductive adsorption is rate determining, rates of reaction are expected to depend on the overlap between surface donor states and molecule acceptor states.[1] Experimental evidence that supports this proposed mechanism has been provided for spontaneous aryldiazonium grafting at ordered carbon nanomaterials such as nanotubes[7-10] and graphene.[1,6] Recently, work from our group has shown that the proposed mechanism can be used to rationalize reaction trends of carbon materials that do not display long range order, such as amorphous carbons. This work aimed to develop a structure-reactivity relationship between the physical and chemical properties of amorphous carbon films and their surface reactivity via spontaneous modification using aryldiazonium salts. We have shown that when the electronic properties of amorphous carbon change from metallic to semiconducting, adsorption rates drop dramatically.[11]

Conversely, molecular acceptor levels can strongly affect adsorption rates at amorphous carbons. For instance in the previous chapter, we demonstrated using *in situ* spectroscopy that adsorption rates of 4-nitronaphthalene (4NND) and 5-nitronaphthalene (5NND) diazonium tetrafluoroborate, two positional isomers (see Scheme 3.2), were remarkably

different.[12] These differences were explained on the basis of their reduction potential, given that adsorption and chemisorption rates were faster for 4NND, the isomer that had a lower lying acceptor level, than for 5NND.[12]

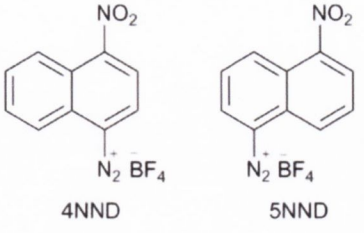

4NND 5NND

Scheme 3.2. Structures of 4-nitronaphthalene diazonium tetrafluoroborate (4NND) and 5-nitronaphthalene diazonium tetrafluoroborate (5NND).

Herein we report on results which suggest that when a carbon surface is exposed to more than one aryldiazonium salt, diazonium cations will establish a kinetic competition for surface sites based on their reduction potential. We show that it is possible to switch-off such competition by changing the electronic properties of the amorphous carbon substrate. Using a combination of spectroscopic and electrochemical methods, we characterized two amorphous carbon materials that differ by their degree of graphitization, and investigate their reactions *in situ* and *ex situ* with the two isomeric aryldiazonium cations 4NND and 5NND.

To our knowledge this is the first time that a modification of electronic properties is shown to control relative reaction rates at the carbon/solution interface in disordered carbon materials. A discussion of our results in light of our current understanding of aryldiazonium chemisorption reactions and available models of charge-transfer at the solid/liquid interface is given. In particular, we show that Gerischer-Marcus theory can be used to make semiquantitative predictions on charge transfer rates at amorphous carbons and we used this approach in order to interpret our experimental observations of relative adsorption rates.

3.2. Experimental

3.2.1. Chemicals and Materials

4-Nitrobenzylamine hydrochloride (97%), potassium chloride (99%), potassium ferricyanide (99+%), potassium nitrate (≥98%) hydrogen peroxide (H_2O_2, 30%), hexammineruthenium(III) chloride (98%), hexammineruthenium(II) chloride (99%) and sulfuric acid (95-97%) were obtained from Sigma and used as received. Degassed deionized water was used for all aqueous solutions. 4-Nitronaphthalene diazonium tetrafluoroborate (4NND) and 5-nitronaphthalene diazonium tetrafluoroborate (5NND) were synthesized as described in the previous chapter and in the literature.[12] 4-Nitrobenzylamine (4NBA) was prepared from 4-nitrobenzylamine hydrochloride salt using published methods.[13]

3.2.2. Preparation of carbon substrates

Amorphous carbon films with thicknesses in the range 40-50 nm were prepared via DC-magnetron sputtering (Torr International, Inc.) at a base pressure $\leq 2 \times 10^{-6}$ mbar and a deposition pressure of 7×10^{-3} mbar, as described in the literature and in the previous chapter.[11] Sputter-coating was performed on silicon for infrared, Atomic Force Microscopy (AFM), Raman and photoelectron spectroscopies, on quartz slides (UQG Optics) for UV−vis measurements and on glassy carbon (GC) substrates for electrochemical measurements. GC substrates (SPI-Glas™ 11 Grade) were polished with 0.3 μm alumina slurry (Buehler), rinsed with water, immersed for 20 s in piranha solution (3:1, H_2SO_4 to H_2O_2) to remove the polishing debris layer and rinsed with abundant water.[14] Annealing was carried out in a tube furnace at 500°C and 700°C for 1 h under N_2 atmosphere.

3.2.3. Functionalization of carbon substrates

In situ real time analysis of the spontaneous grafting of 1×10^{-4} M solutions of aryl diazonium salts onto carbon substrates was monitored using a custom built ATR-FTIR, as previously reported.[11-12] Spectra were obtained at regular times upon commencement of reaction of using a Bruker Tensor 27 FTIR; 100 scans at 4 cm^{-1} resolution were averaged for each measurement over 3 h. The symmetric N—O stretching peak (1342 cm^{-1}) was

chosen for the analysis because it was less affected by interference from water vapor peaks than the asymmetric stretching peak (~1530 cm^{-1}). Spectra were normalized for optical pathlength using a 0.2 M aqueous KNO_3 solution, and for absorption cross-section using an internal standard method, as previously described.[12] Substrates for AFM analysis were functionalized via immersion in 1×10^{-4} M aqueous solutions of aryldiazonium salts for 1 h. Aryldiazonium grafting on GC substrates was carried out via immersion in aqueous solutions of the salts for varying lengths of time. The substrates were washed, sonicated in DI H_2O and dried under an Ar flow prior to electrochemical analysis.

3.2.4. Characterization

Raman spectra were obtained using the 514 nm line of an Ar^+ laser on a micro-Raman system (Renishaw 1000) equipped with a CCD camera and a Leica microscope with 1 cm^{-1} spectral resolution. In order to obtain I_D/I_G ratios, peaks were fitted using a combination of a Breit-Wigner-Fano and a Lorentzian peak)[15] using commercial software (Igor Pro 6.04). UV–vis transmission measurements of amorphous carbon films were collected over the wavelength range 200–890 nm at 1 nm resolution (Shimadzu UV-2401 PC) from carbon samples deposited on quartz substrates. AFM measurements (NT-MDT, Asylum) were carried out in tapping mode with a frequency of 1 Hz and 512 scan lines; root-mean-square (RMS) roughness values were calculated over 2×2 μm^2 boxes with measurements carried out in triplicate. X-ray and Ultraviolet photoelectron spectroscopy (XPS and UPS) measurements of carbon substrates were carried out in an Omicron system with a multichannel array detector, at 1×10^{-10} mbar base pressure. XP spectra were recorded at room temperature at 45° take-off angle with an analyzer resolution of 0.5 eV using a monochromatized Al K_α source (1486.6 eV). Peaks were fitted to Voigt functions after Shirley background correction, using commercial software (Igor Pro 6.04). Atomic ratios were obtained from area ratios using sensitivity factors (C = 0.296; O = 0.711). UPS spectra were taken using a He(I) line as an excitation source, a take-off angle of 90° and an analyzer resolution of 0.02 eV. Measurements were collected by applying a negative bias to the sample in order to measure the high binding energy edge of the photoelectron spectrum. Spectra were corrected for bias and referenced to the Fermi energy, as measured from the Fermi step of a copper clip in electrical contact with the carbon substrates.[16] In order to compare spectra of different carbon samples, curves were normalized by the total integrated

intensity for binding energies greater than 11.0 eV; relative spectral intensities near the Fermi energy were found to be similar when the normalization was carried out using the full energy range. The work function was calculated from the difference between the incident photon energy (21.2 eV) and the energy cutoff at high binding energy. The cutoff value was determined from the intercept of linear fits of the spectrum before and after the emission threshold.[17-18]

Electrochemical measurements were carried out in a home built Teflon cell in which the carbon substrate was utilized as the working electrode (0.067 cm^2), with a Pt wire and Ag/AgCl, KCL (3M) acting as counter and reference electrodes, respectively. Cyclic voltammetry measurements were obtained on a CHI660C potentiostat at room temperature in Ar-purged 0.1 M H_2SO_4 solutions. Electrochemical impedance spectroscopy (EIS) was carried out on an Autolab potentiostat (Model PGSTAT302N) at room temperature in Ar purged solutions containing 0.0010 M equimolar concentrations of hexaminerutheniu(II) chloride and hexaminerutheniu(III) chloride, and 0.1 M KCl as supporting electrolyte. The formal potential (E_0') for the Ru(II)/Ru(III) redox couple was determined for each surface using cyclic voltammetry. Impedance spectra were performed at E_0' for each surface; an equilibration time of 5 min at the applied potential was employed before each impedance measurement. The frequency response was recorded between 100 kHz and 0.1 Hz using a sinusoidal voltage with an amplitude of 10 mV. Equivalent electrical circuit modeling was performed using Nova (Version 1.8). Intercalation experiments were carried out in accordance with published methods,[11,13] via immersion of carbon substrates in 6×10^{-4} M acetonitrile solutions of 4NBA for 2 h. Samples were rinsed with abundant acetonitrile and dried under argon before cyclic voltammetry characterization.

3.3. Results

3.3.1. Properties of annealed amorphous carbon films

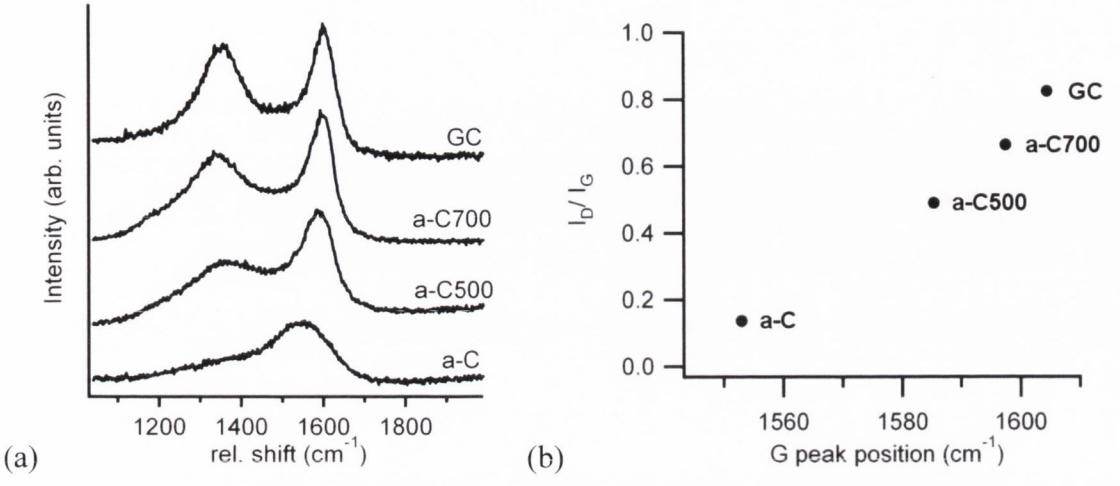

Figure 3.1. (a) Raman spectra (514 nm) of carbon films as deposited (a-C), after annealing at 500 °C (a-C500) and 700 °C (a-C700) for 1 h, and of glassy carbon (GC). (b) I_D/I_G vs. G peak position for a-C, a-C500, a-C700 and GC.

Amorphous carbon films (a-C) were deposited via DC magnetron sputtering as previously described.[11] These films had been shown to be semi-metallic in character and to possess an sp^2 content of (80 ± 4)%, as determined via XPS.[11] a-C films were then annealed under a nitrogen atmosphere in order to increase their sp^2 carbon content. The bulk properties of our various carbon materials were characterized using Raman spectroscopy. Figure 3.1.(a) shows the Raman spectra of the as deposited a-C film, and of a-C after annealing at 500 °C (a-C500) and 700 °C (a-C700); the spectrum of glassy carbon (GC) is reported for comparison, along with a-C500, which was merely utilized as a way of testing that we were progressively changing the properties of the carbon with increasing temperature. All spectra show the characteristic D and G peaks of amorphous carbons which occur due to sp^2 sites. The G peak is as a result of bond stretching of pairs of sp^2 atoms whereas the D peak is due to the breathing modes of rings.[15] Upon annealing, both D and G peaks become narrower, while the G peak also shifts towards higher wavenumbers; this is consistent with increasing sp^2 content and graphitization in the carbon film.[19-20] Spectra were fitted using a combination of a Breit-Wigner-Fano and a Lorentzian peak as proposed by Ferrari *et al.*[15] This yielded I_D/I_G height ratios of 0.1, 0.5 and 0.7 for a-C, a-C500 and a-C700. Based on Ferrari's three-stage model for amorphous carbons, these ratios correspond to a change in

sp^2 content from ~80% to ~100% upon annealing,[11,15] as illustrated in Figure 3.1.(b). A qualitative comparison of the Raman spectrum of a-C700 to that of GC, a 100% sp^2 disordered carbon material, also suggests that a-C700 has ~100% sp^2 content. The Raman spectrum of the GC substrate was measured by my colleague Ronan Cullen.

The change in sp^2 content also affects the optical properties of a-C films. Figure 3.2.(a) shows a 50 nm a-C film deposited on quartz before (left) and after (right) annealing at 700 °C, where the as-prepared film displays greater transparency than the annealed one. The absorptivity of a-C films increased significantly upon annealing as expected in the case of carbon graphitization.[19,21-23] Absorbance measurements were used to generate Tauc plots[11,24] for annealed carbon films, which yielded negative bandgap values for a-C700 of -0.8 eV (vs. 0.6 eV for a-C) as illustrated in Figure 3.2.(b). Zero or negative Tauc gap values have been reported in the literature and are consistent with semi-metallic electronic properties in deposited films.[25-26]

(a) 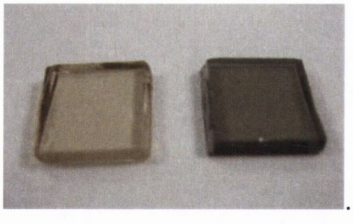 (b) 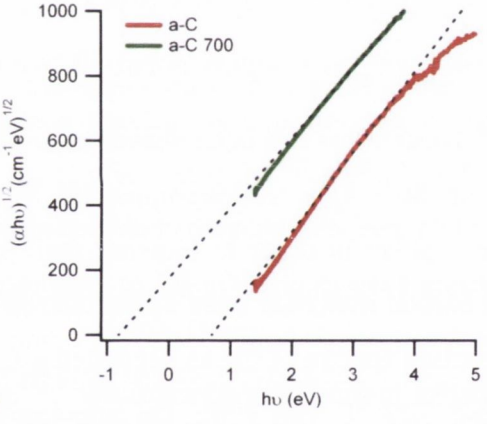

Figure 3.2. (a) a-C deposited on quartz before (left) and after (right) annealing at 700 °C. (b) Typical Tauc plots of as prepared amorphous carbon films (a-C) and after annealing at 700°C (a-C700).

An increase in the concentration of sp^2 bonded carbon upon annealing was also evident from X-ray photoelectron (XP) spectra; Figure 3.3. shows the C 1s spectrum of a-C and a-C700 surfaces. The main peak shifts to lower binding energies and becomes narrower after annealing at 700 °C, indicating a decrease in the contributions from sp^3 carbon centres.[27-28] XP analysis of a-C and a-C700 revealed that the oxygen content of the carbon samples decreased after annealing. The as-deposited a-C films used have a reported oxygen content

of 9 %[11] whereas analysis of the O 1s peak for a-C700 yielded an O/C ratio of 3.3 %. XPS measurements were carried out by my colleague Ronan Cullen.

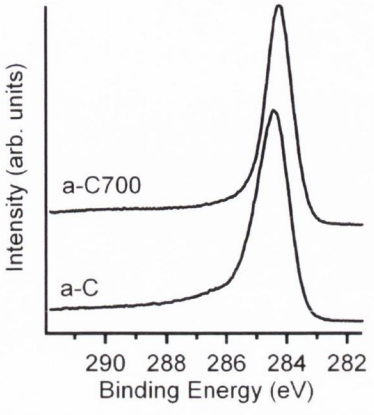

Figure 3.3. C 1s XP spectra of a-C and a-C700 films.

An increase in the concentration of sp^2 carbon centers is often accompanied by graphitization, whereby sp^2 centers organize into more and larger graphitic clusters. In order to obtain information on the relative density of graphitic edge planes exposed at the carbon surface before and after annealing, intercalation studies using 4-Nitrobenzylamine (4NBA) were carried out, following methods developed by Compton and co-workers.[13] 4NBA has been shown to partially intercalate between exposed graphitic edge planes and the total charge associated to the electroreduction of intercalated nitroaryl groups to arylamines can be used to estimate the surface density of intercalation sites.

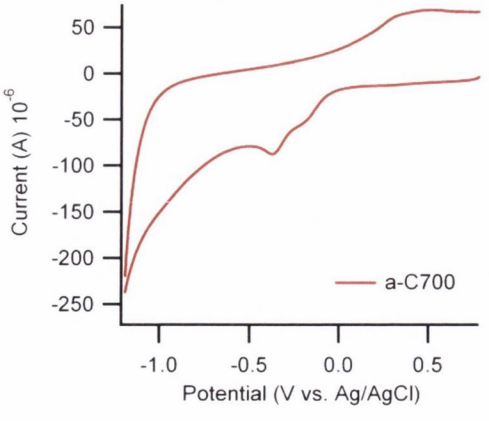

Figure 3.4. Cyclic voltammetry of a-C700 electrodes modified via partial intercalation of 4NBA in acetonitrile solution, measured in 0.1 M H_2SO_4 at 0.2 V s^{-1}.

Cyclic voltammetry of 4NBA-intercalated a-C700 samples was used in order to obtain the electroreduction charge of intercalated nitroaryl groups to arylamines. A cyclic voltammogram carried out in 0.1 M H_2SO_4 at 0.2 V s^{-1} of an a-C700 electrode following 4NBA intercalation is given in Figure 3.4. The integrated charge associated with reduction and oxidation peaks yielded a 4NBA surface density of $(19.5 \pm 1.8) \times 10^{-10}$ mol cm^{-2} (95% C.I.) This value suggests a significantly greater density of graphitic edge planes at annealed carbon surfaces when compared to the previously reported value for a-C of $(3.4 \pm 0.9) \times 10^{-10}$ mol cm^{-2} (95% C.I.).[11] These results therefore indicate that both an increase in sp^2 carbon and graphitic clusters and edges take place upon annealing; the effect of these changes on adsorption reactions will be discussed in the following section.

3.3.2. *In situ* and *ex situ* studies of 4NND and 5NND adsorption at amorphous carbon substrates

In situ spectroscopic studies of aryldiazonium adsorption at annealed carbon surfaces were carried out via Attenuated Total Internal Reflectance Fourier Transform Infrared Spectroscopy (ATR-FTIR), using 4NND and 5NND in solution. Carbon films were deposited and annealed at 700 °C onto a Si trapezoid; the trapezoid was incorporated into a flow cell for studying the carbon/solution interface in real time.

Figure 3.5.(a) shows an example of ATR-FTIR spectra in the region of the symmetric N—O stretching absorption over the course of a reaction; the peak is seen to increase during deposition. The net absorbance at 1342 cm^{-1}, after normalization by optical pathlength and absorption cross-section, was used to provide a quantitative estimate of relative surface coverage for 4NND and 5NND vs. time, as previously described.[11-12]

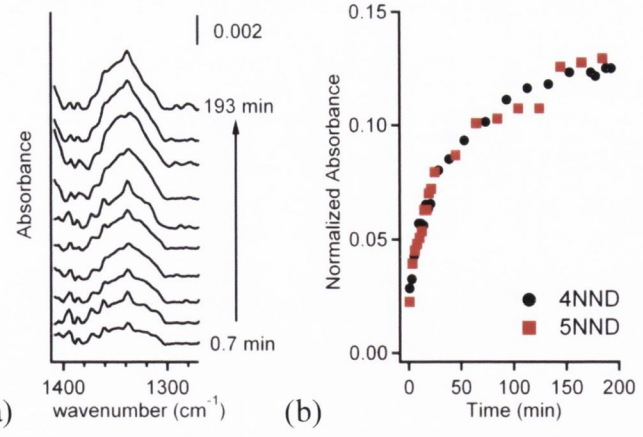

Figure 3.5. (a) Symmetric -NO_2 stretching peak of 4NND obtained via in situ ATR-FTIR at a-C700 surfaces after injection of 1×10^{-4} M 4NND. (b) Adsorption curves for 4NND and 5NND at a-C700, after normalization.

Figure 3.5.(b) shows adsorption curves for the two aryldiazonium isomers over 3 h of reaction time; the curves indicate that the two isomers display the same rate of adsorption at a-C700 surfaces. This result is somewhat surprising given that 4NND is significantly easier to reduce than 5NND, with 4NND acceptor levels positioned 0.250 eV below those of 5NND as shown in Chapter 2.[12] This difference would suggest that adsorption rates should be larger for 4NND, as is indeed the case when adsorption rates are measured at as-prepared a-C surfaces.[12] When comparing rates of adsorption at a-C vs. a-C700 we found that adsorption rates for 4NND increase slightly, whereas those of 5NND increase dramatically, as can be observed in Figure 3.6.(a) and (b).

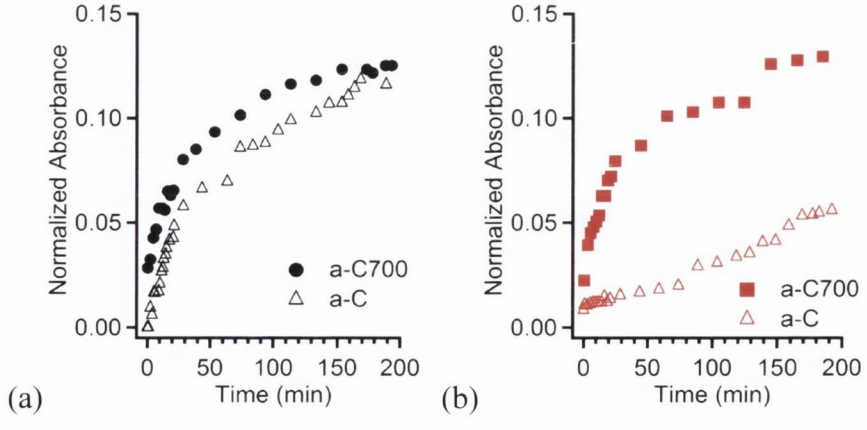

Figure 3.6. Comparison of adsorption curves of 4NND (a) and 5NND (b) at a-C and a-C700 obtained from 1×10^{-4} M solutions over 3 h of reaction.

Therefore, our *in situ* adsorption studies of 4NND and 5NND at amorphous carbons suggest that (a) the change in carbon composition/electronic properties upon annealing leads to an overall increase in reaction rates; (b) the rate-determining step of the 4NND grafting reaction might not depend on interfacial electron transfer rates.

In order to compare the behaviour observed at a-C700 carbon surfaces with that at a reference non-crystalline 100% sp^2 material, we carried out *ex situ* measurements at glassy carbon electrodes (GC) via electrochemistry. The integrated charge associated to the electroreduction of nitroaryl groups was obtained via cyclic voltammetry using samples prepared from 1×10^{-4} M aqueous solutions of 4NND and 5NND, after increasing reaction times.

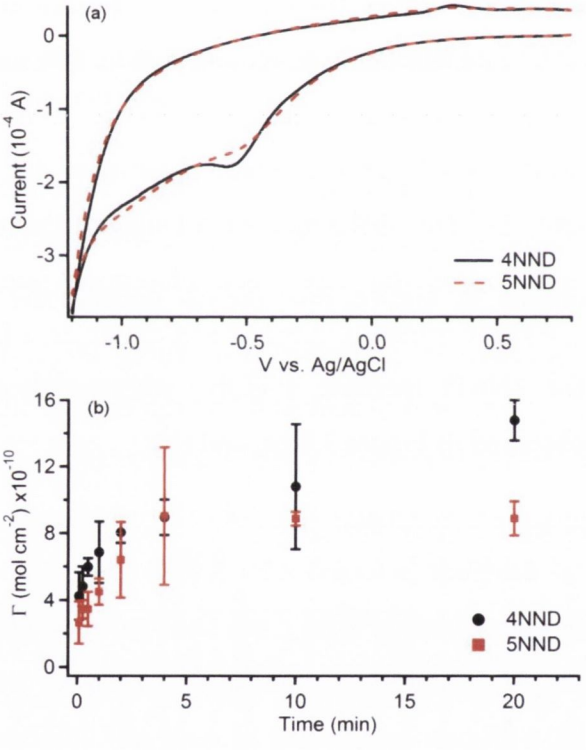

Figure 3.7. (a) Cyclic voltammograms of 4NND and 5NND-modified GC electrodes obtained in 0.1 M H_2SO_4 at 0.2 Vs $^{-1}$; substrates were modified by immersion in 1×10^{-4} M aqueous solutions of 4NND and 5NND for 10 min. (b) Surface coverage of nitroaryl groups (Γ) on GC substrates as a function of deposition time in 1×10^{-4} M 4NND (●) and 5NND (■) aqueous solutions.

Figure 3.7.(a) shows a typical cyclic voltammogram after deposition of 4NND and 5NND at GC electrodes; both peak potential and total charge associated to the reduction peak are similar for 4NND and 5NND adlayers. Figure 3.7.(b) shows the surface density of

nitroaryl groups at GC substrates obtained *ex situ* via this methodology vs. reaction time. Surface coverage in Figure 3.7.(b) is seen to increase at similar rates for both molecules, measurements taken after 2 h of deposition indicated that the surface coverage levels off after 20 min. The limiting coverage was found to be 15×10^{-10} and 8.9×10^{-10} mol cm^{-2} for 4NND and 5NND, respectively, and slightly higher than a close-packed monolayer (1 ML = 6.01×10^{-10} mol/cm^2).[30] These results indicate that, although there is a difference in the limiting surface density of Ar-NO_2 in adlayers consisting of 4NND and 5NND at GC electrodes, the initial rate of adsorption of these two aryldiazonium cations is the same, in agreement with *in situ* measurements. Therefore, adsorption of the two positional isomers at GC as in the case of a-C700, is not controlled by the position of the molecular acceptor level.

AFM characterization of bare and functionalized carbon samples was carried out in order to monitor potential differences in surface morphology among these substrates. AFM measurements were carried out by my colleague Ronan Cullen. Root mean square (RMS) roughness values of 1.40 ± 0.07 and 1.31 ± 0.13 nm were obtained for bare a-C and annealed a-C substrates, respectively. RMS roughness values for bare and aryldiazonium modified a-C and a-C700 surfaces are given below in Table 3.1. Substrates were modified via immersion in 1×10^{-4} M aqueous solutions of aryldiazonium salts for 1 h.

Table 3.1. RMS roughness values for bare and modified a-C and a-C700 substrates measured using AFM.

RMS values (nm)	bare	4NND	5NND
a-C	1.40 ± 0.07	1.01 ± 0.03	0.98 ± 0.06
a-C700	1.31 ± 0.13	1.01 ± 0.06	1.07 ± 0.14

No significant difference between the morphologies of the two bare carbon samples can be identified. In agreement with previous reports from our group, a slight decrease in roughness upon modification with aryldiazonium salts is observed.[29] It can also be understood from this data that there is very little difference in the surface morphology of 4NND and 5NND adlayers.

3.3.3. Valence structure at amorphous carbons

The adsorption rate of aryldiazonium salts at carbon surfaces has been previously interpreted using the Marcus-Gerischer theory of charge transfer.[6] We were interested in understanding whether aryldiazonium cation adsorption at amorphous carbons could also be explained under the same theoretical framework. In order to do that we carried out experimental studies of the valence electronic structure and of charge transfer rates at as prepared and annealed samples via Ultraviolet photoelectron spectroscopy (UPS) and electrochemical impedance spectroscopy (EIS). The full UPS spectra of a-C as deposited and after annealing, shown in Figure 3.8., illustrates broad features and poorly defined peaks characteristic of amorphous carbons.[31-33] UPS measurements were carried out by my colleague Ronan Cullen.

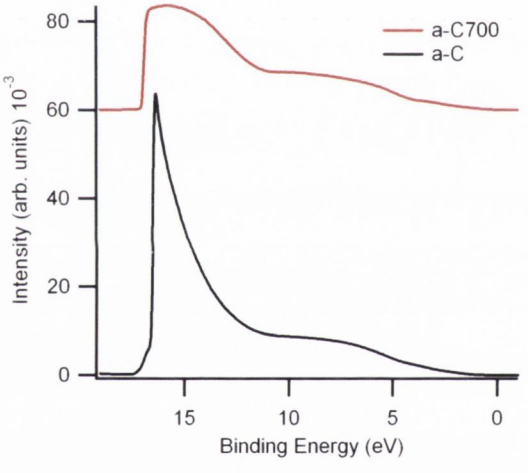

Figure 3.8. Normalized UPS spectra of a-C700 and as deposited a-C surfaces with spectra offset for clarity.

Figure 3.9.(a) shows the high-binding energy region of normalized UPS spectra of annealed a-C700 and as deposited a-C substrates. The high-binding energy emission threshold was fit to a line and extrapolated to the energy axis in order to calculate the high-binding energy cutoff value. This energy value was subtracted from the source photon energy (21.2 eV) to yield work function values of (4.2 ± 0.1) eV and (4.6 ± 0.1) eV for annealed a-C700 and as deposited a-C surfaces, respectively. The annealing treatment reduces the work function by 0.4 eV bringing its value close to that of 100% sp^2 glassy carbon (4.2 eV).[34] This indicates

that the sputtered carbon sample undergoes graphitization, in agreement with Raman, UV and XPS results shown in Figures 3.1., 3.2., and 3.3., respectively.

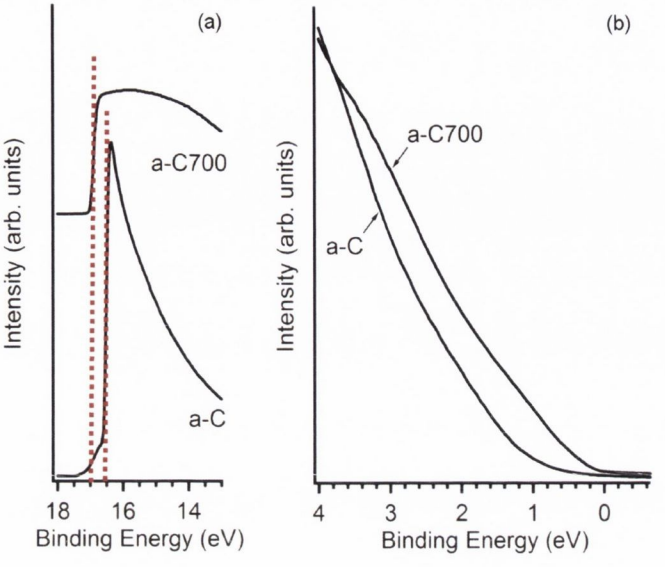

Figure 3.9. (a) High and (b) low binding energy regions of normalized UPS spectra of annealed carbon (a-C700) and as deposited amorphous carbon (a-C) surfaces.

A decrease in work function after annealing is accompanied by an increase in photoelectron emission for energies near the Fermi energy (E_F), which can be observed in the low-binding region of the UPS spectra shown in Figure 3.9.(b). Marked enhancements in valence photoemission are observed for the annealed a-C700 film when compared to that of the as deposited a-C surface in the 0-4 eV region. This region is associated with contributions from p – π states in amorphous carbons and polycrystalline graphite.[31-33] The onset of photoemission approximately coincides with E_F in the case of a-C700, whereas for a-C the photoemission intensity is negligible (below noise equivalent level) in the region 0.19 eV-E_F; this suggests that a-C700 has a greater semi-metallic character than a-C. Importantly, UPS results indicate that at the solid/vacuum interface, annealed a-C700 possesses higher lying occupied electronic states compared to pristine a-C.

3.3.4. Electron transfer studies at amorphous carbons

The kinetics of electron transfer at the carbon/solution interface was investigated using EIS in solutions of $Ru(NH_3)_6^{+3/+2}$, a reversible redox couple with formal potential of E_0'= 0.034 V vs. SHE, at both amorphous carbon electrodes. Typical complex plane impedance

(Nyquist) plots recorded for each carbon surface are shown in Figure 3.10. A modified Randles circuit, shown in the inset of Figure 3.10. was found to give the best fit with an average χ^2 value of 0.05. In this equivalent circuit the resistance R_s represents the electrolyte resistance; the parallel combination of the constant phase element (CPE_p) and a resistance (R_{CT}) represent the double layer capacitance and the charge transfer resistance, respectively; finally, the Warburg element (W) models the diffusional impedance. The values of fitting parameters for the data from Figure 3.10. are presented in Table 3.2.

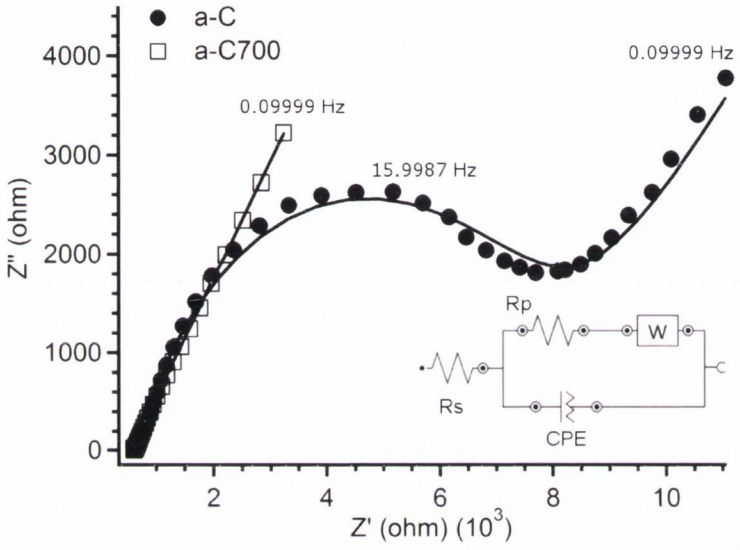

Figure 3.10. Experimental impedance data represented as Nyquist plots for a-C and annealed a-C700 electrodes with frequencies at maximum Z. Continuous lines show the best fit of EIS data using the equivalent circuit shown in the inset.

Table 3.2. Values of fitting parameters for a-C and a-C700 from Figure 3.10.

	a-C	**a-C700**
R_{CT}	7.35 kΩ	39.7 Ω
R_s	654 Ω	603 Ω
W	264 γ_0	207 γ_0
CPE_p	4.3 μMho	111 μMho

Figure 3.10. shows a large semicircular feature at high frequencies for as deposited a-C electrodes; this indicates that a significant charge transfer resistance, R_{CT} exists. The same feature is considerably smaller for annealed a-C700 electrodes, which display an impedance response dominated by the Warburg diffusional impedance. The Nyquist plot of

a-C700 suggests that this material is highly graphitic and behaves similarly to 100% sp^2 glassy carbon electrodes, this is supported by a comparison of a-C700 and GC EIS data which is shown in Figure 3.11.

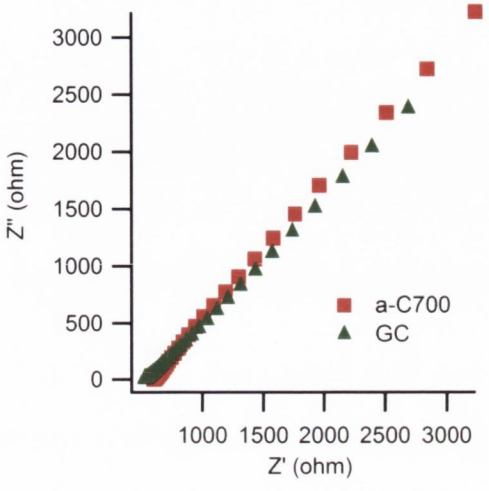

Figure 3.11. Experimental impedance data represented as Nyquist plots for a-C700 and GC electrodes.

These results indicate that charge transfer rates for the $Ru(NH_3)_6^{+3/+2}$ couple are faster at a-C700 than at a-C electrodes. Using the values for R_{CT} obtained from the equivalent circuit fitting, the exchange current density (j_0), the exchange current (i_0) and thereby, the standard heterogeneous rate constant (k^0) could be calculated from Equations 3.1., 3.2., and 3.3. where R is the molar gas constant, T is temperature, F is Faradays constant, A is area and C is concentration.[35]

$$R_{CT} = \frac{RT}{Fj_0} \qquad \text{(Eqn 3.1.)}$$

$$i_0 = j_0 A = k^0 FCA \qquad \text{(Eqn 3.2.)}$$

$$k^0 = \frac{i_0}{FAC} \qquad \text{(Eqn 3.3.)}$$

Electron transfer heterogeneous rates constants k^0 were found to be 5.7×10^{-4} cm s^{-1} and 7.2×10^{-2} cm s^{-1} for a-C and a-C700 electrodes, respectively, in good agreement to previous determinations of k^0 for pyrolyzed photoresist film electrodes.[36-37] Importantly, these EIS results reveal a significant difference of two orders of magnitude in electron transfer rates at

annealed a-C and as deposited a-C surfaces. In order to understand whether trends in electron transfer and in aryldiazonium interfacial adsorption can be explained by differences in electronic structure between these two carbon substrates, we analysed the observed results under the framework of Marcus and Marcus-Gerischer theories of electron transfer as in the following section.

3.4. Discussion

Two amorphous carbon substrates that differ in graphitic content and two aryldiazonium cation isomers were used in this work in order to investigate interfacial reactivity trends. One of the carbon substrates, a-C, displays an estimated trigonally bonded carbon content of 80%, whereas the other one, a-C700, is 100% graphitic. The two aryldiazonium cations, shown in Scheme 3.2. are structural isomers, display the same surface geometric cross section but differ in the position of their electron acceptor level: 4NND is easier to reduce than 5NND by 250 mV, as shown in the previous chapter and tabulated below.[12] This choice of molecules and substrates offers the opportunity to test some of the hypotheses advanced by us and others in the literature for the mechanism of spontaneous reactions of diazonium compounds at surfaces, as well as for explaining the interfacial reactivity of amorphous carbon materials.

Table 3.3. Summary of electrochemical potentials of redox species used in our experiments referenced to SHE and to the vacuum level.

	4NND	**5NND**	**$Ru(NH_3)_6^{3+/2+}$**
E_0' (V) vs SHE	0.29 ± 0.01	0.04 ± 0.02	0.03 ± 0.002
E_0' (V) vs SHE_{vacuum}	4.72 ± 0.01	4.47 ± 0.02	4.46 ± 0.002

The amorphous carbon substrates examined, despite being both of high graphitic content, display marked differences in their electronic properties. The annealed sample, a-C700, has a negative Tauc gap which is characteristic of semi-metallic materials; a-C samples, on the other hand, have a small but finite Tauc gap. The semi-metallic character of a-C700 and the presence of a small optical gap in a-C are consistent with UPS measurements which indicate that the onset of emission for a-C700 coincides with E_F whereas in the case of a-C

it is positioned ~0.2 eV below E_F. UPS measurements also show that (a) the intensity of photoemission in the 4-0 eV binding energy region is higher and (b) that the work function is lower for a-C700 than for a-C. UPS results therefore indicate that based on thermodynamics arguments, a-C700 should behave as a better electron donor in charge transfer reactions because it possesses higher lying donor states than a-C.

Electrochemical impedance measurements also indicate that the kinetics of electron transfer is faster at a-C700 than at a-C surfaces. The electron transfer rate constant (k^0) $Ru(NH_3)_6^{+3/+2}$ for was found to be 126 times higher for a-C700 relative to a-C. Given that $Ru(NH_3)_6^{+3/+2}$ is an outer-sphere redox couple that has been shown to be rather insensitive to surface sites but sensitive to the density of states (DOS) of carbon electrodes,[38] it is interesting to interpret observed differences in k^0 on the basis of DOS differences near the Fermi level of these two carbon materials. Theories of charge transfer have been successfully used in the recent literature to model electron transfer rates obtained from electrochemical measurements at carbon electrodes. For instance, Compton and co-workers have used Marcus-Hush theory to relate electron transfer rates to the DOS of a graphite microelectrode;[39] Heller *et al.*[40] and Szroeder *et al.*[41-42] have used Gerischer-Marcus (GM) theory in order to model electron transfer rates based on the DOS distribution of carbon nanotube electrodes. GM theory has also been used to interpret and model spontaneous electron transfer from graphene nanoribbons and carbon nanotubes to aryldiazonium cations.[5-6] Therefore, in our analysis we decided to use GM theory in order to discuss under the same framework both EIS findings and spontaneous reactions of aryldiazonium at amorphous carbon electrodes.

GM theory considers that electron transfer rates depend on the overlap between occupied donor and unoccupied acceptor states. For electron transfer from the electrode to an oxidized species in solution, the electron transfer rate at energy E is proportional to the number of unoccupied states in solution $W_{ox}(E)$, and to the number of occupied states at the electrode $DOS_{occ}(E)$, where $DOS_{occ}(E)$ depends on the applied electrode potential. The total electron transfer rate constant, k_r, is proportional to the overlap integral over all possible energies:[6,42]

$$k_r \propto \int_{-\infty}^{+\infty} DOS_{occ}(E) W_{ox}(E) dE \qquad \text{(Eqn 3.4.)}$$

The energy distribution of states in solution is assumed to be a Gaussian:[35]

$$W_{ox}(E) = \frac{1}{\sqrt{4\pi\lambda kT}} \exp\left(- \frac{(E - (\lambda + E_{redox}))^2}{4\pi\lambda kT} \right) \qquad \text{(Eqn 3.5.)}$$

where k is Boltzmann's constant, T is temperature, λ is the reorganization energy and E_{redox} is the redox potential of the species in solution.

Assuming that the proportionality pre-factor is the same for both a-C700 and a-C substrates, Equation 3.4. allows us to estimate the relative values of electron transfer rate constants for $Ru(NH_3)_6^{+3/+2}$ from the occupied density of states in order to compare it to experimentally determined rate constants. In order to use Equation 3.4. to model relative electron transfer rates at amorphous carbons it is necessary to obtain the density of occupied states, $DOS_{occ}(E)$. The UPS photoemission intensity can be used for this purpose; however, this would generally require the UPS spectra to be corrected by the photoemission cross section.[43-44] If only the photoemission intensity over a narrow energy range within few eV of the Fermi level is used, we can assume that changes in cross section over this energy range are small so that the cross section can be included in the proportionality factor. Furthermore, if interested in relative values of rate constants, we can assume that photoemission cross sections are similar for both a-C and a-C700; this approximation is reasonable given that in this region the majority of photoelectrons originate from similar p-π states in both graphitic materials.[43] Using these assumptions, we can approximate the ratio between the electron transfer rate constants of a-C and a-C700 for spontaneous reductions as:

$$\frac{k_{r,aC}}{k_{r,aC700}} \cong \frac{\int_{E_{min}}^{E_F} I_{aC}(E) W_{ox}(E) d\varepsilon}{\int_{E_{min}}^{E_F} I_{aC700}(E) W_{ox}(E) d\varepsilon} \qquad \text{(Eqn 3.6.)}$$

where $I_{aC}(E)$ and $I_{aC700}(E)$ are the photoemission intensities of a-C and a-C700 surfaces, respectively, and $[E_{min}\,;\, E_F]$ defines an energy integration interval over occupied states at the electrode for which the overlap with acceptor states in solution is non-negligible (*vide infra*).

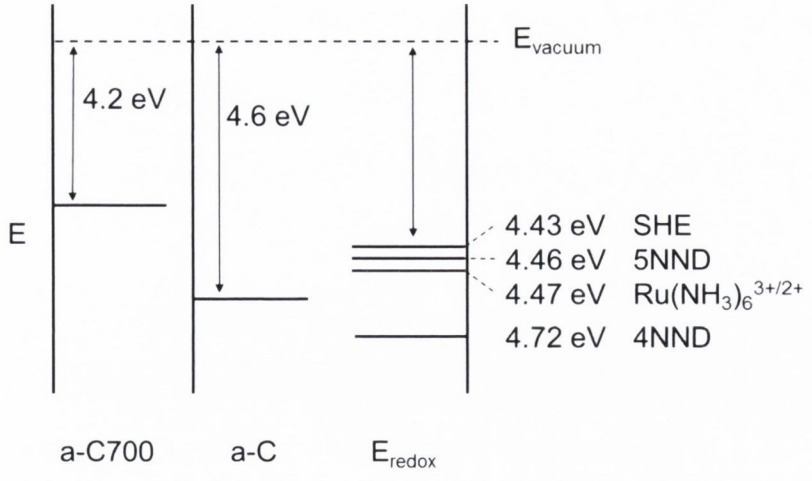

Figure 3.12. Schematic showing the Fermi levels obtained from work function determinations of carbon substrates in this chapter, the position of electron acceptor levels of 4NND and 5NND obtained from electrochemical measurements,[12] and the literature position of the Standard Hydrogen Electrode (SHE), all relative to vacuum.[45]

EIS measurements using $Ru(NH_3)_6^{+3/+2}$ were carried out at the formal potential, E_0', of the redox couple. Figure 3.12. shows the energy positions of the Fermi levels of carbon surfaces and redox species used in our experiments relative to vacuum; redox potentials were positioned with respect to vacuum using the absolute potential scale derived by Trasatti.[45] The figure shows that a negative potential of ~100 mV and a positive potential of ~300 mV must be applied to a-C and a-C700 electrodes, respectively, in order to bring their Fermi levels to coincide with E_0'. The density of occupied states $DOS_{occ}(E)$ depends on the applied potential; however, on a first approximation we can assume that whenever a small potential is applied to our carbon electrodes it is dropped primarily over the double layer. Therefore, upon applying a potential all valence band states simply shift in energy while maintaining the position of the Fermi level fixed with respect to band edges. This approximation is justifiable and less stringent than it would first appear, since amorphous carbons are rich in localized states and defects, which result in pinning of the Fermi level as shown for instance by Miyajima *et al.*[44] and Ilie *et al.*[46]

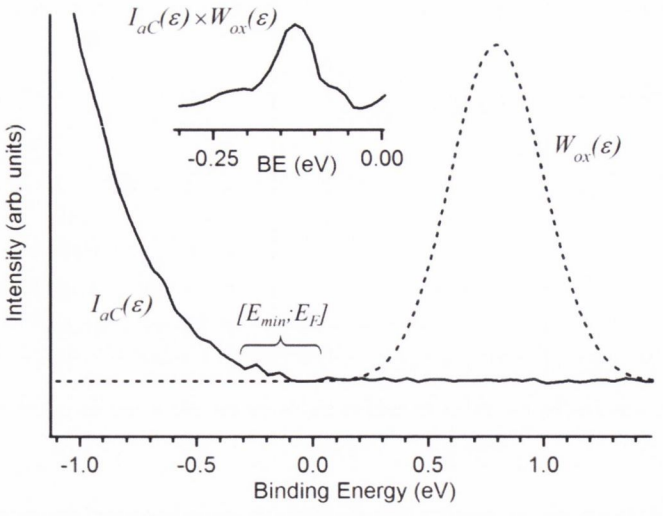

Figure 3.13. Example of the integration procedure used to calculate charge transfer rate constant ratios using the approximation in Equation 3.6.. The intensity of the UPS photoemission and the distribution of $Ru(NH_3)_6^{+3/+2}$ acceptor levels in solution are shown after alignment of their Fermi levels (E=0); the y-scaling is arbitrarily chosen for the two curves in order to facilitate graphical comparison. The inset shows the product of the two curves which defines a narrow energy interval over which the overlap can be integrated (indicated by the bracket).

Under the above approximations it is possible to calculate the ratio of electron transfer rate constants by integrating the overlap of the photoemission intensity and the acceptor state distribution after alignment of the Fermi levels. Figure 3.13. shows an example of this procedure in the case of a-C and $Ru(NH_3)_6^{+3/+2}$: the $W_{ox}(E)$ distribution was calculated according to Equation 3.5., assuming room temperature and a reorganization energy of 0.8 eV, as determined by Smalley *et al.* at gold electrodes.[47] The integral can then be calculated over a limited energy range over which the overlap is significant, as shown in the inset of Figure 3.13.

Following the above procedure we calculated the ratio of the overlap integrals between the normalized photoemission curves of a-C and a-C700 and the acceptor level distribution function of $Ru(NH_3)_6^{+3/+2}$ calculated by Equation 3.5. The GM prediction for the ratio $k_{r,aC}$: $k_{r,\,aC700}$ is 1 : 82, in good agreement with the ratio of 1 : 126 measured via EIS. This result suggests that the approximation described by Equation 3.4. offers a good approach for estimating relative charge transfer rate constant values at amorphous carbon electrodes.

The same procedure was used to estimate the rates of electron transfer to aryldiazonium cations in solution. The distributions of acceptor levels $W_{ox,4NND}(E)$ and $W_{ox,5NND}(E)$ were calculated using Equation 3.5., previously determined values of E_{redox},[12] and λ=0.7 eV, a value obtained by Nair *et al.*[5] by fitting kinetic data on the spontaneous reactions of a phenyldiazonium cations at carbon nanotubes to the GM model. Using Equation 3.6., the relative values of reduction rate constants for 4NND and 5NND at both a-C and a-C700 samples were then calculated, which are summarized in Table 3.4.

Table 3.4. Relative values of electron transfer rate constants for the spontaneous reduction of aryldiazonium cations in water at the two carbon surfaces investigated in this work, calculated using a Gerischer-Marcus model and Equation 3.6.

	Relative values of electron transfer rate constants	
	a-C	**a-C700**
4NND	355	1.8×10^6
5NND	1	1.0×10^5

It is clear from the values in Table 3.4 that for an electron-transfer mediated reaction step GM theory predicts faster reaction rates for 4NND than for 5NND, and for a-C700 than for a-C, under the same conditions.

If the initial adsorption rate were exclusively controlled by an electron transfer step, relative adsorption rates would be expected to be comparable to GM model predictions; in fact, the GM model appears to be a good approach for predicting relative charge transfer rates for the $Ru(NH_3)_6^{+3/+2}$ redox couple in solution. Results in Table 3.4 are in qualitative agreement with our observation of faster adsorption rates of 5NND at a-C700 vs. a-C surfaces *in situ* (see Figure 3.6.(b)). However, the observed relative adsorption rates for 5NND at time zero on these two surfaces differ by much less than the 5 orders of magnitude predicted by GM models. Strikingly, the GM model predicts approximately a 20-fold difference for electron transfer from a-C700 to 4NND and 5NND; in contrast, *in situ* adsorption data in Figure 3.5.(b) and *ex situ* chemisorption data in Figure 3.7.(b) show little or no difference between 4NND and 5NND reaction rates at 100% sp^2 amorphous carbons. Finally, *in situ* adsorption data for 4NND at a-C and a-C700 surfaces yields only

very small differences in the rate of adsorption (Figure 3.6.(a)), whereas the GM model estimates a difference of 3 orders of magnitude

The fact that, compared to GM model predictions, smaller or no differences are observed experimentally among adsorption rates might be explained by two possible arguments: (a) differences in adsorption rate at annealed surfaces are below what can be distinguished via our experimental method; (b) the overall aryldiazonium cation adsorption process is controlled by steps that follow the initial electron transfer-mediated adsorption (step 1 in Scheme 3.1.). The first hypothesis appears unlikely, given that the expected differences are extremely large. The second hypothesis appears instead to be likely, based on previous literature on carbon nanotube reactions by Strano and co-workers. Nair *et al.*,[5] in fact, observed a similar effect in the kinetic selectivity of aryldiazonium grafting towards metallic and semiconducting nanotubes; at high aryldiazonium salt concentrations the first adsorption step becomes non-limiting and therefore the reaction rate becomes independent of the carbon substrate electronic properties. In previous work from our group, we found that the early aryldiazonium adsorption curves could be easily modeled using reversible Langmuir adsorption at amorphous carbon surfaces that are poor electron donors (H-doped carbon), however, it was not possible to use the same model for more graphitic surfaces.[29] The current results as well as our previous work therefore suggest that although electron-transfer is important for the first adsorption step, there must exist a threshold rate of electron transfer beyond which adsorption is determined by other processes. For instance, surface diffusion or reorientation of aryldiazonium adsorbates might be necessary in order to chemisorb aryldiazonium adsorbates through nitrogen elimination. Also and importantly, in order for the reaction to proceed and yield a chemisorbed species it is necessary to preserve charge neutrality, as suggested by experimental evidence by Downard and co-workers;[48] reaction of the surface with hole scavengers must therefore occur in parallel to aryldiazonium reduction and can potentially control reaction rates.

3.5. Conclusions

Amorphous carbons offer an interesting opportunity for improving our understanding of reactions at carbon materials since it is possible to modulate their electronic and optical properties to examine their effect on surface chemistry. GM theory has been used in order to interpret experimentally determined charge transfer rates and aryldiazonium cation adsorption results. GM theory was successful at predicting relative charge transfer rates at graphitic amorphous carbon surfaces under the assumptions outlined in the Discussion section: predicted rates were found to be of the same order of magnitude and within 30% of the experimentally determined values. To our knowledge, this is the first example of a successful correlation between valence electronic structure determinations and electrochemical electron transfer rate results at amorphous carbon materials.

The same GM model was applied to spontaneous aryldiazonium cation adsorption; however, it was found that GM predicted much larger differences in adsorption rates than those observed experimentally. This suggests that electron transfer mediated adsorption of aryldiazonium cations at graphitic amorphous carbons is fast to the point that they become not rate-determining, even at early reaction times.

This result has important implications in order to understand (1) the chemistry of amorphous carbon materials and (2) surface functionalization reactions using aryldiazonium salts. A first conclusion is that it appears possible to apply theories of charge transfer that have worked in the past for materials with long range order (e.g. gold, graphene, nanotubes) also to these disordered materials with high density of localized states and defects. A second conclusion is that, although the rate of spontaneous reduction is a good criterion to estimate relative rates of aryldiazonium adsorption at carbons, once the electron transfer rate is sufficiently fast the reaction is controlled by other processes. Although at this stage we can only speculate on the identity of these processes, possible steps could be, for instance, hole scavenging at the carbon or surface reorientation and/or diffusion. Finally and importantly, our results show how a controlled change in carbon composition can be used to gain mechanistic insights on chemical reactions and to develop guiding criteria for achieving selectivity in interfacial reactions.

3.6. References

(1) Paulus, G. L. C.; Wang, Q. H.; Strano, M. S. *Accounts of Chemical Research* **2012**, *46*, 160.

(2) Mahouche-Chergui, S.; Gam-Derouich, S.; Mangeney, C.; Chehimi, M. M. *Chemical Society Reviews* **2011**, *40*, 4143.

(3) Belanger, D.; Pinson, J. *Chemical Society Reviews* **2011**, *40*, 3995.

(4) Barriere, F.; Downard, A. J. *Journal of. Solid State Electrochemistry* **2008**, *12*, 1231.

(5) Nair, N.; Kim, W.-J.; Usrey, M. L.; Strano, M. S. *Journal of the American Chemical Society* **2007**, *129*, 3946.

(6) Sharma, R.; Nair, N.; Strano, M. S. *The Journal of Physical Chemistry C* **2009**, *113*, 14771.

(7) Strano, M. S.; Dyke, C. A.; Usrey, M. L.; Barone, P. W.; Allen, M. J.; Shan, H.; Kittrell, C.; Hauge, R. H.; Tour, J. M.; Smalley, R. E. *Science* **2003**, *301*, 1519.

(8) Usrey, M. L.; Lippmann, E. S.; Strano, M. S. *Journal of the American Chemical Society* **2005**, *127*, 16129.

(9) Baik, S.; Usrey, M.; Rotkina, L.; Strano, M. S. *Journal of Physical Chemistry B* **2004**, *108*, 15560.

(10) Kim, W. J.; Usrey, M. L.; Strano, M. S. *Chemistry of Materials* **2007**, *19*, 1571.

(11) Cullen, R. J.; Jayasundara, D. R.; Soldi, L.; Cheng, J. J.; Dufaure, G.; Colavita, P. E. *Chemistry of Materials* **2012**, *24*, 1031.

(12) Murphy, D. M.; Cullen, R. J.; Jayasundara, D. R.; Scanlan, E. M.; Colavita, P. E. *RSC Advances* **2012**, *2*, 6527.

(13) Wildgoose, G. G.; Wilkins, S. J.; Williams, G. R.; France, R. R.; Carnahan, D. L.; Jiang, L.; Jones, T. G. J.; Compton, R. G. *ChemPhysChem* **2005**, *6*, 352.

(14) Kiema, G. K.; Aktay, M.; McDermott, M. T. *Journal of Electroanalytical Chemistry* **2003**, *540*, 7.

(15) Ferrari, A.; Robertson, J. *Physical Review B* **2000**, *61*, 14095.

(16) Colavita, P. E.; Sun, B.; Tse, K.-Y.; Hamers, R. J. *Journal of the American Chemical Society* **2007**, *129*, 13554.

(17) Ertl, G.; Küppers, J. *Low Energy Electrons and Surface Chemistry*; Wiley-VCH: Weinheim, **1986**.

(18) Schlaf, R.; Schroeder, P. G.; Nelson, M. W.; Parkinson, B. A.; Lee, P. A.; Nebesny, K. W.; Armstrong, N. R. *Journal of Applied Physics* **1999**, *86*, 1499.

(19) Wang, T. M.; Wang, W. J.; Chen, B. L.; Zhang, S. H. *Physical Review B* **1994**, *50*, 5587.

(20) Noguchi, T.; Shimada, T.; Chiba, T.; Terada, M.; Hasegawa, T. *Diamond and Related Materials* **2010**, *19*, 107.

(21) Fanchini, G.; Tagliaferro, A. *Diamond and Related Materials* **2001**, *10*, 191.

(22) Foulani, A. *Journal of Physics D: Applied Physics* **2003**, *36*, 394.

(23) Robertson, J. *Materials Science and Engineering: R: Reports* **2002**, *37*, 129.

(24) Sun, B.; Colavita, P. E.; Kim, H.; Lockett, M.; Marcus, M. S.; Smith, L. M.; Hamers, R. J. *Langmuir* **2006**, *22*, 9598.

(25) Fendrych, F.; Pajasova, L.; Wagner, T.; Jastrabik, L.; Chvostova, D.; Soukup, L.; Rusnak, K. *Diamond and Related Materials* **1999**, *8*, 1711.

(26) Faizrakhmanov, I.; Bazarov, V.; Stepanov, A.; Khaibullin, I. *Semiconductors* **2003**, *37*, 723.

(27) Haerle, R.; Riedo, E.; Pasquarello, A.; Baldereschi, A. *Physical Review B* **2001**, *65*, 045101.

(28) Jackson, S. T.; Nuzzo, R. G. *Applied Surface Science* **1995**, *90*, 195.

(29) Jayasundara, D.; Cullen, R. J.; Colavita, P. E. *Chemistry of Materials* **2013**, *25*, 1144.

(30) Hallmark, V. M.; Chiang, S.; Brown, J. K.; Wöll, C. *Physical Review Letters* **1991**, *66*, 48.

(31) Reinke, P.; Francz, G.; Oelhafen, P.; Ullmann, J. *Physical Review B* **1996**, *54*, 7067.

(32) Schelz, S.; Richmond, T.; Kania, P.; Oelhafen, P.; Guntherodt, H. J. *Surface Science* **1996**, *359*, 227.

(33) McFeely, F. R.; Kowalczyk, S. P.; Ley, L.; Cavell, R. G.; Pollak, R. A.; Shirley, D. A. *Physical Review B* **1974**, *9*, 5268.

(34) Kelemen, S. R.; Freund, H.; Mims, C. A. *Journal of Catalysis* **1986**, *97*, 228.

(35) Bard, A. J.; Faulkner, L. R. *Electrochemical Methods: Fundamentals and Applications*; 2nd ed.; John Wiley & Sons, Inc.: New York, **2001**.

(36) Fairman, C.; Yu, S. C.; Liu, G.; Downard, A.; Hibbert, D. B.; Gooding, J. J. *Journal of Solid State Electrochemistry* **2008**, *12*, 1357.

(37) Ranganathan, S.; Steidel, I.; Anariba, F.; McCreery, R. L. *Nano Letters* **2001**, *1*, 491.

(38) McCreery, R. L. *Chemical Reviews*, **2008**, *108*, 2646-2687.

(39) Nissim, R.; Batchelor-McAuley, C.; Henstridge, M. C.; Compton, R. G. *Chemical Communications* **2012**, *48*, 3294.

(40) Heller, I.; Kong, J.; Williams, K. A.; Dekker, C.; Lemay, S. G. *Journal of the American Chemical Society* **2006**, *128*, 7353.

(41) Szroeder, P.; Tsierkezos, N. G.; Scharff, P.; Ritter, U. *Carbon* **2010**, *48*, 4489.

(42) Szroeder, P. *Physica E: Low-dimensional Systems and Nanostructures* **2011**, *44*, 470.

(43) Schäfer, J.; Ristein, J.; Graupner, R.; Ley, L.; Stephan, U.; Frauenheim, T.; Veerasamy, V. S.; Amaratunga, G. A. J.; Weiler, M.; Ehrhardt, H. *Physical Review B* **1996**, *53*, 7762.

(44) Miyajima, Y.; Tison, Y.; Giusca, C. E.; Stolojan, V.; Watanabe, H.; Habuchi, H.; Henley, S. J.; Shannon, J. M.; Silva, S. R. P. *Carbon* **2011**, *49*, 5229.

(45) Trasatti, S. *Journal of Electroanalytical Chemistry* **1974**, *52*, 313.

(46) Ilie, A.; Hart, A.; Flewitt, A. J.; Robertson, J.; Milne, W. I. *Journal of Applied Physics* **2000**, *88*, 6002.

(47) Smalley, J. F.; Finklea, H. O.; Chidsey, C. E. D.; Linford, M. R.; Creager, S. E.; Ferraris, J. P.; Chalfant, K.; Zawodzinsk, T.; Feldberg, S. W.; Newton, M. D. *Journal of the American Chemical Society* **2003**, *125*, 2004.

(48) Lehr, J.; Williamson, B. E.; Downard, A. J. *Journal of Physical Chemistry C* **2011**, *115*, 6629.

4. Photochemical investigations of nPAHs at amorphous carbon surfaces

---

Investigating the photochemical behaviour of nPAHs is important as photodegradation is thought to be the dominant daytime decay pathway for these molecules. When it comes to the degradation of nPAHs, one reaction which is known to occur is their heterogenous reactions on soot particles, which make up a major percentage of particulate matter in the atmosphere. The photodegradation of nPAHs on carbon/nPAH interfaces was investigated as a model for the reactions that occur on soot particles.

4.1. Introduction

A known degradation pathway for nPAHs in the atmosphere is their heterogeneous reactions on soot particles.[1] Soot particles consist of elemental and organic carbon and make up a major percentage of particulate matter in the atmosphere. Surface mediated reactions which occur on soot particles can have huge environmental effects such as affecting the distribution and residence time of particulate matter in the atmosphere and thereby determining their impact on human health.[1-3] Therefore understanding heterogeneous chemical reactions on these carbonaceous particles is imperative for improving atmospheric models and assessing impacts on the environment, climate and public health. Photodegradation is thought to be the dominant daytime loss pathway for nPAHs in the atmosphere, consequently, in this work the photodegradation of nPAHs on carbon/nPAH interfaces was investigated as a model for the reactions that occur on soot particles.

The mechanism for the photodegradation process for nPAHs has been discussed in the introduction chapter and is proposed to occur via a nitro to nitrite rearrangement, as put forward by Chapman.[4] The reaction proceeds via a rearrangement from the nitroarene to the corresponding arylnitrite with subsequent elimination of NO and the formation of a reactive phenoxy radical as depicted in Scheme 4.1. Subsequent reactions of the radical lead to the formation of oxidized species. The overall reaction results in the elimination of nitro moieties and rearrangement to oxidized species such as carbonyls. The elimination of nitro groups is important from an environmental perspective as this rearrangement reduces the toxicity of the molecule.

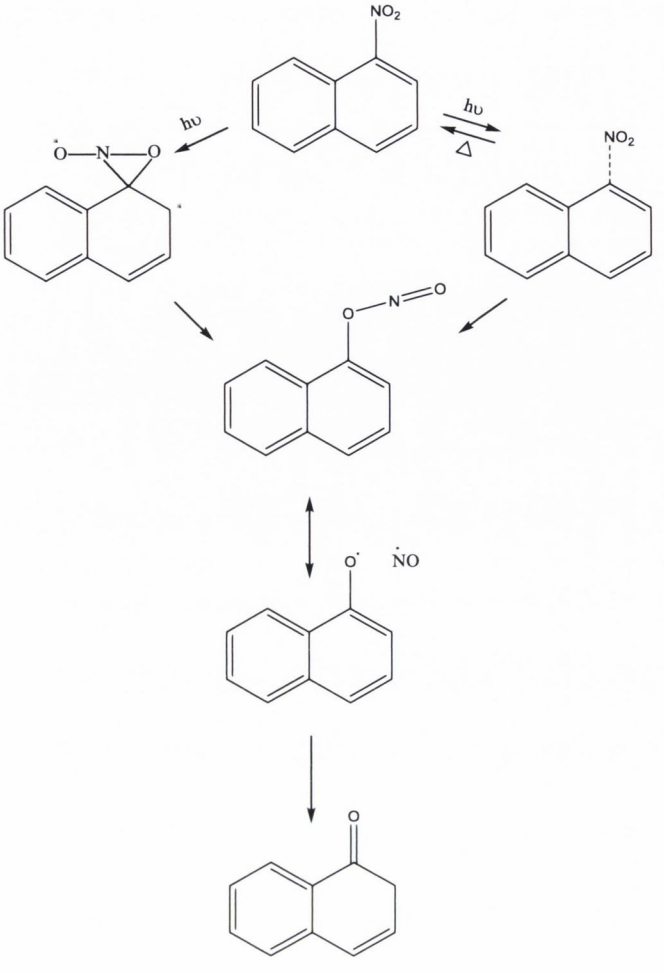

Scheme 4.1. Proposed mechanism for the photodegradation of 1-nitronaphthalene.

The photochemical reactions of particle associated nitroarenes have been discussed previously in the literature and have also been dealt with, in great detail, in the introduction chapter.[1] However, a major gap in atmospheric chemistry knowledge still exists with regards the mechanisms, rates, structures and fates of nPAHs as they degrade in the polluted atmosphere. For surface associated nPAHs, this is largely due to the complexity of the surface on which the photodegradation occurs.[1] For carbonaceous materials it has been suggested that carbon content is one of the main factors determining the photostability of absorbed nPAHs.[1,5]

Therefore, we aimed to investigate the effect carbon content had on the photodegradation rate of nPAHs. In order to achieve this, carbon substrates with well-characterized structure and composition were prepared and utilized as model surfaces for carbonaceous soot particles found in the atmosphere. Diazonium chemistry was employed for the modification

of surfaces with nPAH compounds, to attain model interfaces that retain selected aspects of naturally occurring carbon/nPAH interfaces. Surfaces were modified with 4-nitrobenzene diazonium tetrafluoroborate (4NBD) and 4-nitronaphthalene diazonium tetrafluoroborate (4NND), the structures of which are shown in Scheme 4.2.

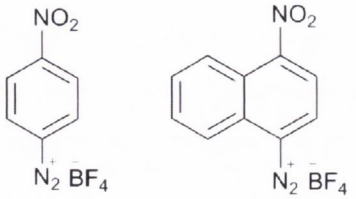

Scheme 4.2. Structures of 4-nitrobenzene diazonium tetrafluoroborate (4NBD) and 4-nitronaphthalene diazonium tetrafluoroborate (4NND).

Photodegradation measurements were taken under normal conditions of temperature, humidity and oxygen content as these conditions are most relevant for transformations in the troposphere. Photodegradation at carbon surfaces was studied using infrared spectroscopy. nPAHs have strong signatures in the infrared region enabling chemical transformations at the model carbon surface to be monitored. Infrared reflection absorption spectroscopy (IRRAS) has been utilized previously for the characterization of functionalized thin films of amorphous carbons.[6-8] In this work, photodecomposition was investigated using IRRAS to monitor the disappearance of the strong NO_2 stretching peaks as a function of time. Oxidised aromatics are the expected reaction products and can also be identified using IRRAS spectroscopy. IRRAS provides a useful platform for investigating changes at the carbon interface as this technique operates over a short time scale and is ideal for measuring the degradation of 2-3 ring nPAHs, as these have typical half-lives of less than 6 h.[6,9-10]

Measurements of photodegradation of nPAHs in solution were also taken, in order to compare to the results we obtained at carbon surfaces. This work was carried out by my colleague Dr. Paraic Keane. The compounds chosen for solution photolysis experiments were 1-nitronapthalene (1NN) and nitrobenzene (NB), the structures of which are given in Scheme 4.3. The low solubility of 1NN in water (<0.3 mM) precluded the use of IR

techniques for these experiments, so the spectral changes on photo-irradiation were monitored using UV–Vis spectroscopy.

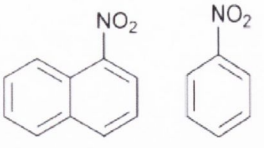

Scheme 4.3. Structures of 1-nitronaphthalene (1NN) and nitrobenzene (NB).

Overall, this project aimed to gather information from experimental investigation which would add to the compiled knowledge on the subject of photodegradation of nPAHs. Little is known about the photostability of nPAHs on atmospheric aerosols and further knowledge will greatly benefit understanding of the chemistry of polluted atmospheres.[5] The work herein offers an original contribution aiding the understanding of reactions on carbonaceous aerosols. Thus far, the limited work on soot simulants has been carried out on candle or toluene soot, substances that display uncontrollable chemical heterogeneity and therefore, a mixed range of electronic properties.[11-12] Amorphous carbons enable the synthesis of carbon materials with controlled electronic and chemical properties as has been shown in Chapter 3. These surfaces are amenable to careful characterization and can be reproducibly synthesized under controlled conditions. Literature publications indicate that nobody has taken advantage of these materials for the improvement of understanding of environmental reactions. In this chapter we report on our efforts to achieve this.

4.2. Experimental

4.2.1. Chemicals and materials

4-Nitrobenzene diazonium tetrafluoroborate (4NBD, 97%) hydrogen peroxide (H_2O_2, 30%), sulfuric acid (95-97%) and 1-nitronaphthalene (1NN, 99%) were all obtained from Sigma and used as received. Nitrobenzene (NB, 99%) was obtained from Fluka and was also used as received. 4-Nitronaphthalene diazonium tetrafluoroborate (4NND) was synthesized as described in the previous chapters and in the literature.[13] Deionized water was used for all aqueous solutions.

4.2.2. Sample preparation

As described in the two previous chapters, amorphous carbon substrates were prepared via DC magnetron sputtering at a base pressure $\leq 2 \times 10^{-6}$ mbar and a deposition pressure of 7×10^{-3} mbar.[8,13] Substrates consisted of a 70 nm carbon layer with a 300 nm thick titanium underlayer to enhance the reflectance of the sample.[7,14] The amorphous carbon substrates discussed thus far, have been sputtered in an Ar amosphere, are referred to as a-C and are deposited in the same fashion as in Chapters 2 and 3. Hydrogen-doped amorphous carbon films were also prepared for this work via introduction of H_2 during deposition at a concentration of 10%. This hydrogen doped amorphous carbon will be referred to as a-C:H. Structural characterization of these films has been reported in the literature and shows that introduction of hydrogen into the films at this concentration decreased the sp^2 content from approximately 80% for a-C substrates to approximately 17% sp^2 for a-CH substrates.[8] Sputter-coating was performed on silicon for infrared measurements, which were cleaned prior to deposition via immersion in piranha (3:1, H_2SO_4 to H_2O_2), followed by rinsing in DI H_2O and drying using Ar flow. Following deposition of carbon films, surfaces were functionalized via immersion in 1×10^{-4} M aqueous solutions of aryldiazonium salts to form 4-nitrobenzene (4NB) and 4-nitronaphthalene (4NN) adlayers. Modification times were varied for each surface to attain a surface coverage of $\sim 6 \times 10^{-10}$ mol cm^{-2}. For the photochemical analysis of solutions, 2.6×10^{-5} M and 1.7×10^{-4} M aqueous solutions of 1NN and NB were prepared, respectively.

4.2.3. Photodegradation setup

The irradiation setup which was utilized for both surface and solution photochemical experiments consisted of a 300 W Xe Arc lamp power supply (LOT Oriel) in a lamp housing. The irradiation was collimated through a long pass filter wheel (LOT Oriel) and quartz window into the reaction cell which had a removable sample compartment. A schematic of the photodegradation setup is given in Figure 4.1. The power of the lamp was also monitored at regular intervals using a Thorlabs S302C Thermal Power Sensor, and was found to remain relatively stable over time (2-3% deviation). The specifications of the filters utilized in this set-up, together with the total power measured at the sample position for each filter, are given in Table 4.1. It is important to note that illumination through filter

2 is most likely the best approximation of the ozone filtered spectrum of the troposphere. The measurements described herein were taken at ambient temperature, pressure, and humidity. The humidity remained in the range 42 - 46 % during the course of the experiments. Sample temperature was monitored during irradiation and no increase in temperature at the sample surface was observed.

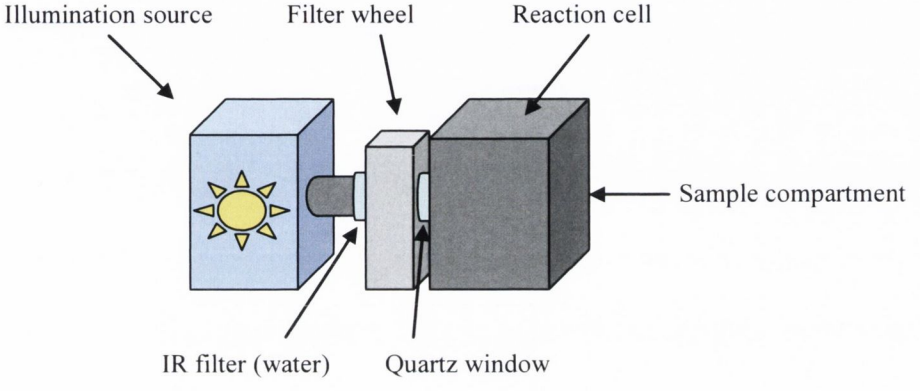

Figure 4.1. Photodegradation experimental set-up.

Table 4.1. Filter specifications and total power measured at the sample position.

Filter No.	Wavelength range (nm)	Wavelength at 50% T	Power (mW cm^{-2})
1	>200	-	53.5
2	>350	280	48.2
3	>440	360	47.3

4.2.4. Characterization Methods

Surface and solution measurements were taken using IRRAS and UV–Vis absorbance techniques respectively, following irradiation of samples using the experimental set-up described in Section 4.2.3. IRRAS was carried out on a Bruker Tensor 27 Fourier transform infrared (FTIR) spectrometer, equipped with a mercury-cadmium-telluride (MCT) detector, using a VeeMaxII variable angle specular reflectance accessory with wire grid polarizer. All IRRAS measurements were obtained using p-polarized light at an 80° angle of incidence from the surface normal. 256 scans with a resolution of 4 cm^{-1} were collected for each sample and a bare carbon substrate was used as a background. Irradiation of solution

samples was performed in a quartz cuvette with 1 cm pathlength. UV–Vis spectra were recorded on a Cary 50 Scan spectrophotometer with 1 nm resolution; spectra were collected against a water baseline in the range 200-700 nm at regular time intervals. When not under illumination or being characterized, samples were kept in the dark.

4.3. Results

4.3.1. UV-Vis absorption spectra of parent molecules

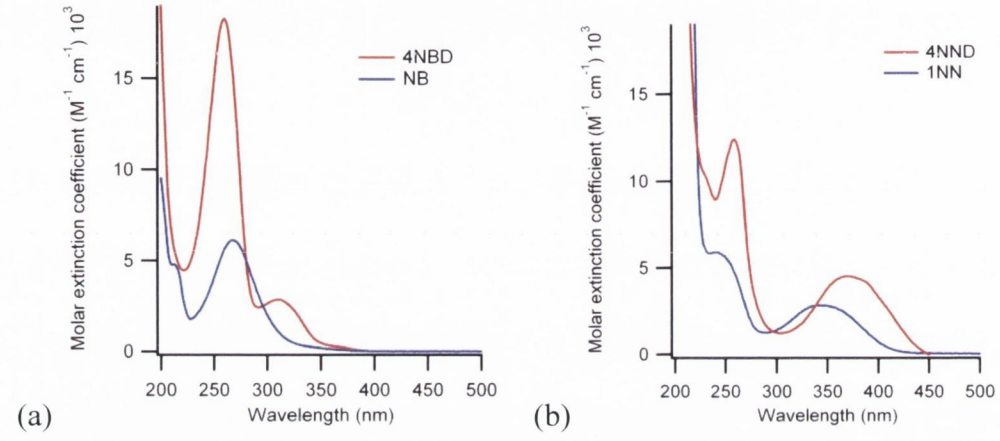

Figure 4.2. UV–Vis spectra of (a) nitrobenzene and 4-nitrobenzene diazonium and (b) nitronaphthalene and 4-nitronaphthalene diazonium in aqueous solution.

Figure 4.2.(a) and (b) show plots of molar extinction coefficient versus wavelength for the diazonium salts used for surface modifications and the nitro aryl molecules used for solution analysis. There are similarities between the absorption spectra of the nitroaryl compounds and their corresponding diazoniated analogues in solution. The band at ~260 nm is characteristic of the nitrobenezene chromophore and is found in nearly all nitroaromatics.[15] It has been assigned as an intramolecular transfer band from the benzene ring towards the NO_2 group. The bands occurring at higher wavelengths for 4NND and 1NN are associated with extended aromatic systems. All of the peaks shown are attributed to $\pi - \pi^*$ transitions.[16] It can be observed that the molecules with an additional aromatic ring (4NND and 1NN) have greater absorptions in the 300 – 400 nm region.

4.3.2. Photodegradation of 4NB at a-C surfaces

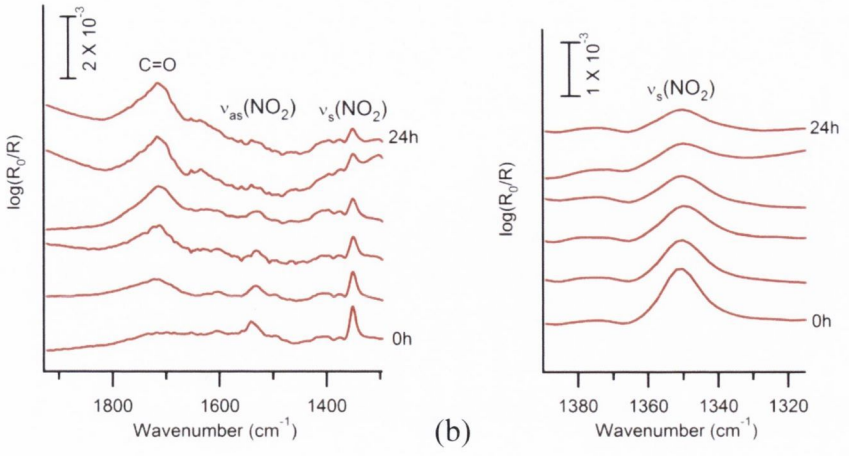

Figure 4.3. (a) Raw IRRAS spectra of 4NB on a-C irradiated with filter at position 1 over 24 h. Spectra have been offset for clarity. (b) Close up of the nitro symmetric stretching peak region.

Figure 4.3.(a) shows the raw IRRAS spectra of a-C substrates modified using 4NBD to a surface coverage of 6.0×10^{-10} mol cm^{-2} and subsequently irradiated using the photochemical setup described in Section 4.2.3. Measurements were taken at regular time intervals and revealed that irradiation of the surface-bound nitrophenyl compound resulted in reductions in the symmetric and asymmetric nitro associated peaks occurring at ~1350 cm^{-1} and ~1530 cm^{-1} respectively.[17] (Over time, a peak emerged at 1715 cm^{-1} which we attribute to a carbonyl stretching mode. Figure 4.3.(b) shows an enlargement of the nitro symmetric stretching peak region for this dataset, which shows an overall reduction of 60% over 24h.

These results demonstrated that the photochemical degradation of surface bound nitroaryl groups could be measured with satisfactory time resolution. The photodegradation of 4NB at a-C surfaces was measured in the photochemical set up using light over different wavelength ranges by varying the filter used. From the raw IRRAS data, the percentage change in the net absorbance of the symmetric nitro stretching peak was calculated and plotted as a function of irradiation time. This is illustrated in Figure 4.4. which shows the percentage change in the symmetric nitro stretching peak for 4NB at a-C surfaces measured using IRRAS over 24h using filters No. one, two and three which correspond to

wavelengths of greater than 200 nm, 350 nm and 440 nm, respectively. These measurements were carried out in triplicate and average values and errors calculated.

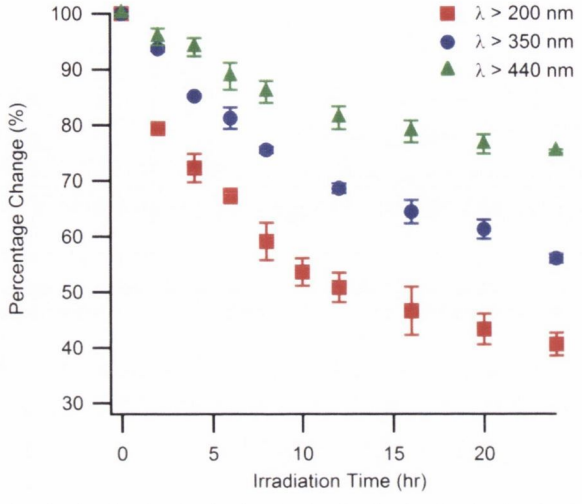

Figure 4.4. Percentage change in symmetric nitro peak over time for 4NB on a-C.

From these results, it can be concluded that as the wavelength range shifts to higher values, the total percentage change in the symmetric nitro peak decreases, over 24 h, from 60% for filter one ($\lambda > 200$ nm), to 44% and 25% for filter two ($\lambda > 350$ nm) and three ($\lambda > 440$ nm), respectively. The data in Figure 4.4, suggests that the net absorbance of the symmetric nitro peak decays exponentially as a function of irradiation time.

Figure 4.5. shows logarithmic plots of the data in Figure 4.3. prepared in an analogous manner as in Chapter 2. The linear trends observed suggest that a 1st order decay can be used to approximate satisfactorily the experimental results.

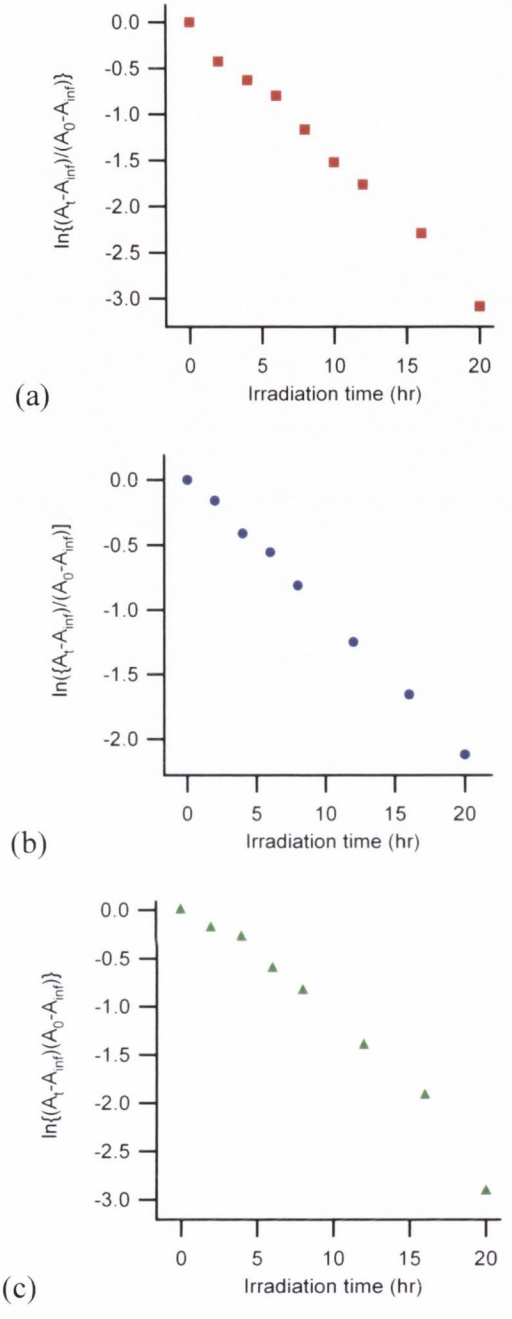

Figure 4.5. Logarithmic plots of the symmetric nitro peak decay at (a)Filter position one ((λ > 200 nm, (b)Filter position two (λ > 350 nm) and (c)Filter position three (λ > 440 nm).

An exponential function:

$$f(t) = (100 - A) + A_0 e^{-kt} \qquad \text{(Eqn 4.1.)}$$

Where k is the observed rate coefficient and A is an amplitude constant, offered an excellent fit of the decay data in Figure 4.4. Figure 4.6. shows data plots and their corresponding weighted exponential fits. The first order rate constant, k (h^{-1}) and the limiting value at

$t \rightarrow \infty$, $f(t \rightarrow \infty)$ are shown in Table 4.2. Also in Table 4.2, are reported the reaction rates at $t = 0$ for all three data sets, which were calculated as a straight line fit of the data for $t < 4$ h.

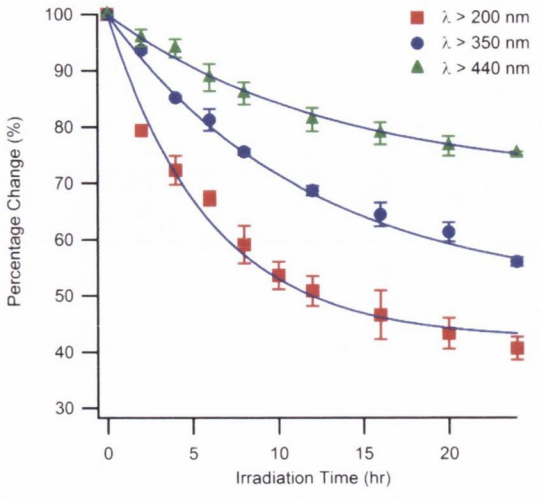

Figure 4.6. Percentage change in the symmetric nitro peak for 4NBD modified a-C surfaces measured over 24 h using λ > 200, λ > 350 and λ > 440 with weighted exponential fitting of the decay.

Table 4.2. First order rate constant, limiting value at t→∞, and initial rate decay of 4NB at a-C surfaces.

	k (h^{-1})	f(t→∞)	Rate @ t=0 (h^{-1})
Filter 1 (λ > 200)	0.168 ± 0.012	42 ± 2	6.9 ± 2.0
Filter 2 (λ > 350)	0.084 ± 0.004	50 ± 1	3.7 ± 0.3
Filter 3 (λ > 440)	0.076 ± 0.015	70 ± 2	1.5 ± 0.3

It is significant to note that shorter wavelengths appeared to have an important impact on the decay of the nitro moiety. This is apparent from the large difference in rate constants between filter one and filter two and three. The first order rate constant for filter one is double the value obtained for filter two, while the values calculated for filters two and three are relatively similar. The initial rates of decay measured at t=0 showed that the rate at filter one is approximately double that of filter two, which, in turn, is double that of filter three.

The decrease in the symmetric nitro stretching peak in Figure 4.3. is accompanied by an increase in the absorbance of a carbonyl peak at ~1715 cm^{-1}. Figure 4.7. shows a plot of the time evolution of the two peaks during irradiation.

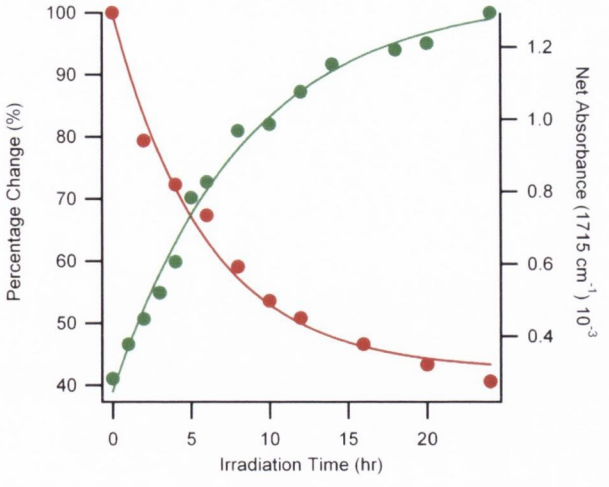

Figure 4.7. Plot of decrease of nitro symmetric peak (●) and emergence of CO peak (●) for 4NB surfaces with irradiation at $\lambda > 200$ nm (filter one). Lines show fitting with exponential functions.

The net absorbance of the carbonyl peak also displayed an exponential behaviour as a function of time. A fit of the carbonyl net absorbance plots with an exponential function yielded a rate constant of 0.118 ± 0.012, which is somewhat smaller than that observed for the disappearance of the nitro group (95% C.I.). This suggests that oxidized species are being formed during the photodegradation of the surface-bound aryl nitro groups.

In summary, the experiments carried out using 4-nitrobenzene molecules showed that (1) It is possible to follow photochemical degradation of surface-bound nitroaryl groups with satisfactory time resolution. (2) That the photodegradation of the surface-bound nitro groups occurs in parallel with an oxidation process and (3) Wavelengths above 440 nm have a much smaller impact on the decay of the nitrobenzene group compared to wavelengths in the range 200-440 nm.

4.3.3. Photodegradation of 4NN at a-C surfaces

The photodegradation of nPAHs was probed by monitoring the IRRAS spectra of 4NND modified a-C samples with increasing irradiation time. Figure 4.8. shows the raw IRRAS spectra of a-C substrates modified using 4NND to a surface coverage of 6.0×10^{-10} mol cm^{-2} following increasing irradiation time. Similar to the 4NB results mentioned in the

previous section, a decrease in the peaks associated with nitro stretching and an increase in the carbonyl peak are observed with increasing irradiation time.

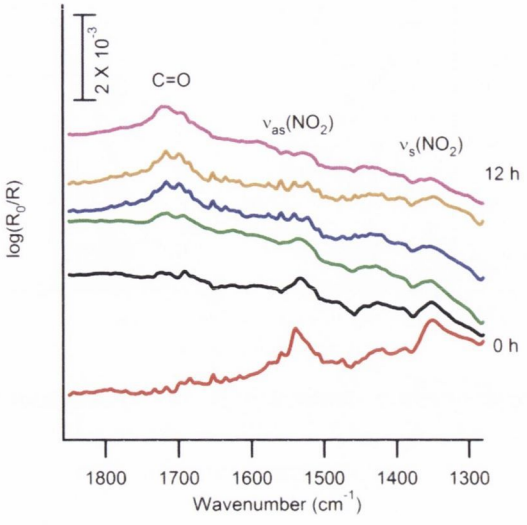

Figure 4.8. Raw IRRAS spectra of 4NN at a-C with irradiation at λ > 200 nm (filter one).

The percentage change in the net absorbance of the symmetric nitro stretching peak was plotted as a function of irradiation time from the raw IRRAS data. This is illustrated in Figure 4.9. which shows the percentage change for 4NND modified surfaces measured over 12 h using filters No. one (λ > 200 nm), two (λ > 350 nm) and three (λ > 440 nm). Measurements for times longer than 12 h were not possible because the IRRAS intensity of the nitro peak falls below the noise threshold. The nitro peak intensity of 4NN falls rapidly to 80% in only 12 h through filter one (λ > 200 nm). The decay of 4NN is much faster than that observed under the same conditions for 4NB; this can be seen in Figure 4.10. which shows a comparison of decay curves obtained for λ > 200 (filter one) for the two nitroaryl adlayers.

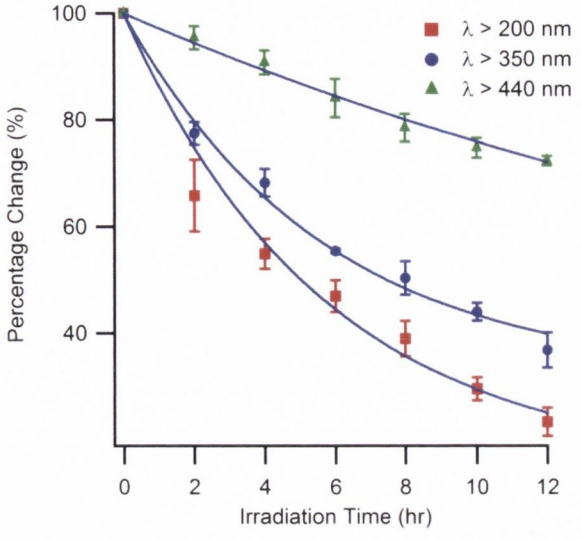

Figure 4.9. Percentage change in symmetric nitro peak for 4NND modified a-C surfaces measured over 12 h using λ > 200, λ > 350 and λ > 440 with weighted exponential fitting of the decay.

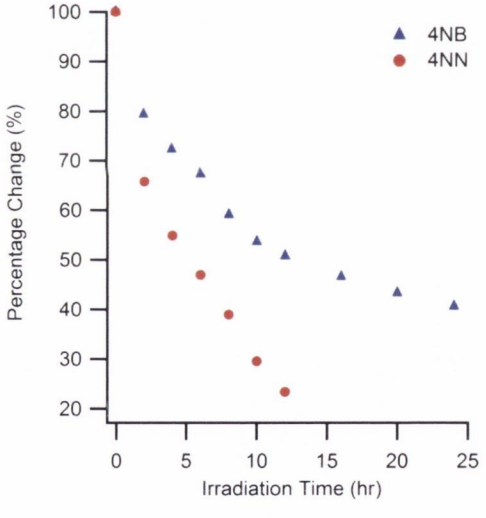

Figure 4.10. Comparison of 4NB and 4NN decay curves through filter one (λ > 200 nm).

Table 4.3. First order rate constant, limiting value at t→∞ and initial rate decay of 4NN at a-C surfaces.

	k (h^{-1})	f(t→∞)	Rate @ t=0 (h^{-1})
Filter 1 (λ > 200 nm)	0.18 ± 0.03	15 ± 6	11.3 ± 3.4
Filter 2 (λ > 350 nm)	0.18 ± 0.02	32 ± 4	7.9 ± 1.9
Filter 3 (λ > 440 nm)	0.05 ± 0.05	35 ± 1	2.3 ± 0.1

In a similar manner to that described in the previous section, the first order rate constants and the limiting values at $t \rightarrow \infty$ were calculated using the standard deviation for weighted exponential fits using equation 4.1. The first order rate constants, limiting values at $t \rightarrow \infty$ and initial rates of decay of 4NN at a-C surfaces were calculated and are presented in Table 4.3.

Figure 4.9. indicates that, although the shortest wavelengths (filter one, $\lambda > 200$ nm) still yield the fastest decay rate, longer wavelengths are more important for the decay of 4NN than for the decay of 4NB. A similar decay over at wavelengths greater than 200 nm and 350 nm are observed for 4NN modified surfaces during irradiation is confirmed in Table 4.3., where it is observed that the rate constant values do not vary hugely by changing the from filter position one to filter position two. A large decrease in rate is noted following irradiation at wavelengths greater than 440 nm. By examining Figure 4.10. and the values in Tables 4.2. and 4.3., it can be confirmed that 4NN decays at a faster rate than 4NB.

From the raw IRRAS data, it can be observed that the decrease in the symmetric nitro stretching peak for 4NN on a-C is accompanied by an increase in the absorbance of a carbonyl peak at ~1715 cm^{-1}. Figure 4.11. shows the time evolution of the two peaks during irradiation.

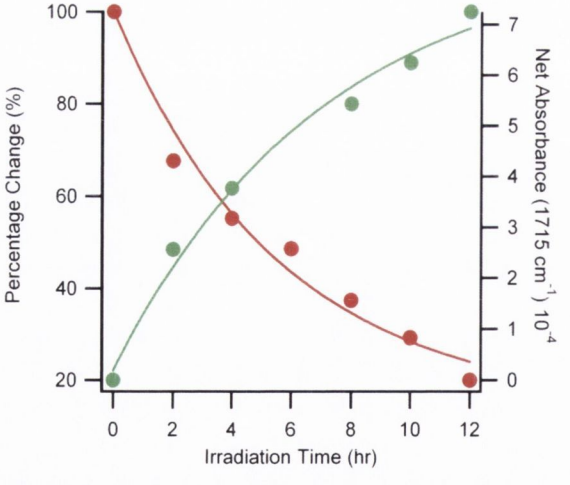

Figure 4.11. Plot of decrease of nitro symmetric peak (●) and emergence of CO peak (●) for 4NND modified surfaces with irradiation at $\lambda > 200$ nm (filter one). Lines show fitting with exponential functions.

Similar to the photodegradation of 4NB on a-C, the net absorbance of the carbonyl peak displayed an exponential behaviour as a function of time. A fit of the carbonyl net

absorbance plots with an exponential function yielded a rate constant of 0.14 ± 0.04 h^{-1}, which is similar to that observed for the disappearance of the nitro group which had a rate constant value of 0.18 ± 0.03 h^{-1}.

From these results it can be deduced that at a-C surfaces 4NN has a shorter lifetime than 4NB when under irradiation using our photodegradation set-up. It has previously been observed in the literature, that photodegradation rate is not solely dependant on the ring size of the PAC.[10] It can also be stated that photodegradation at 4NND modified surfaces results in a much greater overall reduction in the nitro group. This is realized when we compare the limiting value at $t \rightarrow \infty$ for 4NN and 4NB which are 15% ± 6% and 42% ± 2%, respectively. The 4NN initial decay rates do not drop as drastically as those calculated for 4NB when changing the wavelength range used in our experiments (from $\lambda > 200$ nm to $\lambda >$ 350 nm); this could possibly be attributed to differences in the absorption spectra of the two molecules and will be discussed further in later sections. Finally, the photodegradation of 4NN surface-bound nitro groups results in an oxidation process at the surface.

4.3.4. Photodegradation of 4NND at a-C:H surfaces

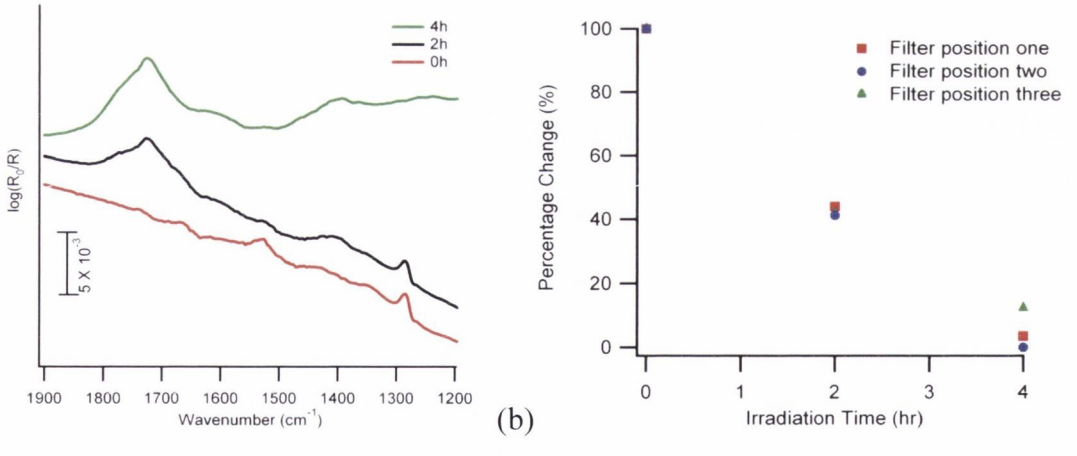

Figure 4.12.(a). Raw IRRAS spectra of 4NN on a-C:H irradiated using filter one over 4 h and (b) percentage change in symmetric nitro peak over time for 4NND modified a-C:H.

To further probe the photodegradation of nPAHs at amorphous carbon surfaces, measurements were taken at a-C:H substrates. It was found that the photochemical induced transformations occurred readily at the a-C:H surface, with an almost complete

disappearance of the symmetric nitro peak in 4 h using filter one. Figure 4.12.(a) displays the IRRAS spectra of 4NND modified a-C:H substrates following irradiation for increasing times through filter one. Similar to the IRRAS data already shown in previous sections, a decrease in the peaks associated with nitro groups and the emergence of a peak in the carbonyl stretching area are observed. Figure 4.12.(b) displays the percentage change in the symmetric nitro stretching peak for 4NND at a-C:H surfaces measured using IRRAS over 4 h using filter position one, two and three. The initial rates at t=0 were calculated as 24.1 ± 2.2, 25.0 ± 2.5 and 21.9 ± 4.1 % loss h^{-1} for filters one, two and three, respectively. The data could not be fit satisfactorily with an exponential function, so first order rate constants were not calculated. It is apparent from Figure 4.12.(a) and (b) that almost complete photodegradation of nitro groups at hydrogen doped amorphous carbon surfaces occurred within 4 h. To ensure that the rapid loss is not due to desorption of physisorbed 4NN groups at the a-C:H surface, we plan on carrying out X-ray photoelectron spectroscopy (XPS) measurements of the initial 4NN adlayer.

4.3.5. Photodegradation of nPAH in solution

The photodegradation of mono and polycyclic nitro compounds in aqueous solution was also investigated using the described photochemical setup in collaboration with Dr. Paraic Keane. Monitoring of the photolysis of nitrobenzene (NB) and 1-nitronaphthalene (1NN) in aqueous solutions was carried out using UV–Vis absorption spectrophotometry.

Figure 4.13. shows the UV–Vis spectra for 1NN with increasing irradiation over 18 h through filter position 1. The decrease in the peak associated with $\pi - \pi^*$ transition at 213 nm was monitored as a function of time; a percentage change was calculated and fit to an exponential function, which is illustrated in Figure 4.14. Data manipulation was carried out for 1NN data across using all of the optical filters in Table 4.1. and the results are reported in Table 4.4. From this data, the photodegradation quantum yield of 1NN in aqueous solution was calculated to be $1.1 \pm 0.4 \times 10^{-3}$, which is in line with the literature reports for the photodegradation of 1NN in acetonitrile.[18]

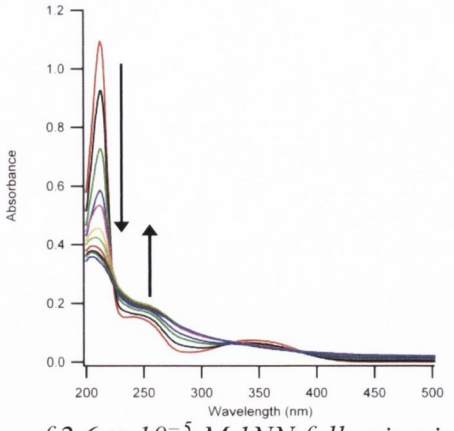

Figure 4.13. UV–Vis spectra of 2.6 × 10^{-5} M 1NN following irradiation at λ > 200 nm over 18 h.

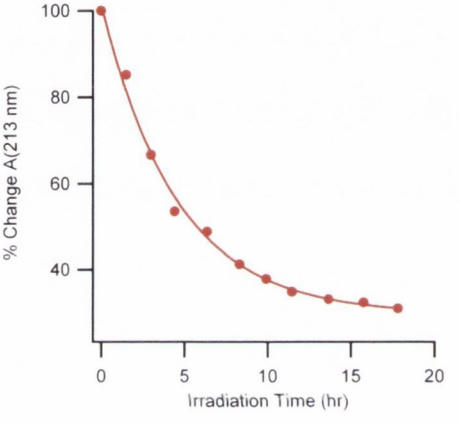

Figure 4.14. Plot of percentage change of absorbance at 213 nm of 2.6 × 10^{-5} M 1NN following irradiation at λ > 200 nm over 18 h.

Table 4.4. First order rate constant, limiting value at t→∞ and initial rate decay of 1NN in aqueous solution.

	k (hr^{-1})	**f(t→∞)**	**Rate @ t=0 (hr^{-1})**
Filter 1 (λ > 200 nm)	0.219 ± 0.016	27.9 ± 1.9	10.7 ± 0.4
Filter 2 (λ > 350 nm)	0.186 ± 0.011	25.6 ± 1.7	9.2 ± 0.1
Filter 3 (λ > 440 nm)	0.134 ± 0.013	32.4 ± 2.3	6.9 ± 0.2

4.4. Discussion and Conclusions

The photodegradation of nPAHs at surfaces is proposed to occur via the Chapman rearrangement, as discussed previously.[1,5] Degradation via this pathway results in the loss of nitro groups and the appearance of oxidised species. The observations from the work presented herein, on the photodegradation of surface-bound nitroaryl molecules at amorphous carbons are consistent with the mechanism, as described in Scheme 4.1. Our results indicate that nitroaryl compounds decompose through the loss of the nitro group, which occurs in parallel with an oxidation process.

It is possible that the observed oxidation process could be (1) unrelated to the nitro reduction or (2) a product of the nitro degradation. We propose the oxidation process is a product of the degradation due to observations in the carbonyl region of IRRAS spectra. We have assigned the oxidation process to the appearance of carbonyl peaks at ~ 1715 cm^{-1} and calculated rate constants for carbonyl appearance and nitro disappearance for the photodegradation of 4NBD and 4NND modified surfaces. The rate constants were not equal but were of a similar magnitude, with the carbonyl formation rate slower than the nitro degradation. Possible explanations for the difference in rate constant values could be (1) that other oxidised products were also formed simultaneously, which are not present at the wavenumber monitored or (2) that measurement of net absorbance at one wavenumber is not fully indicative of the oxidative processes occurring. To investigate the second possibility, decay curves and rate constants were calculated using peak areas of the symmetric nitro and carbonyl regions. It was found that this introduced significant deviations into the resultant curves which rendered them indistinguishable from each other. This clarifies that our method of measurement of photodegradation using peak heights is suitable. We believe that the observed oxidation process is a product of the nitro degradation, and not a parallel oxidation. However, to verify this conclusively, XPS analysis of carbon samples before and after irradiation is required and is part of the future work for this project. From the work carried out in this chapter, it can be concluded that the photochemical degradation of surface-bound nitroaryl groups can be monitored with satisfactory time resolution.

For the photodegradation of nitroaryl groups at a-C surfaces, similar first order rate constants of ~ 0.17 – 0.18 h^{-1} were measured for 4NBD and 4NND modified surfaces when irradiating at the full range of wavelengths. However, when the wavelength range was narrowed, the rates constants for 4NBD surfaces decreased drastically whereas the rate constants for 4NND surfaces remained relatively constant. We believe that this can be explained by differences in the absorption spectra of the two molecules.

In solution, 4NND has greater absorptions in the wavelength region 300 – 400 nm, as can be seen in Figure 4.2., which displays the molar extinction coefficient versus wavelength plots for 4NBD and 4NND. It can be observed that, relative to 4NND, 4NBD absorbs very little in this region. Assuming that also when attached to the surface, 4NN moieties have greater absorption cross sections than 4NB moieties in the 300 – 400 nm region, we can attribute the higher rate constants in this region for 4NN to the greater ability of 4NN moieties to absorb radiation.

Overall, the initial rates of photodegradation (Rate @ t=0) measured at a-C surfaces were quicker for 4NND modified surfaces than for 4NBD modified surfaces, as shown in Tables 4.2. and 4.3. The initial rates calculated for 4NND did not drop as drastically as those calculated for 4NBD when the filter was changed; again we attribute this to differences in the absorption spectra of the molecules as discussed in the previous paragraph.

Photodegradation of 4NND at a-C surfaces occurred over a shorter timescale than 4NBD as observed in Figure 4.10., furthermore, it can also be concluded from our results that photodegradation at 4NND modified surfaces results in a much greater overall reduction in the nitro group. This can be seen when we compare the limiting value at $t \rightarrow \infty$ for 4NND at a-C of 15 ± 6 %, to a $t \rightarrow \infty$ value for 4NBD at a-C of 42 ± 2 %. Finally, for the photodegradation of nitroaryl groups at amorphous carbon surfaces, we can conclude that rates were increased rapidly at a-C:H compared to a-C surfaces. XPS analysis of the surfaces is required to verify the composition of nitroaryl layers at a-C:H. Changes in the carbon surface such as increased porosity[19] or increased absorptions of the carbon surface due to the lighter colour of hydrogenated films[20-21] could also be possible reasons for the

extremely fast degradation of nitroaryls at the surface. However, further experiments on this surface are required before concrete conclusions can be made.

The results of the photodegradation of nitroaryl molecules at carbon surfaces can be compared to the photodegradation of their corresponding nitroaryl compounds in solution. First order rate constants of degradation were found to be of similar magnitude in solution and at a-C surfaces, with values of 0.219 ± 0.016 h^{-1} and 0.18 ± 0.04 h^{-1} calculated for the degradation of 1NN in aqueous solution and of 4NN at a-C, respectively, following irradiation at λ >200 nm. It has been reported in the literature that, in general, photodegradation tends to be inhibited on surfaces compared to reactions in solution or in the gas phase.[19,22] Interestingly, it can also be concluded from this work that photodegradation is not as effective in solution, due to the larger limiting value at $t \rightarrow \infty$ obtained of 27.9 ± 1.9 % for 1NN in solution versus 15 ± 6 % for 4NN at a-C, following irradiation through filter one with λ > 200 nm. The initial rates of reaction for the photodegradation of nitroaryl molecules in solution were found to be of a similar magnitude to those obtained at a-C surfaces, as demonstrated in Table 4.2. and 4.3. Photodegradation measurements in solution were also carried out using NB which is the monocyclic analogue of 1NN. Results for surface-bound nitroaryl molecules showed that degradation of 4NBD on a-C surfaces had considerable longer lifetime and slower rates than its larger 2-ringed counterpart, 4NND. Similar to these results, the solution analysis of NB revealed its photolysis rates to be significantly slower than 1NN in solution, with a lifetime of more than 24 h estimated versus a lifetime of 4.56 h for 1NN.

Future experiments for the work presented in this chapter include XPS analysis of a-C and a-C:H surfaces after modification, and before and after irradiation. The role of a number of the parameters on the photodegradation of nPAHs will also be examined. An advantage of our photodegradation experimental system is that it has been set up so that pressure, O_2 content, gaseous mixture, temperature and humidity can be controlled.

4.5. References

(1) Finlayson-Pitts, B. J.; Pitts, J. J. N. In *Chemistry of the Upper and Lower Atmosphere*; Academic Press: San Diego, **2000**, 436.

(2) Ancelet, T.; Davy, P. K.; Trompetter, W. J.; Markwitz, A.; Weatherburn, D. C. *Atmospheric Environment* **2011**, *45*, 4463.

(3) Querol, X.; Alastuey, A.; Viana, M.; Moreno, T.; Reche, C.; Minguillón, M.; Ripoll, A.; Pandolfi, M.; Amato, F.; Karanasiou, A. *Atmospheric Chemistry and Physics Discussions* **2013**, *13*, 6971.

(4) Chapman, O. L.; Heckert, D. C.; Reasoner, J. W.; Thackaberry, S. P. *Journal of the American Chemical Society* **1966**, *88*, 5550.

(5) Fan, Z.; Kamens, R. M.; Hu, J.; Zhang, J.; McDow, S. *Environmental Science & Technology* **1996**, *30*, 1358.

(6) Colavita, P. E.; Sun, B.; Tse, K.-Y.; Hamers, R. J. *Journal of the American Chemical Society* **2007**, *129*, 13554.

(7) Sun, B.; Colavita, P. E.; Kim, H.; Lockett, M.; Marcus, M. S.; Smith, L. M.; Hamers, R. J. *Langmuir* **2006**, *22*, 9598.

(8) Cullen, R. J.; Jayasundara, D. R.; Soldi, L.; Cheng, J. J.; Dufaure, G.; Colavita, P. E. *Chemistry of Materials* **2012**, *24*, 1031.

(9) Kameda, T.; Akiyama, A.; Toriba, A.; Tang, N.; Hayakawa, K. *Environmental Science & Technology* **2011**, *45*, 3325.

(10) Kameda, T. *Journal of Health Science* **2011**, *57*, 504.

(11) Bedjanian, Y.; Lelievre, S.; Le Bras, G. *Physical Chemistry Chemical Physics* **2005**, *7*, 334.

(12) Deng, X.; Mammen, L.; Butt, H.-J.; Vollmer, D. *Science* **2012**, *335*, 67.

(13) Murphy, D. M.; Cullen, R. J.; Jayasundara, D. R.; Scanlan, E. M.; Colavita, P. E. *RSC Advances* **2012**, *2*, 6527.

(14) Tolstoy, V. P.; Chernyshova, I. V.; Skryshevsky, V. A. *Handbook of Infrared Spectroscopy of Ultrathin Films*; John Wiley & Sons, Inc.: New Jersey, **2003**.

(15) Ungnade, H. E. *Journal of the American Chemical Society* **1954**, *76*, 1601.

(16) Reichardt, C.; Vogt, R. A.; Crespo-Hernandez, C. E. *The Journal of Chemical Physics* **2009**, *131*, 224518.

(17) Socrates, G. *Infrared and Raman characteristic group frequencies. Tables and Charts*; 3rd ed.; John Wiley & Sons: Chichester, **2001**.

(18) Crespo-Hernandez, C. E.; Vogt, R. A.; Sealey, B. *Modern Chemistry & Applications* **2013**, *1*, 106.

(19) Esteve, W.; Budzinski, H.; Villenave, E. *Atmospheric Environment* **2006**, *40*, 201.

(20) Baek, S. O.; Field, R. A.; Goldstone, M. E.; Kirk, P. W.; Lester, J. N.; Perry, R. *Water Air Soil Pollution* **1991**, *60*, 279.

(21) Vione, D.; Barra, S.; de Gennaro, G.; de Rienzo, M.; Gilardoni, S.; Perrone, M. G.; Pozzoli, L. *Annali di Chimica* **2004**, *94*, 257.

(22) Vione, D.; Maurino, V.; Minero, C.; Pelizzetti, E.; Harrison, M. A.; Olariu, R.-I.; Arsene, C. *Chemical Society Reviews* **2006**, *35*, 441.

5. Carbohydrate coated surfaces using aryldiazonium chemistry

A functional interface has been developed using aryldiazonium chemistry. We present a versatile method of surface modification for the functionalization of a range of materials with bioactive carbohydrates. Immobilization of these important biomolecules onto solid surfaces finds numerous applications in areas such as bio and marine-fouling and surface biomimicry.

Scanlan, E. M.; Colavita, P. E.; Murphy, D. M.; Bourke, J.
"Carbohydrate Functionalized Surfaces".
Patent Application No. PCT/EP2012/069762; Filed on 05/10/2011.

Jayasundara, D.R.; Duff, T. M.; Angione, D.; Bourke, J.; Murphy, D.M.;
Scanlan, E. M.; Colavita, P. E.;
Carbohydrate coatings via aryldiazonium chemistry for surface biomimicry
Chem. Mater., **2013**, *25*, 4122-4128.

5.1. Introduction

Throughout the work presented in this thesis, diazonium chemistry has been exploited as a methodology for the modification of surfaces with desired molecules. The chemistry, properties and some applications of aryldiazonium salts has been discussed in previous chapters. Briefly, it has been established that aryldiazonium salts are versatile reagents that can be used to modify the surface chemistry of a wide variety of substrates. These molecules have been identified as coupling agents, and have been shown to form strong linkages between materials such as nanoparticles, polymers and macromolecules onto surfaces. The use of diazonium chemistry for surface modification has resulted in the discovery of a large number of high performance materials. In this work, we aimed to use the diazonium chemistry expertise gained previously to design, develop and characterize a functional surface.

In previous chapters, diazonium chemistry methodologies were utilized to modify carbon surfaces with nPAHs to create model surfaces for understanding environmental reactions. The interfacial chemistry of aryldiazonium salts spontaneously grafting at carbon surfaces was probed. In this chapter, we aimed to use the information and knowledge gained to immobilize biomolecules at surfaces.

Herein we show how diazonium chemistry can be utilized to functionalize surfaces with carbohydrates. Carbohydrates are enormously important biomolecules that are involved in a wide variety of biological functions such as fertilization, inflammatory responses and cell-cell communication.[1-3] Modifying surfaces with these biomolecules can lead to many exciting applications. Carbohydrate coated surfaces offer materials which mimic the glycosylation patterns of cells surfaces for applications in medical devices, diagnostics and sensors.[4-8] Other uses for coated surfaces could include carbohydrate microarrays and possible applications in antifouling technology.[9-16]

Due to the many potential and proven applications of bioactive surfaces there has been significant interest in developing new methodologies for functionalization of surfaces with biological components.[13-14,17] Previously, the most commonly used methods for the

preparation of sugar coated surfaces included prefunctionalization, ligation and patterning techniques.[18] The direct immobilization of carbohydrates on metal surfaces has been probed using thiol chemistry,[19] amide bond formation and copper catalyzed [3+2] cycloaddition reactions.[13-14,17] However, these methods have encountered problems due to labile bond formation and prefunctionalization requirements, respectively. Also, the multistep nature of these methods means they tend to be time consuming. Diazonium chemistry offers an efficient, one-step procedure for the direct glycosylation of surfaces as an alternative to traditional carbohydrate immobilization methodologies.

Diazonium chemistry has been widely employed for the functionalization of carbon with various aromatic groups but has not previously been employed for glycosylation reactions.[20-21] Surface modification using this aryldiazonium methodology is advantageous in that it forms strong stable covalent bonds with carbon surfaces and can also be used to directly functionalize metals such as copper, gold and alloys.[22-26] Moreover, the grafting methodology can be carried out in aqueous conditions which are ideal for solubilizing the hydrophilic sugar groups. The mild conditions of diazotization are of paramount importance as it is imperative that the adlayers formed during the reaction retain the biological recognition specificity of the original carbohydrate molecules. The mild conditions of the diazotization have been shown in the literature via the functionalization of proteins specifically at tyrosine which proceeded without any denaturing of the protein structure.[27]

Herein we describe the results of our studies into the development of grafting of carbohydrates onto a range of materials including metals and alloys using aryldiazonium chemistry. This one-pot, solution based modification method for functionalizing carbohydrates onto surfaces offers exciting potential for the preparation of a range of glycosylated materials with many possible applications in glycobiology. This work shows the development of a tailor-made bioactive interface with potential commercial application in areas such as antifouling and surface biomimicry.

5.2. Experimental

5.2.1. Chemicals and materials

Acetonitrile (ACN, HPLC grade), fluoroboric acid (HBF_4), hydrogen peroxide (H_2O_2, 30%), methanol (MeOH, semiconductor grade), nitric acid (HNO_3), sodium nitrite ($NaNO_2$), tetrahydrofuran (THF) and concentrated sulphuric acid (H_2SO_4) were obtained from Sigma and used without further purification. Deionized water was used for all aqueous solutions. All glassware and quartz crystals were cleaned with piranha solution before use (3:1, H_2SO_4 to H_2O_2). Compounds (**A**) 4-aminophenyl rhamnoside and (**B**) and benzyl protected 4-aminophenyl rhamnoside were synthesized by Jean Bourke. The procedure for the synthesis of compounds (**1**) – (**4**) is available in the literature and was carried out by my colleague, Dr. Thomas Duff.[28]

5.2.2. Surface preparation

Amorphous carbon (a-C) substrates were prepared by magnetron sputtering of Ti followed by a-C as described in previous chapters and in the literature.[29-30] Following deposition, samples were stored under Ar and used as deposited in functionalization reactions. Substrates were cleaned prior to functionalization in a number of ways; copper foil (pipe grade) was immersed in 0.1 M HNO_3, rinsed with copious DI H_2O and dried in Ar. Copper substrates were used immediately after cleaning. Gold substrates were prepared via electroplating of stainless steel foil using commercially available gold plating solution (Spa Plating Ltd.), following plating, substrates were rinsed in DI H_2O and dried under Ar.

5.2.3. Preliminary grafting experiments

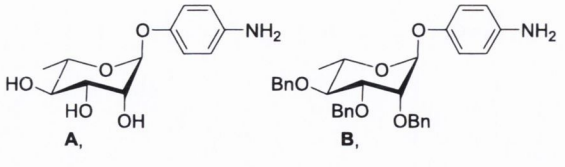

*Scheme 5.1. Structures of unprotected 4-aminophenyl rhamnoside (**A**) and benzyl protected 4-aminophenyl rhamnoside (**B**).*

Preliminary grafting experiments were carried out via *in situ* diazotization of two compounds; unprotected 4-aminophenyl rhamnoside (**A**) and benzyl protected 4-aminophenyl rhamnoside (**B**) and immediate functionalization onto surfaces. The structures of these compounds are shown in Scheme 5.1. The diazotization was carried our following the method illustrated in Scheme 5.3. and described by D'Amours.[31] Briefly, (**A**) and (**B**) were dissolved in an equivalent molarity solution of HBF_4 and kept cool by placing in ice. An aqueous solution of solution of sodium nitrite was added dropwise over 10 min to the rhamnoside solutions yielding the diazonium derivatives of the starting materials in solution. Precursor (**B**) required the use of THF (approximately 1:5 v/v) to enable dissolution into aqueous solution. Substrates were immersed in these solutions for 60 min. Following functionalization, substrates were cleaned via rinsing with DI H_2O and immersion in MeOH for 2 min.

5.2.4. Synthesis of Diazonium tetrafluoroborate derivatives of acetylated carbohydrates and surface functionalization procedure

Various diazonium tetrafluoroborate salts were prepared on treatment of the corresponding 4-aminophenyl glycoside with a solution of sodium nitrite and fluoroboric acid as illustrated in Scheme 5.3. The relevant 4-aminophenyl glycoside (compounds **1-4**, Scheme 5.2.) were dissolved in 20.0 mL of 1.25 mM HBF_4 and kept cool by placing in a beaker of ice. An aqueous solution of $NaNO_2$ (5.0 mL, 5.0 mM) that was also kept in ice was then added dropwise over a period of 10 min to the 4-aminophenyl glycoside solution yielding the diazonium salt with a final concentration of 1.0 mM.

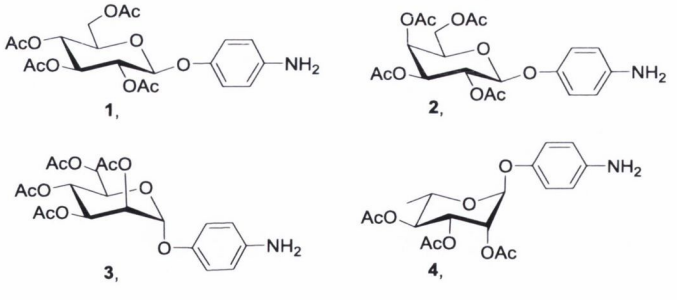

*Scheme 5.2. Peracetylated 4-aminophenyl glucoside (**1**), galactoside (**2**), mannoside (**3**) and rhamnoside (**4**).*

Surfaces were functionalized via immersion in the prepared solutions of diazonium precursors (1.0 mM) for 60 min. Functionalization of carbon substrates with precursor **4** required the use of a small amount of ACN in the aqueous solution (approximately 1:10 v/v) due to the limited solubility of peracetylated rhamnose in water.

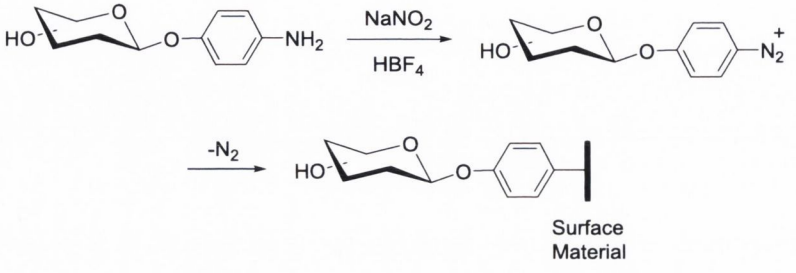

Scheme 5.3. Formation of glycosyl diazonium intermediate.

5.2.5. Characterization Methods

Infrared Reflectance Absorption spectroscopy (IRRAS) was carried out on Ti/a-C samples and on Au and Cu samples using a Fourier Transform Infrared (FTIR) Spectrometer (Tensor 27, Bruker) equipped with a Mercury Cadmium Telluride (MCT) detector, a specular reflectance accessory (VeeMax II) and a ZnSe polarizer. Spectra were taken at 80° incidence using p-polarized light; 256 spectra were collected at 4 cm^{-1} resolution using a bare substrate as a background sample.

Quartz crystals with 10 MHz resonant frequency were used for the Quartz Crystal Microbalance (QCM) measurements described in this study; crystal were coated with 100 nm thick vapour deposited gold electrodes (International Crystal Manufacturing). Carbon coated crystals were obtained via DC-magnetron sputtering of Au electrodes with 10 nm thick Ti adhesive layer followed by a 50 nm a-C film, as previously described.[30] The QCM setup consists of a static Teflon reaction cell, a lever oscillator and a frequency counter connected to a computer for data recording.[26] The crystal was clamped in the static cell with O-rings on both sides resulting in only one face, with a geometric area of 0.205 cm^2, being immersed in the liquid. The frequency of a dry a-C coated crystal, stable over a period of 60 min at 20 °C before insertion into the teflon cell, was taken as the reference frequency. Surface functionalization and rinsing of QCM crystals was carried out following the same procedure as that of substrates for spectroscopic analysis.

5.3. Results and Discussion

5.3.1. Preliminary surface modification using aryldiazonium carbohydrates

Initial grafting experiments were carried out via *in situ* diazotization of compounds (**A**) (unprotected 4-aminophenyl rhamnoside) and (**B**) (benzyl protected 4-aminophenyl rhamnoside) and immediate functionalization onto surfaces. For compound (**A**), modification was carried out on copper and carbon surfaces, whereas for compound (**B**), carbon, copper and gold surfaces were functionalized.

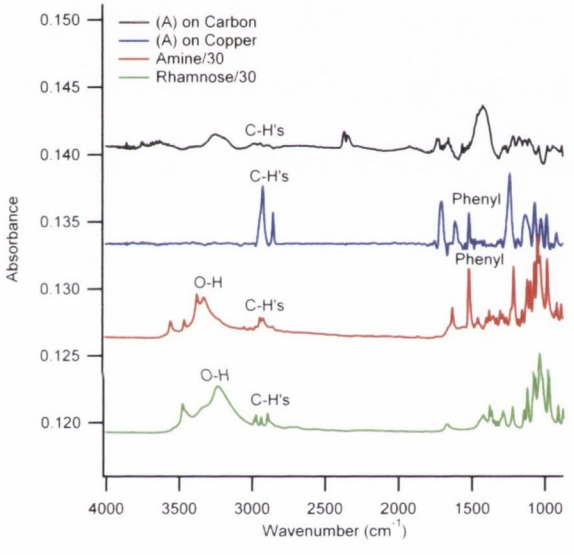

Figure 5.1. Background corrected IRRAS spectra of C and Cu surfaces following in situ modification with (A). IR spectra of parent amine compound and carbohydrate rhamnose.

Figure 5.1. shows the background corrected IRRAS spectra of Cu and C substrates following functionalization with (**A**). IR spectra of the parent amine compound and of the parent carbohydrate rhamnose are also given for comparison. The peaks observed in the IRRAS spectra have been assigned tentatively using the parent compounds spectra and known IR stretching frequencies as can be observed in Figure 5.1.[32] Following functionalization the surfaces were rinsed with DI H_2O and immersed in MeOH, ensuring any physisorbed molecules at the surface were removed. It can be deduced from these results that functionalization at C and Cu surfaces of aryldiazonium carbohydrates following *in situ* diazonium salt generation has occurred. Control experiments were

conducted by immersing substrates in aqueous solutions of $NaNO_2$ or in aqueous solutions of the parent amine alone, without carrying out diazotization reactions which resulted in no peaks in the IRRAS spectra, indicating diazotization in solution is required to achieve functionalization at the surface.

Figure 5.2. shows the 3200 to 2600 cm^{-1} wavenumber region of the IRRAS spectra of C, Cu and Au surfaces following functionalization with (**B**). This region corresponds to the C – H stretching region.[32] Peaks observed on the surfaces indicated that functionalization has occurred. This work indicated that by using aryldiazonium chemistry, surface modification of a number of substrates with protected and unprotected glycosides was possible. To the best of our knowledge, these two examples represent the first demonstration of spontaneous surface modification with diazonium salt derivatives of carbohydrates.

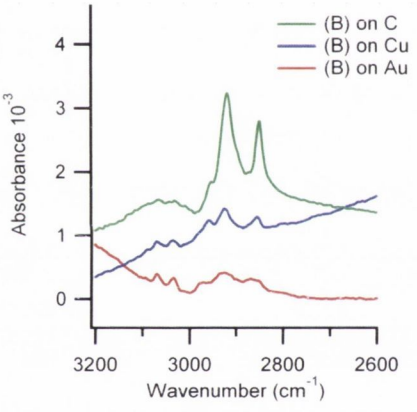

*Figure 5.2. Raw IRRAS spectra of C, Cu and Au surfaces following in situ modification with (**B**).*

5.3.2. Functionalization of various acetylated carbohydrates onto amorphous carbon surfaces

Diazonium grafting has emerged as a highly efficient and general strategy for the functionalization of carbon materials, but has not previously been applied to the modification of surfaces with carbohydrates. In this section, diazonium chemistry was utilized to generate reactive diazonium species *in situ* on treatment of the 4-aminophenyl glycosides given in Scheme 5.2. with a solution of sodium nitrite and fluoroboric acid as shown in Scheme 5.3. The reactive diazonium species reductively adds to carbon surfaces through a robust, covalent carbon-carbon bond as shown in previous work.[21,25,30,33-34] The

data represented in this section followed the experimental procedures outlined in Section 5.2.4. IRRAS was used in order to confirm that surface functionalization took place after immersion of the substrates in aqueous solutions of the *in situ* generated aryldiazonium salts. For the functionalization of carbon surfaces using the diazonium derivatives of 4-aminophenyl glycosides given in Scheme 5.2., I carried out the experiment using precursor (**4**). This compound proved to be somewhat troublesome due to the limited solubility of peracetylated rhamnose in water, therefore a small amount of ACN (CH_3CN) was utilized in the aqueous solution (approximately 1:10 v/v). Figure 5.3. shows the IRRAS spectrum of peracetylated rhamnose following its functionalization onto an amorphous carbon substrate.

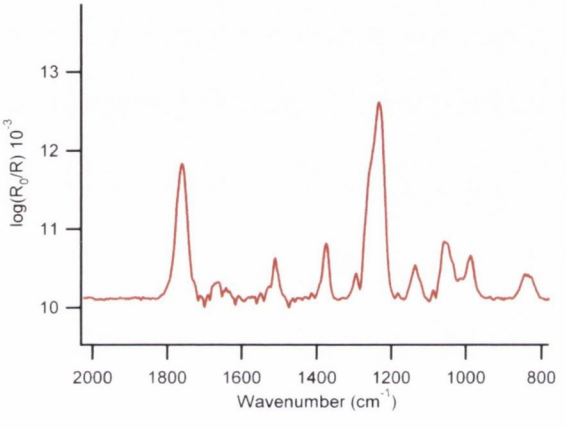

*Figure 5.3. IRRAS spectrum of carbohydrate coated a-C substrate obtained via surface functionalization of aryldiazonium salt **4** from a 1.0 mM aqueous solution.*

The functionalization of amorphous carbon substrates using precursors **1**, **2** and **3** were carried out by my colleagues and are presented in Figure 5.4., along with the trace from precursor **4**. This figure shows IRRAS spectra obtained after surface modification of amorphous carbon coatings using the aryldiazonium derivative of precursor compounds **1, 2**, **3** and **4**, which bear Glc, Gal, Man and Rha monosaccharides, respectively.

Absorbance peaks at 1757 cm^{-1} and 1371 cm^{-1} can be attributed to carbonyl and methyl groups of the acetyl moiety, respectively. Strong absorbances at ~1230 cm^{-1} and in the region 1025-1090 cm^{-1} are associated to C—O stretching modes arising from the carbohydrate ring and the acetyl protecting groups.[32] Peaks in the region 1500-1550 cm^{-1} arise from C—C skeletal vibrations of phenyl rings;[32] in particular, it was possible to

observe in all spectra the presence of a peak at 1508 cm^{-1} which can be attributed to the strong stretching mode of phenyl rings.[35] The IRRAS spectra show the characteristic infrared absorbances of the parent peracetylated glycosides which were also observed in the reference infrared spectra of bulk powders.

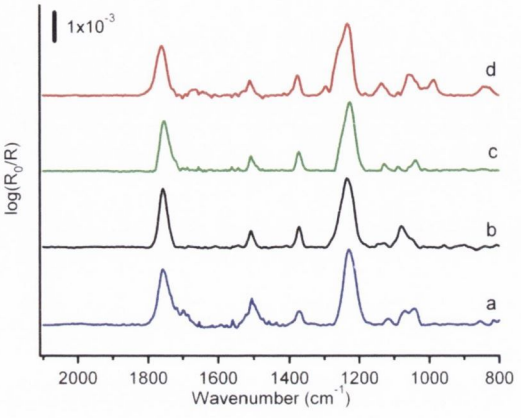

Figure 5.4. IRRAS spectra of carbohydrate coated carbon substrates obtained via surface functionalization of aryldiazonium salts of compounds ***1*** *(trace a),* ***2*** *(trace b),* ***3*** *(trace c) and* ***4*** *(trace d) from 1.0 mM aqueous solutions.*

Control experiments carried out by immersing the substrates in aqueous solutions of 4-aminophenyl glycosides alone, without carrying out diazotization reactions, yielded no IRRAS signatures, thus indicating that formation of aryldiazonium cations is necessary in order to observe the formation of monosaccharide adlayers. These results indicate that peracetylated carbohydrate coatings were obtained in a single step procedure from aqueous solutions via diazotization of acetal-protected precursors followed by chemisorption to carbon substrates. Importantly, this functionalization methodology was found to be general to all of the monosaccharide-derivatives tested.

5.3.3. Functionalization of carbohydrates onto various surfaces

The carbohydrate functionalization methodology was found to be also general with respect to the type of substrate material used. Similar to the results presented in Section 5.3.1., the surface modification was shown to occur successfully at Cu, C and Au surfaces, and functionalization was also expanded to include brass surfaces. The details and results of these experiments are reported in full in the literature.[28]

5.3.4. Surface density of carbohydrate coated carbon films

Quantitative information on the molecular surface density of carbohydrate films obtained at solid surfaces from our one-step methodology was obtained via *ex situ* QCM measurements. Surface density was determined by calculating the mass change at the quartz crystal from the change in resonance frequency using the Sauerbrey equation: (Equation 5.1.)[36]

$$\Delta f = -\frac{2f_0^2}{A\sqrt{\mu\rho}}\Delta m \qquad \text{(Eqn. 5.1.)}$$

where, f_0 is the resonance frequency of the fundamental mode of the QCM in air, A is the effective surface area of the electrodes, and ρ and μ are the density and shear modulus of quartz. The resonant frequency of a-C coated crystals prior to surface modification was considered as the baseline in determining frequency shifts and thereby the mass shifts for all of our experiments. Normalization of mass shifts by the molecular weight of the chemisorbed compound after dediazoniation yielded surface molar densities. For the quantitative assessment of molecular surface density of carbohydrate films, I carried out measurements for precursor (**4**), while the other measurements were carried out by my colleagues.

*Table 5.1. Surface coverage obtained from functionalization reactions with 1.0 mM solutions of 4-aminophenyl glycoside precursors **1-4**.*

	Carbon
	Peracetylated glycoside precursor ($\times 10^{-10}$ mol/cm^2)
Glc	8.1 ± 0.5
Gal	8.0 ± 0.6
Man	7.5 ± 0.4
Rha	7.6 ± 0.3

The surface density of peracetylated monosaccharides obtained via spontaneous aryldiazonium adsorption at carbon substrates from 1.0 mM 4-aminophenyl glycoside solutions was found to be (8.1 ± 0.5) × 10^{-10} mol cm^{-2} for compound **1** (Glc), (8.0 ± 0.6) × 10^{-10} mol cm^{-2} for compound **2** (Gal), (7.5 ± 0.4) × 10^{-10} mol cm^{-2} for compound **3** (Man) and (7.6 ± 0.3) × 10^{-10} mol cm^{-2} for compound **4** (Rha) as shown in Table 5.1. These values

are lower than those reported for the spontaneous attachment of small aryldiazonium salts at the same carbon substrate (e.g. 4-nitrobenzene diazonium salt),[30] as expected based on the much larger geometrical cross-section of compounds **1**, **2**, **3** and **4**.

5.4. Conclusions and supporting work

As discussed earlier, glycosylated surfaces have numerous applications such as in glycoarrays,[5] sensing,[6] and recently in new approaches of inducing specific immune responses.[37-38] These applications rely on biomolecule-carbohydrate recognition processes that must take place at the solid/liquid interface. In order to investigate whether the carbohydrate coatings produced display biomolecule-substrate interactions typical of carbohydrates, surface binding experiments utilizing lectins were carried out.[28] Binding experiments were carried out by Dr. Daniela Angione but the main results are presented here in order to confirm that the functional layers synthesized via aryldiazonium chemistry preserve their biological function once immobilized at the surface.

Briefly, a carbon coated surface was partially coated with α-mannose using deprotected **3** as a precursor. The sample was incubated in a solution of Concanavalan A fluorescein-conjugate (FITC-ConA), which is a lectin whose specific interaction with mannose has been widely investigated.[5] Fluorescence microscopy revealed that the mannose-functionalized area displayed stronger FITC emission than the non-functionalized area indicating an affinity of ConA towards surface-bound mannose groups. A similar result was obtained using galactose-modified surfaces using deprotected **2**, and Peanut Aggulutinin fluorescein-conjugate (FITC-PNA), a lectin that displays binding specificity towards Gal units.[5] Also in this case, FITC-PNA was found to preferentially bind to the Gal-modified areas. Fluorescence microscopy images are given in Figure 5.5. These results showed that the surface-bound carbohydrates displayed typical lectin-carbohydrate interactions. This result suggests that the monosaccharide layers formed via the spontaneous chemisorption of aryldiazonium monosaccharide precursors retain the biological recognition specificity of the parent carbohydrate molecule.

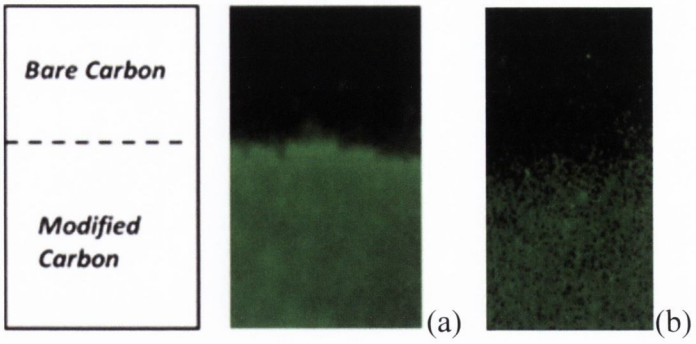

Figure 5.5. Fluorescence microscopy images of carbon surfaces after binding experiments using fluorescently labelled biomolecules; the lower half of the carbon surface has been modified with a monosaccharide, whereas the upper half remains bare. (a) Binding experiment on Man-modified carbon surfaces using FITC-ConA lectin (b) Binding experiment on Gal-modified carbon surface using FITC-PNA.

In conclusion, it has been shown that aryldiazonium chemistry offers a viable approach for the modification of surfaces with carbohydrates. This work offers a one-step, solution based functionalization method for the spontaneous attachment of monosaccharides at carbon, metals and alloys, under mild conditions. Surface coverages of attached carbohydrates can be determined quantitatively and are found to be comparable to typical surfaces densities at aryldiazonium adlayers.[30] This work presented the development of a functional surface fashioned using aryldiazonium chemistry. It is apparent that this functionalization methodology is mild and efficient and should find general applications towards a wide range of materials for biomimetic surfaces and antifouling coatings.

5.5. References

(1) Davis, B. G.; Scanlan, E. M.; Gamblin, D. P. *Chemical reviews* **2009**, *109*, 131.

(2) Dwek, R. A. *Chemical reviews* **1996**, *96*, 683.

(3) Varki, A.; Kornfeld, S. *Essentials of Glycobiology*; 2nd ed.; Cold Spring Harbour Laboratory Press: New York, **2009**.

(4) Ladmiral, V.; Melia, E.; Haddleton, D. M. *European Polymer Journal* **2004**, *40*, 431.

(5) Maupin, K. A.; Liden, D.; Haab, B. B. *Glycobiology* **2012**, *22*, 160.

(6) Craig, D.; Simpson, J.; Faulds, K.; Graham, D. *Chemical Communications* **2013**, *49*, 30.

(7) El-Boubbou, K.; Zhu, D. C.; Vasileiou, C.; Borhan, B.; Prosperi, D.; Li, W.; Huang, X. *Journal of the American Chemical Society* **2010**, *132*, 4490.

(8) Moros, M.; Hernáez, B.; Garet, E.; Dias, J. T.; Sáez, B.; Grazú, V.; González-Fernández, Á.; Alonso, C.; de la Fuente, J. M. *ACS Nano* **2012**, *6*, 1565.

(9) Ban, L.; Pettit, N.; Li, L.; Stuparu, A. D.; Cai, L.; Chen, W.; Guan, W.; Han, W.; Wang, P. G.; Mrksich, M. *Nature Chemical Biology* **2012**, *8*, 769.

(10) dePaz, J. L.; Seeberger, P. H. *Journal of Molecular Biology* **2012**, *808*, 1.

(11) Godula, K.; Bertozzi, C. R. *Journal of the American Chemical Society* **2012**, *134*, 15732.

(12) Rillahan, C. D.; Paulson, J. C. *Annual review of biochemistry* **2011**, *80*, 797.

(13) Horlacher, T.; Seeberger, P. H. *Chemical Society Reviews* **2008**, *37*, 1414.

(14) Park, S.; Gildersleeve, J. C.; Blixt, O.; Shin, I. *Chemical Society Reviews* **2013,** *42*, 4310.

(15) Ederth, T.; Ekblad, T.; Pettitt, M. E.; Conlan, S. L.; Du, C.-X.; Callow, M. E.; Callow, J. A.; Mutton, R.; Clare, A. S.; D'Souza, F.; Donnelly, G.; Bruin, A.; Willemsen, P. R.; Su, X. J.; Wang, S.; Zhao, Q.; Hederos, M.; Konradsson, P.; Liedberg, B. *ACS Applied Materials & Interfaces* **2011**, *3*, 3890.

(16) Otten, L.; Richards, S.-J.; Fullam, E.; Besra, G. S.; Gibson, M. I. *Journal of Materials Chemistry B* **2013**, *1*, 2665.

(17) Feizi, T.; Fazio, F.; Chai, W.; Wong, C.-H. *Current Opinion in Structural Biology* **2003**, *13*, 637.

(18) Pashkuleva, I.; Reis, R. L. *Journal of Materials Chemistry* **2010**, *20*, 8803.

(19) Zhi, Z-L.; Laurent, N.; Powell, A. K.; Karamanska, R.; Fais, M.; Voglmeir, J.; Wright, A.; Blackburn, J. M.; Crocker, P. R.; Russell, D. A.; Flitsch, S.; Field, R. A.; Turnbull, J. E. *ChemBioChem* **2008**, *9*, 1569

(20) Mahouche-Chergui, S.; Gam-Derouich, S.; Mangeney, C.; Chehimi, M. M. *Chemical Society Reviews* **2011**, *40*, 4143.

(21) Barriere, F.; Downard, A. J. *Journal of Solid State Electrochemistry* **2008**, *12*, 1231.

(22) Adenier, A.; Barre, N.; Cabet-Deliry, E.; Chausse, A.; Griveau, S.; Mercier, F.; Pinson, J.; Vautrin-Ul, C. *Surface Science* **2006**, *600*, 4801.

(23) Adenier, A.; Cabet-Deliry, E.; Chaussé, A.; Griveau, S.; Mercier, F.; Pinson, J.; Vautrin-Ul, C. *Chemistry of Materials* **2005**, *17*, 491.

(24) Hurley, B. L.; McCreery, R. L. *Journal of The Electrochemical Society* **2004**, *151*, B252.

(25) Laurentius, L.; Stoyanov, S. R.; Gusarov, S.; Kovalenko, A.; Du, R. B.; Lopinski, G. P.; McDermott, M. T. *ACS Nano* **2011**, *5*, 4219.

(26) Jayasundara, D. R.; Cullen, R. J.; Soldi, L.; Colavita, P. E. *Langmuir* **2011**, *27*, 13029.

(27) Gavrilyuk, J.; Ban, H.; Nagano, M.; Hakamata, W.; Barbas, C. F. *Bioconjugate Chemistry* **2012**, *23*, 2321.

(28) Jayasundara, D. R.; Duff, T.; Angione, M. D.; Bourke, J.; Murphy, D. M.; Scanlan, E. M.; Colavita, P. E. *Chemistry of Materials* **2013**.

(29) Cullen, R. J.; Jayasundara, D.; Soldi, L.; Cheng, J.; DuFaure, G.; Colavita, P. E. *Chemistry of Materials* **2012**, *24*, 1031.

(30) Jayasundara, D. R.; Cullen, R. J.; Colavita, P. E. *Chemistry of Materials* **2013**, *25*, 1144.

(31) D'Amour, M.; Belanger, D. *Journal of Physical Chemistry B* **2003**, *107*, 4811.

(32) Socrates, G. *Infrared and Raman characteristic group frequencies. Tables and Charts*; 3rd ed.; John Wiley & Sons: Chichester, **2001**.

(33) Paulus, G. L. C.; Wang, Q. H.; Strano, M. S. *Accounts of Chemical Research* **2012**, *46*, 160.

(34) Murphy, D. M.; Cullen, R. J.; Jayasundara, D. R.; Scanlan, E. M.; Colavita, P. E. *RSC Advances* **2012**, *2*, 6527.

(35) Varsányi, G. *Assignments for vibrational spectra of seven hundred benzene derivatives*; Halsted Press, **1974**.

(36) Sauerbrey, G. *J. Physik* **1959**, *155*, 206.

(37) Fallarini, S.; Paoletti, T.; Battaglini, C. O.; Ronchi, P.; Lay, L.; Bonomi, R.; Jha, S.; Mancin, F.; Scrimin, P.; Lombardi, G. *Nanoscale* **2013**, *5*, 390.

(38) Carrillo-Conde, B.; Song, E.-H.; Chavez-Santoscoy, A.; Phanse, Y.; Ramer-Tait, A. E.; Pohl, N. L. B.; Wannemuehler, M. J.; Bellaire, B. H.; Narasimhan, B. *Molecular Pharmaceutics* **2011**, *8*, 1877.

6. Fluorine-Fluorine interactions for recovery and separation

Functional fluorinated surfaces were designed and prepared to investigate possible applications for recovery and separation techniques. Fluorine-fluorine interactions between polyfluorinated compounds and fluorinated surfaces were investigated and quantified using Infrared Reflection Absorption Spectroscopy (IRRAS). These results are highly significant as we demonstrate a clear opportunity for designing solid phase recovery systems for pollutants, ligands or catalysts based on fluorous chemistry.

Baker, R. J.; Colavita, P. E.; Murphy, D. M.; Platts, J. A.; Wallis, J. D.
Fluorine – Fluorine interactions in the Solid State:
An Experimental and Theoretical Study
J. Phys. Chem. A, **2012**, *116*, 1435-1444.

6.1. Introduction

Non-covalent fluorine-fluorine interactions were investigated for recovery and separation applications. Several non-covalent interactions such as $\pi - \pi$ stacking, hydrogen bonding, lone pair $- \pi$ interactions and cation/anion $- \pi$ stacking are widely used contacts for constructing supramolecular assemblies.[1-6] In contrast, interactions between the halogens have not been used significantly in the building of supramolecular architectures.[7] Non-covalent interactions do not partake in electron sharing and therefore orbital overlap does not occur. Instead non-covalent interactions undergo attractive intermolecular forces via shared electrostatic interactions. As a result, non-covalent interactions are relatively weak when compared to their covalent counterparts, and act over a longer distance (>2 Å), but this can be advantageous and collectively pooled non-covalent interactions can have a large effect on molecular structure leading to numerous applications.[8-9]

Developing an understanding of these weak non-covalent interactions presents an opportunity for molecular design applications. Non-covalent interactions lead to the formation of molecular clusters and are of paramount importance in supramolecular chemistry, however their importance has also been recognized in other areas.[3] For example, many biodisciplines are heavily reliant on non-covalent interactions; non-covalent interactions hold together the two strands of DNA in the double helix and it has been shown that substitutions of C – H for C – F groups affects enzyme – ligand binding affinities massively.[3,10] Many phenomena have dependencies on non-covalent interactions, including the structures of biomacromolecules (DNA), the structures of liquids, physisorption and molecular recognition.[3] Such a broad scope of related areas highlights the significance of understanding non-covalent interaction chemistry.

Fluorine-fluorine interactions are the non-covalent interactions we have investigated herein. The interactions between fluorine atoms are not believed to be strong, due to their low polarizability and weak interatomic dispersion forces.[11] Halogen-halogen interactions (C – X --- X – C) are reported to occur in two types, as shown in Scheme 6.1.[12] The majority of C – F --- F – C interactions are type 1, which are non-stabilizing and formed via close packing.[6] Alkorta *et al*, investigated systems with a range of F – F coupling constants to

quantify the interaction occurring and found that the systems with strong F – F coupling constants had large electron density, which corresponded to closed shell interactions similar to ionic bonds and hydrogen bonding.[13]

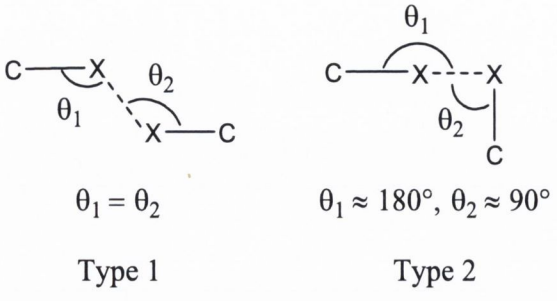

Scheme 6.1. Classification of Halogen – Halogen interactions.

Whilst reviews of these interactions are given in the literature, definitive classification of fluorine-fluorine interactions remains undetermined.[8-9,11,14] Further investigations of closed shell C – F --- F – C interactions are required to gain fundamental understanding of this interaction and to enable them to be further utilized in supramolecular chemistry.

Fluorine-fluorine interactions have become part of what is known as fluorous chemistry, which is the study of structure, properties and reactions of fluorous molecules, fragments, materials and media.[15] Fluorous molecules are defined as molecules which are highly fluorinated or rich in fluorines and based upon sp^3 hybridized carbon. Generally, fluorous molecules comprise of both hydrophobic and lipophobic components, namely an organic and a perfluoroalkyl (ponytail) section. Fluorous interactions can be used for separation, recovery and extraction as highly fluorinated organic compounds will preferentially associate/interact with other fluorinated substances (fluorous separation media) whereas non fluorous molecules will not.[16] The interaction which occurs between fluorous molecules and perfluorinated surfaces enables solid-phase extraction techniques. [16]

Investigations into fluorous interactions began in 1994 when Horvath and Rabai developed a novel method of catalyst separation without water owing to the limited miscibility of partially or fully fluorinated compounds with nonfluorinated compounds.[17] Since this report, fluorous affinity interactions have been well-documented in the literature.[10,16,18]

Several companies are actively marketing fluorous reagents and separation media and this technology forms the basis of commercially available products.[15-16]

Fluorine-fluorine interactions have demonstrated numerous applications including direction of self-assembly,[18-19] immobilization and purification of DNA fragments,[20] use in crystal engineering,[21] and solid phase extraction.[16] Overall, the use of fluorine-fluorine interactions in separation, simplified product isolation, recovery and regeneration of catalysts and reagents has been shown to be very efficient.[20] Publications on non-covalent C – F --- F – C interactions in recent years have been plentiful, stressing the importance of this type of bonding as a useful chemistry tool.[19,22-25]

The work present herein aims to gain further understanding of these interactions in order to fine-tune their usage and make more efficient applications. This work focuses on the use of fluorinated compounds for applications in environmental chemistry and separation science. Extractions of Cs^+ and Sr^{2+} from water into toluene using fluorinated phenols has been shown in the literature by Baker *et al.*,[26] along with examples of fluorinated phosphine oxides and fluorinated ketones as extractants for precious metals, toxic metals and radionuclides.[27-29] This work probes fluorine-fluorine interactions of the various polyfluorinated compounds synthesized, which all feature the same "ponytail" $CF_3(CF_2)_5$-CH_2CH_2. The weak interactions observed between the fluorous chains were utilized to direct the assembly of these perfluorinated compounds onto perfluorinated self-assembled monolayers (PF-SAMs).[30]

The work associated with the results presented in this chapter features the characterization of C – F --- F – C interactions in the solid state via X-ray crystallography and comprehensive computational studies using the AIMS methodology.[30] The following sections show physisorption tests which were carried out to further qualify the interaction. The applicability of the selected compounds to solid phase extraction was investigated via physisorption onto model fluorinated surfaces. The weakly stabilizing nature of these interactions was realized via physisorption of a selected number of compounds containing long chain perfluorinated ponytails onto perfluorinated self-assembled monolayers (PF-SAMs), and characterization with IRRAS (Infrared Reflection Absorption Spectroscopy).

In previous chapters, IRRAS was used to monitor adsorption; however in this chapter the physisorption of polyfluorinated compounds at fluorinated surfaces was probed using this technique. Infrared (IR) spectroscopy can be used for diagnostic interpretation of fluorinated organic compounds with C – F stretches appearing in IR spectra between 1000 and 1360 cm^{-1}. A strong band exists between 1000 and 1100 cm^{-1} for monofluorinated compounds, which splits into two for compounds with more than one fluorine atom. This accounts for the symmetric and asymmetric modes of IR stretch of the C-F bond.

6.2. Experimental

6.2.1. Chemicals and Materials

1H, 1H, 2H, 2H-perfluorodecanethiol (PFT), absolute ethanol (HPLC grade), acetone (HPLC grade) and trioctylphosphine oxide (TOPO) were obtained from sigma and used without further purification. Fluorous compounds $CF_3(CF_2)_5(CH_2)_4(CF_2)_5CF_3$, $(CF_3(CF_2)_5CH_2CH_2)_3P{=}O$, $(CF_3(CF_2)_9CH_2CH_2)_3P{=}O$, $(CF_3(CF_2)_9CH_2CH_2)_3PPhI$, $(CF_3(CF_2)_5(CH_2CH_2)CO_2H$, $(CF_3(CF_2)_5CH_2CH_2)_2P(=O)C_2H_4P(=O)(CH_2CH_2(CF_2)_5CF_3)_2$ were prepared as described in the literature, in the laboratory of Prof. Baker, our collaborator.[27,29-31] The structures of the compounds are detailed in Table 6.1.

6.2.2. Preparation of substrates

Copper (Cu) substrates were cleaned before modification via immersion in *circa* 10% nitric acid solution, rinsing with degassed DI H_2O and drying with Argon flow. Gold substrates were made from stainless steel pieces which were cut to size from a large sheet of commercially available stainless steel (grade 304). Initial treatment consisted of cleaning with acetone, rinsing with degassed DI H_2O and drying under argon flow. Further cleaning involved activation of the stainless steel pieces for 3 min at 6V using activator solution obtained from Spa Plating Ltd. in order to remove the strong oxide layer which can form on stainless steel.

Table 6.1. Compound numbers and structures for fluorine-fluorine physisorption tests.

Compound No.	Structure	Obtained/ Synthesis
1 (Thiol)	$CF_3(CF_2)_7CH_2CH_2SH$	Sigma
2	$CF_3(CF_2)_5(CH_2)_4(CF_2)_5CF_3$	Baker[30]
3	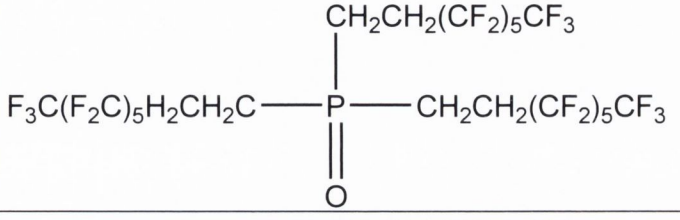	Vlad[31]
4	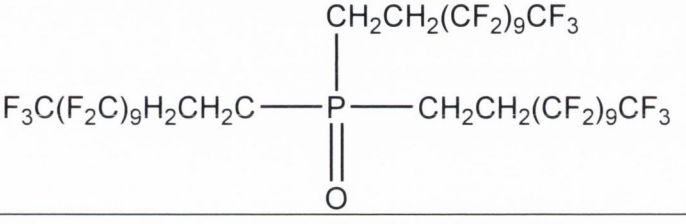	Vlad[31]
5	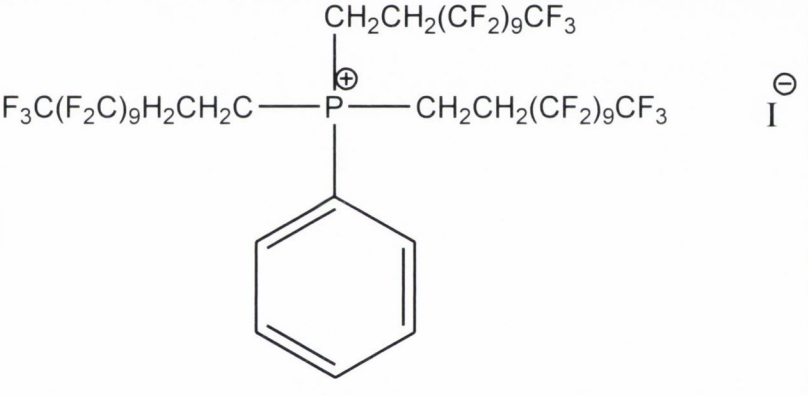	Vlad[31]
6	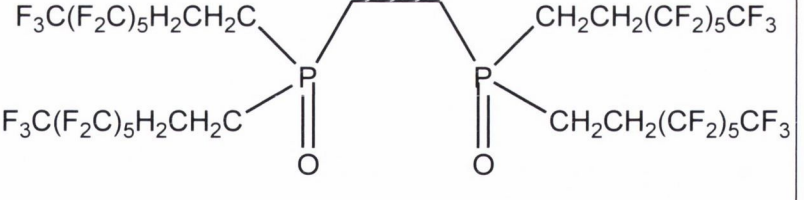	Baker[27]
7	$CF_3(CF_2)_5CH_2CH_2CO_2H$	Baker[29]
8 (TOPO)	$OP(C_8H_{17})_3$	Sigma

Following activation, the samples were rinsed with degassed DI H_2O and dried under argon flow. The stainless steel pieces were then gold plated using gold plating solution (Spa

Plating Ltd.) for 2 min at 4 V. The substrates were rinsed and dried under Argon flow and left overnight under Argon. Stability of the gold plated substrates was checked via strong sonication (12 min) and immersion in strong acid solutions, after which no etching of the surface was observed. Also, no visible defects were seen under a magnifying glass showing substrates were suitable for surface modification.

6.2.3. Preparation of Perfluoro-Self Assembled Monolayers

Perfluoro-self assembled monolayers (PF-SAMs) of 1H,1H,2H,2H-perfluorodecanethiol (PFT) were prepared according to methods which have been previously reported in the literature.[32] Initially, copper substrates were utilized to verify literature reports. Following this, the modification of gold substrates with PF-SAMs was investigated owing to the improved signal obtained on this surface using IRRAS.

6.2.4. Physisorption Studies

Gold substrates were immersed in 1×10^{-3} M solutions of PFT in absolute ethanol for 1 h under argon flow. Following modification, the surface was rinsed three times with absolute ethanol, sonicated for 2 min to remove any physisorbed species and dried under argon. IRRAS measurements were carried out to examine the PF-SAM on the surface. The PF-SAM coated gold substrates were then immersed for 30 min in 1×10^{-3} M solutions of compounds 2-7 in acetone. The substrates were rinsed three times with acetone and dried under argon prior to IRRAS characterization. Following measurements, the substrates were sonicated for 10 min in acetone to remove physisorbed species and IRRAS measurements repeated. A summary schematic of the procedure is given in Figure 6.2. Control experiments were carried out using TOPO instead of the fluorous compounds and also using a gold substrate with no PF-SAM monolayer. IRRAS measurements were carried out on a Bruker Tensor 27 FTIR equipped with an MCT (Mercury Cadmium Telluride) detector using a VeeMax II specular reflectance accessory with a wire grid polarizer. All IRRAS measurements were obtained using p-polarized light at an 80^{o} angle of incidence from the surface normal at a resolution of 4 cm^{-1}; peak integration was carried out using WinFIRST software.

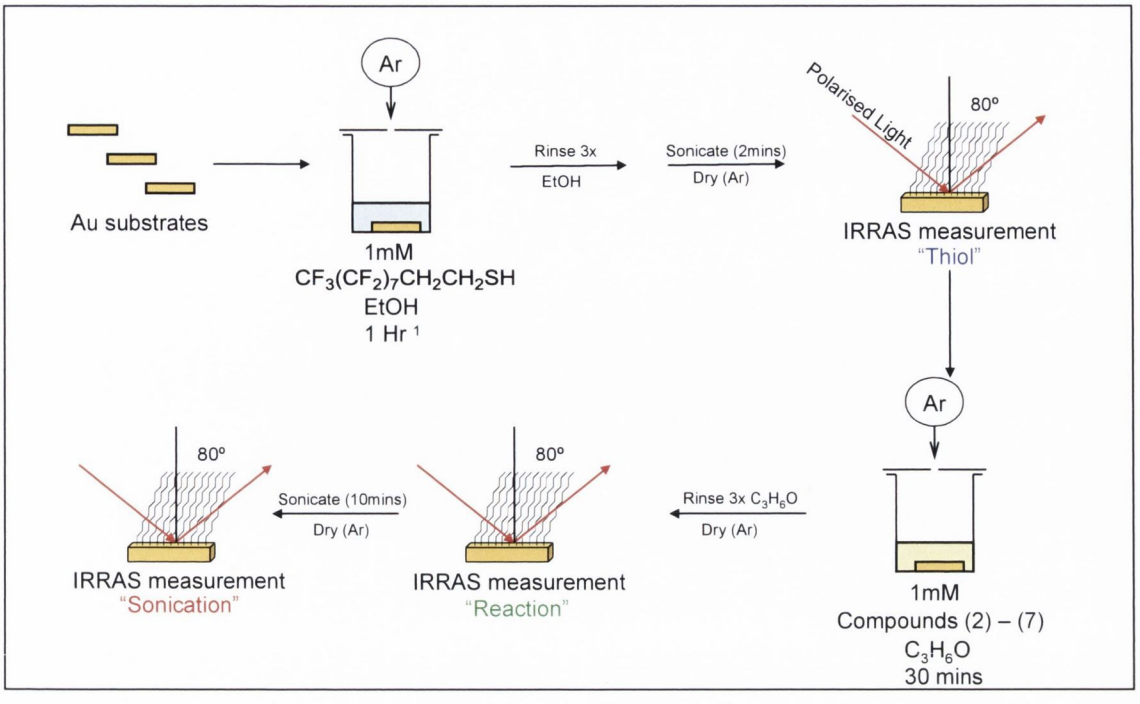

Scheme 6.2. Procedure for the modification of surfaces with fluorinated compounds.

6.3. Results and Discussion

6.3.1. Preliminary grafting experiments

Initially, PF-SAMs were grafted onto Cu substrates to verify literature reports and attain optimal conditions for physisorption tests.[32] In line with the procedure detailed in the literature, 0.1 M PFT was grafted for 2 h at Cu surfaces to achieve PF-SAMs. This modification resulted in the spectrum shown in Figure 6.1. In line with literature reports, peaks attributed to CF_2 asymmetric and symmetric vibrations of the fluorinated chains are present at 1240 cm^{-1} and 1148 cm^{-1}, respectively.[32-34] Unresolved $-CF_3$ stretching modes are present from ~1330 cm^{-1} to 1370 cm^{-1}, along with axial CF_2 stretchings.[33] The prominent peak at ~1217 cm^{-1} is attributed to a vibration which involves the stretching of C-C bonds and bending of CCC angles (υ(CC) + α(CCC)).[33]

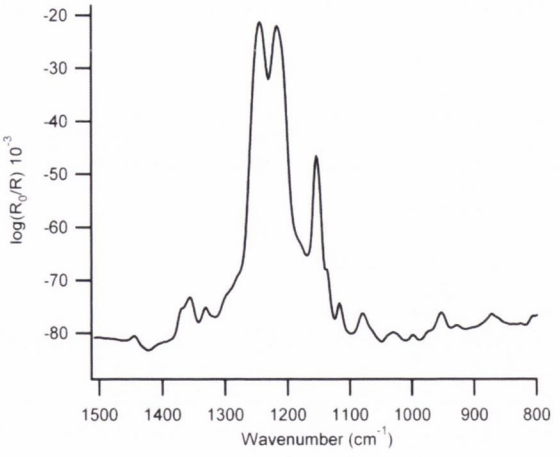

Figure 6.1. IRRAS spectrum of PF-SAM grafted at Cu surface.

Figure 6.1. shows the IRRAS spectrum of 0.1 M PFT grafted at a Cu surface. Whilst the spectrum obtained corresponds well to that reported in the literature, the magnitude of the peaks may incur difficulties in interpreting changes in CF_2 peaks. Therefore, a lower concentration of PF-SAM preparation of 1×10^{-3} M was investigated and found to result in CF_2 stretching heights which would more easily show decipherable changes with physisorbed fluorinated compounds. The stability of the PF-SAM's was investigated and their integrity found to hold for at least 24 h.

6.3.2. Physisorption Studies

Computational analysis and solid state structure determination was carried out on a number of the fluorinated compounds given in Table 6.1. This analysis demonstrated that C – F --- F – C interactions are energetically favorable.[30] In order to investigate the physical applications of these interactions, we explored their uses in solid phase extractions via physisorption studies onto fluorinated surfaces.

For this purpose, the adsorption of compounds 2-7 onto a model fluorinated surface (PF-SAM on gold substrates) was probed using IRRAS. The compounds given in Table 6.1. were chosen so that we could determine the effects that chain length, number of ponytails and charge would have on their physisorption onto the fluorinated surface. For example, comparing compounds 3 and 4 will show the effect of chain length due to the increase in CF_2 moieties, comparing compounds 7, 2, 3 and 6 will show the effect of increasing the

number of ponytails from one through four and finally comparing compounds 4 and 5 will highlight any differences in absorptions due to charge on molecules.

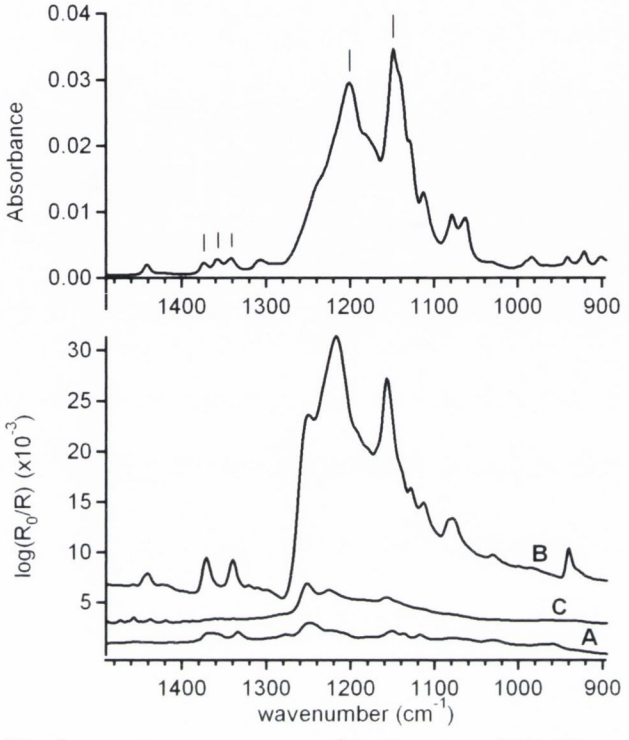

Figure 6.2. ***Top:*** *IR absorption spectrum of 5.* ***Bottom:*** *IRRAS spectra of PF-SAM (A), of PF-SAM after adsorption of compound 5 (B), and after vigorous sonication to remove physisorbed material (C). Spectra have been offset for clarity.*

All of the fluorinated compounds discussed in this work display strong infrared absorption peaks in the region 1000-1400 cm^{-1}, which are assigned to C−F stretching modes of the fluorinated chains.[35] Figure 6.2(top) shows a typical absorption infrared spectrum for this region, obtained following analysis of compound 5. The spectrum displays several unresolved peaks with two prominent absorptions at 1148 and 1200 cm^{-1} that, based on previous assignments,[36-37] are attributed to the symmetric and asymmetric $-CF_2$ stretching modes, respectively, of the fluorinated chains. Three peaks with maxima at 1342, 1357, and 1374 cm^{-1} are attributed to $-CF_3$ stretching modes. Peak intensities observed in IRRAS spectra are the result of both surface coverage and orientation effects; however, in the case of disordered films, the integrated intensity can be used to monitor surface coverage.[38-39] We therefore used the integrated peak area to quantitate the adsorption of fluorinated compounds on the PF-SAMs on gold. Figure 6.2.(bottom) shows a typical set of IRRAS

spectra with absorptions in the 1000-1400 cm^{-1} region for the PF-SAM (trace A), the surface after exposure to acetone solutions of 5 (trace B) and the same surface after 10 min sonication in acetone to remove physisorbed material (trace C).

6.3.3. Comparison of physisorption of compounds

IRRAS spectra of PF-SAMs alone displayed absorptions in the 1000-1400 cm^{-1} with an integrated area of 0.18 ± 0.01 (90% C.I.). Upon adsorption of fluorinated compounds, the integrated intensity in the region 1000-1400 cm^{-1} increased as expected from an increase in the surface density of $-CF_2$ and $-CF_3$ groups. Following sonication, the intensity of the C–F stretching absorbance's returned to the initial values, suggesting that physisorption on fluorinated surfaces is reversible. This behaviour is summarized in Figure 6.3. which gives integrated absorptions measured for compounds 2-7: it was consistently observed that all of the compounds physisorbed on the PF-SAM.

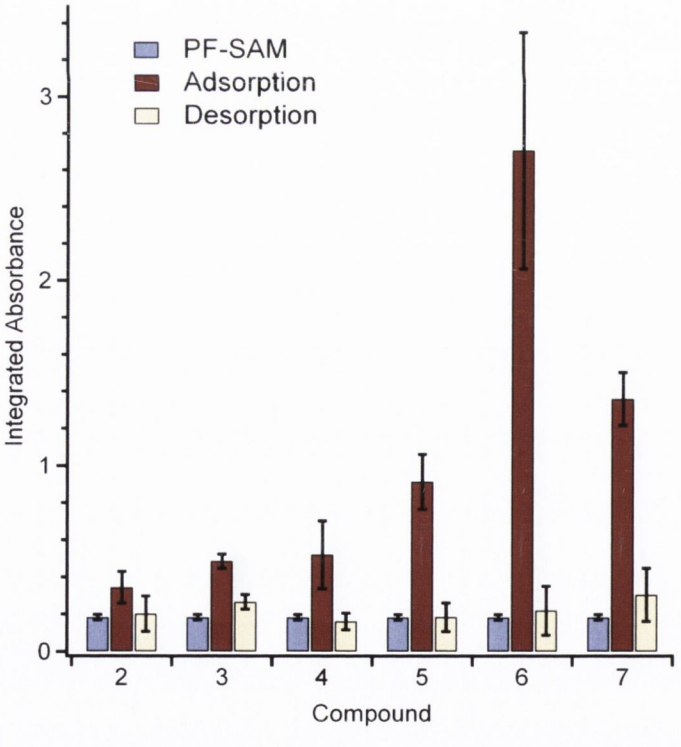

Figure 6.3. Integrated absorbances in the region 1400-1000 cm^{-1} of compounds 2-7. Error bars indicate 90% C.I.

Control experiments on bare gold surfaces did not yield significant absorption peaks in this region, thus indicating that an increase in infrared absorption results from molecular assembly onto the PF-SAM, as opposed to simple precipitation/aggregation from solution.

The largest increase in surface coverage is observed for the bidentate phosphine compound 6, which has four fluorinated $-(CF_2)_5CF_3$ chains. The increase in adsorption is much higher than that expected on the basis of the results for 3, which possesses three of the same fluorinated chains (expected approximately 30% increase). This would suggest that either the arrangement of the fluorinated chains or the presence of P=O groups is responsible for more favorable interactions with the surface. Control experiments carried out using trioctylphosphine oxide ($Oct_3P=O$, TOPO) the nonfluorous analogue of 3, showed no increase in intensity in the C–H (2800-3000 cm^{-1}) stretching region, thus suggesting that P=O groups should not promote adsorption significantly. Therefore, we propose that the arrangement of fluorinated chains is important in determining adsorption properties. It is interesting to note that 6 would probably exist in the transoid form, as seen crystallographically for other examples of bidentate phosphine oxides,[40] which may give a bigger "footprint" compared to 3.

4 and 5 both have the same number of fluorous groups so the increase in 5 compared to 4 may be due to either electrostatics or the phenyl groups allowing for a further stabilization by $\pi-\pi$ interactions to form a bilayer rather than monolayer motif. Compounds 6, 3, 2, and 7 show a steady decrease in $-CF_2$ and $-CF_3$ functionality that is mirrored in the decreased absorbance observed for their reactions on the fluorinated thiol coated surface. Comparing 3 to 4 we can identify the effect chain length has on physisorption, as the increase in adsorption onto the longer chained 4 shows that the longer chain promotes more efficient adsorption. A summary of the integrated absorptions in the 1000-1400 cm^{-1} region obtained for compounds 2-8 is given in Table 6.2. This includes the average integrated absorbances, which was carried out using WinFIRST software, for the PF-SAM, adsorption and desorption layers and also their standard deviations. A summary figure of the IRRAS spectra and a table of possible peak assignments for compounds 2-7 are also given below in Figure 6.4. and Table 6.3. respectively.

Table 6.2. Summary of the integrated absorbances in the 1000-1400 cm^{-1} region for compounds 2-8.

Integrated Absorbances from 1000-1400cm^{-1}							
Compound	**PF-SAM**	**Adsorption**	**Desorption**		**PF-SAM**	**Adsorption**	**Desorption**
2.1	0.149911	0.471153	0.253249				
2.2	0.185843	0.475155	0.255123	Av	0.193092	0.486037	0.267913
2.3	0.243523	0.511804	0.295367	SD	0.047225	0.022404	0.023794
3.1	0.138361	0.609932	0.136370				
3.2	0.123056	0.552657	0.161623	Av	0.145182	0.521240	0.162127
3.3	0.174129	0.401131	0.188388	SD	0.026211	0.107888	0.026013
4.1	0.145444	0.963538	0.136114				
4.2	0.190146	0.966107	0.225551	Av	0.172511	0.914264	0.184665
4.3	0.181944	0.813148	0.192331	SD	0.023797	0.087579	0.045209
5.1	0.158360	1.356024	0.216493				
5.2	0.177663	1.445275	0.386375	Av	0.159711	1.359130	0.304781
5.3	0.143111	1.276087	0.311474	SD	0.017316	0.084637	0.085139
6.1	0.193071	3.146851	0.188428				
6.2	0.213833	2.476758	0.164580	Av	0.217413	2.706700	0.220501
6.3	0.245335	2.496478	0.308496	SD	0.026315	0.381313	0.077133
7.1	0.191341	0.302047	0.205501				
7.2	0.182286	0.400210	0.257992	Av	0.199109	0.344779	0.203465
7.3	0.223699	0.332079	0.146902	SD	0.021772	0.050299	0.055573
8.1	0.228170	0.229869	0.232050				

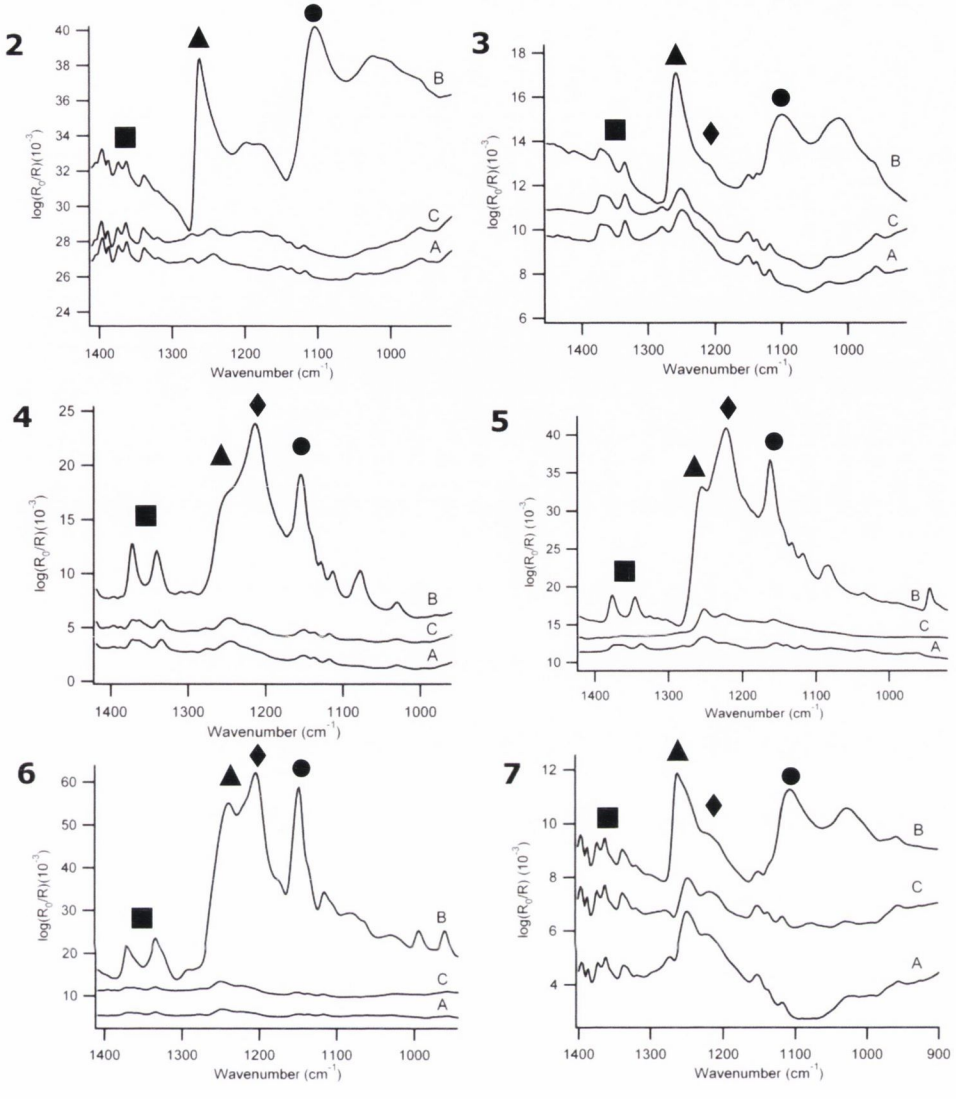

Figure 6.4. IRRAS spectra of PF-SAM (A), of PF-SAM after adsorption of compounds (B), and after vigorous sonication to remove physisorbed material (C) for compounds 2-7. Spectra have been offset for clarity. Unresolved peaks are assigned as follows CF_3 stretching modes (■), asymmetric CF_2 vibrations (▲), symmetric CF_2 vibrations (●) stretching of C-C bonds and bending of CCC (♦).

Table 6.3. Peak assignments for fluorinated compounds 2-7.[35]

Functional Groups	IR (cm^{-1})	Strength	Comments
C–F	1400-1000	strong	C-F stretch, general range
	830-520	strong	C-F deformation, general range
Polyfluorinated alkanes	1360-1090	very strong	a number of bands
CF_3–CF_2–	1365-1325	strong-med	C-F stretch
	745-730	strong	C-F deformation vibration
–CF_3	1390-1105	strong-med	C-F stretch, α-unsaturated CF_3
	1215-1045	strong-med	C-F stretch, α-unsaturated CF_3
	780-610	med-weak	C-F deformation vibration, α-unsaturated CF_3
–CF_2–	1300-1100	strong	asym C-F stretch, (usually found 1275-1175cm^{-1})
	1200-1060	strong	sym C-F stretch

6.4. Conclusions

This work developed a means of quantifying fluorine-fluorine interactions between polyfluorinated compounds and fluorinated surfaces. Fluorine-fluorine interactions were leveraged to physisorb selected fluorinated compounds onto fluorinated surfaces. IRRAS measurements revealed that the physisorption is reversible. Differences between the fluorous molecules show distinguishable differences in their physisorption onto PF-SAMs. We have shown that increases in chain length, number of ponytails and introduction of charged molecules brings about increases in their adsorption onto surfaces.

These results are highly significant as they show it is possible to design solid phase recovery systems for ligands, catalysts or pollutants based on fluorous interactions. Such technology could prove to be extremely useful and of commercial value, both in industry and for environmental applications, for use in organofluoride analysis or remediation. The weakness of fluorous interactions relative to other intermolecular forces is an advantage for such applications, because, as shown in our experiments it allows for the ease of desorption/recovery.

6.5. References

(1) Gilli, G.; Gilli, P. *The Nature of the Hydrogen Bond; Outline of a Comprehensive Hydrogen Bond Theory*; 'Oxford University Press': Oxford, U.K., **2009.**

(2) Schottel, B.; Chifotides, H.; Dunbar, K. *Chemical Society Reviews* **2008**, *37*, 68.

(3) Tewari, A. K.; Dubey, R. *Bioorganic & Medicinal Chemistry* **2008**, *16*, 126.

(4) Mooibroek, T. J.; Black, C. A.; Gamez, P.; Reedijk, J. *Crystal Growth & Design* **2008**, *8*, 1082.

(5) Ma, J. C.; Dougherty, D. A. *Chemical Reviews* **1997**, *97*, 1303.

(6) Barcelo-Oliver, M.; Estarellas, C.; Garcia-Raso, A.; Terron, A.; Frontera, A.; Quinonero, D.; Mata, I.; Molins, E.; Deya, P. M. *CrystEngComm* **2010**, *12*, 3758.

(7) Legon, A. C. *Physical Chemistry Chemical Physics* **2010**, *12*, 7736.

(8) Berger, R.; Resnati, G.; Metrangolo, P.; Weber, E.; Hulliger, J. *Chemical Society Reviews* **2011**, *40*, 3496.

(9) Chopra, D.; Row, T. N. G. *CrystEngComm* **2011**, *13*, 2175.

(10) Purser, S.; Moore, P. R.; Swallow, S.; Gouverneur, V. *Chemical Society Reviews* **2008**, *37*, 320.

(11) Reichenbächer, K.; Süss, H. I.; Hulliger, J. *Chemical Society Reviews* **2005**, *34*, 22.

(12) Ramasubbu, N.; Parthasarathy, R.; Murray-Rust, P. *Journal of the American Chemical Society* **1986**, *108*, 4308.

(13) Alkorta, I.; Elguero, J. *Structural Chemistry* **2004**, *15*, 117.

(14) O'Hagan, D. *Chemical Society reviews* **2008**, *37*, 308.

(15) Gladysz, J. A.; Curran, D. P. *Tetrahedron* **2002**, *58*, 3823.

(16) Pearson, W. H.; Berry, D. A.; Stoy, P.; Jung, K.-Y.; Sercel, A. D. *The Journal of Organic Chemistry* **2005**, *70*, 7114.

(17) Horváth, I. T.; Rábai, J. *Science* **1994**, *266*, 72.

(18) Halper, S. R.; Cohen, S. M. *Inorganic Chemistry* **2005**, *44*, 4139.

(19) Huston, S. M.; Wang, J.; Loth, M. A.; Anthony, J. E.; Conrad, B. R.; Dougherty, D. B. *The Journal of Physical Chemistry C* **2012**, *116*, 21465.

(20) Beller, C.; Bannwarth, W. *Helvetica Chimica Acta* **2005**, *88*, 171.

(21) Banerjee, S.; Dastidar, P. *CrystEngComm* **2013**.

(22) Dikundwar, A. G.; Row, T. N. G. *Crystal Growth & Design* **2012**, *12*, 1713.

(23) Jarzembska, K. N.; Kubsik, M.; Kamiński, R.; Woźniak, K.; Dominiak, P. M. *Crystal Growth & Design* **2012**, *12*, 2508.

(24) Smrcok, L.; Mach, P.; Le Bail, A. *Acta Crystallographica Section B* **2013**, *69*, 395.

(25) Yamada, S.; Kinoshita, K.; Iwama, S.; Yamazaki, T.; Kubota, T.; Yajima, T. *RSC Advances* **2013**, *3*, 6803.

(26) Baker, R. J.; Ogilvie, H. V.; Richards, A. J. *Radiochimica Acta* **2010**, *98*, 507.

(27) Baker, R. J.; Fuchs, J.; Richards, A. J.; Ogilvie, H. V. *Journal of Environmental Management* **2011**, *92*, 2781.

(28) Baker, J.; Baker, R.; Schulzke, C. *Gold Bulletin* **2011**, *44*, 79.

(29) Baker, R. J.; McCabe, T.; O'Brien, J. E.; Ogilvie, H. V. *Journal of Fluorine Chemistry* **2010**, *131*, 621.

(30) Baker, R. J.; Colavita, P. E.; Murphy, D. M.; Platts, J. A.; Wallis, J. D. *The Journal of Physical Chemistry A* **2011**, *116*, 1435.

(31) Vlád, G.; Richter, F. U.; Horváth, I. T. *Tetrahedron Letters* **2005**, *46*, 8605.

(32) Patois, T.; Et Taouil, A.; Lallemand, F.; Carpentier, L.; Roizard, X.; Hihn, J.-Y.; Bondeau-Patissier, V.; Mekhalif, Z. *Surface and Coatings Technology* **2010**, *205*, 2511.

(33) Laffineur, F.; Auguste, D.; Plumier, F.; Pirlot, C.; Hevesi, L.; Delhalle, J.; Mekhalif, Z. *Langmuir* **2004**, *20*, 3240.

(34) Tsao, M. W.; Hoffmann, C. L.; Rabolt, J. F.; Johnson, H. E.; Castner, D. G.; Erdelen, C.; Ringsdorf, H. *Langmuir* **1997**, *13*, 4317.

(35) Socrates, G.; John Wiley&Sons Ltd.: New York, **2004**, 198.

(36) Ren, Y.; Iimura, K.-i.; Ogawa, A.; Kato, T. *The Journal of Physical Chemistry B* **2001**, *105*, 4305.

(37) Schuy, S.; Faiss, S.; Yoder, N. C.; Kalsani, V.; Kumar, K.; Janshoff, A.; Vogel, R. *The Journal of Physical Chemistry B* **2008**, *112*, 8250.

(38) Desroches, M. J.; Chaudhary, N.; Omanovic, S. *Biomacromolecules* **2007**, *8*, 2836.

(39) Colavita, P. E.; Sun, B.; Tse, K.-Y.; Hamers, R. J. *Journal of the American Chemical Society* **2007**, 129, 13554.

(40) Calcagno, P.; Kariuki, B. M.; Kitchin, S. J.; Robinson, J. M. A.; Philp, D.; Harris, K. D. M. Chemistry – A European Journal **2000,** 6, 2338.

7. Conclusions and Future Work

In this work we aimed to design and characterize functional nPAH/carbon interfaces for fundamental studies of nPAH chemistry. An introduction to the chemistry of these ubiquitous contaminants, an explanation of the broader relevance of the project and a brief description of the methodologies utilized is presented.

Following the introduction, a comprehensive investigation of the spontaneous grafting of nitroaromatic diazonium salts at model carbon surfaces is offered. We focused on the adsorption kinetics of the spontaneous grafting reaction of aryldiazonium salts and probed the reliance of the grafting rate and yield on the structure and stability of the salt using a combination of spectroscopic and electrochemical techniques. We discovered that the adsorption rates of the positional isomers investigated were significantly different at amorphous carbon surfaces, a disparity which we attributed to a shift in reduction potential of the aryldiazonium salts. The results obtained indicated that the spontaneous attachment of diazonium derivatives of nPAHs can lead to different layers at carbon surfaces, depending on the position of the $-N_2^+$ functional group with respect to other substituents in the condensed ring system.

The fundamental processes occuring at the carbon-solution interface during spontaneous attachment were then probed via a detailed examination of the charge transfer properties of the carbon surfaces. We discussed our results in light of our current understanding of aryldiazonium chemisorption reactions and available models of charge-transfer at the solid/liquid interface. Gerischer-Marcus theory was utilized to interpret experimentally determined charge transfer rates and aryldiazonium adsorption data, and resulted in efficacious predictions of rates at graphitic carbon surfaces. Predictions for spontaneous aryldiazonium adsorption were of a much larger magnitude than those experimentally observed, suggesting that electron transfer is not the rate determining step for adsorption at amorphous carbons. Possible rate controlling processes could be hole scavenging at the carbon surface, surface reorientation or diffusion. The work presented gives the first example of a successful correlation between valence electronic structure determination and electrochemical electron transfer rate results at amorphous carbon materials. Importantly,

we can conclude from our results that a modification of the electronic properties of disordered carbons enabled us to control relative reaction rates at the carbon/solution interface. This control can be used to gain mechanistic insight into chemical reactions and also to develop guiding criteria for achieving selectivity in interfacial reactions.

The photochemical behavior of nPAHs at carbon surfaces was studied as a model for the reactions which occur on soot particles in the atmosphere. Spectroscopic and absorption techniques were utilized to examine the degradation of nitroaromatic molecules at surfaces and in solution, respectively. The photodegradation of nPAHs at surfaces was found to occur via the loss of the nitro group and this transformation occurs in parallel with an oxidation process. We propose the oxidation process is as a result of the photodegradation of the nitro species due to observations in infrared spectra, and have assigned the oxidation process to the formation of carbonyls. First order rate constants for the photodegradation of nitroaryls at carbon surfaces were obtained and a dependence on the absorption spectra of the molecule under irradiation was identified. The photodegradation of nPAHs at amorphous carbon surfaces and in solution were investigated and compared, with similar values for first order rate constants of degradation obtained. Photodegradation of the polycyclic naphthalene analogue occurred over a shorter timescale than its monocyclic counterpart, both in solution and when adsorbed at an amorphous carbon surface. XPS analysis of modified surfaces is part of the future work of this project, so that the composition of nitroaryl layers at the differing carbon surfaces can be characterized, and the role that the composition of the layers plays in the photodegradation can be identified.

Following this, bioactive model interfaces were developed utilizing diazonium chemistry. Immobilization was confirmed via infrared characterisation, along with a quantitative assessment of the surface density of carbohydrate coated films obtained at carbon surfaces using *ex situ* quartz crystal microbalance measurements. It was confirmed that the functional layers synthesized via aryldiazonium chemistry preserve their biological function once immobilized at the surface. The methodology utilized should find numerous applications as it is a one-step, solution based functionalization procedure for the spontaneous attachment of monosaccharides at various surfaces, under mild conditions.

Finally, fluorine-fluorine interactions were investigated for extraction and separation technologies. Fluorine-fluorine interactions were leveraged to physisorb selected polyfluorinated compounds onto fluorinated surfaces and the interaction was quantified using infrared techniques. Our results revealed that physisorption was reversible. The interactions identified were rationalized based on the chemical structure of the fluorinated molecules. We demonstrated that increases in chain length, number of ponytails and introduction of charged molecules brought about increases in adsorption of molecules onto surfaces. A control experiment utilizing the corresponding alkanethiol self-assembled monolayer should be carried out as part of the future work for this project. The results presented are highly significant as a clear opportunity for designing solid phase recovery systems for pollutants, ligands or catalysts based on fluorous interactions is demonstrated.